OBSERVATIONS OF
NITROGEN AND OXYGEN ISOTOPES IN THE
LOW ENERGY COSMIC RAYS

Thesis by
Solomon Benjamin Vidor

In Partial Fulfillment of the Requirements
for the Degree of
Doctor of Philosophy

California Institute of Technology
Pasadena, California

1975

(Submitted May 29, 1975)

To Candy,

whose love has been my inspiration.

ACKNOWLEDGEMENTS

Many people have contributed to making this thesis possible. Foremost is my thesis advisor, Professor Edward C. Stone, who continually provided encouragement and sound advice. As principal investigator on these experiments, he has been responsible for the experiments since the proposal stage.

I also wish to express my appreciation to Professor Rochus Vogt, who,as co-investigator on these experiments, has made many valuable contributions to the experiments and to my research in particular.

Gordon Hurford was responsible for preparing the detector stack and for performing calibrations on the IMP-7 instrument. I would also like to thank Gordon for implementing the many data analysis programs that have been indispensable to this work.

The assistance of Dick Mewaldt in planning and performing the calibrations of the IMP-8 instrument is appreciated. Dick has also made many valuable suggestions throughout the course of this research.

Bill Althouse, the project engineer, deserves much of the credit for the successful operation of the experiments.

Conversations with Professor Jon Mathews have contributed to my understanding of the subtleties of the maximum likelihood method.

I would like to acknowledge the aid and advice of Rick Cook, Alan Cummings, Tom Garrard, Steward Hartman, Frank Marshall, and Mark Wiedenbeck and the contributions they have made to this thesis.

The assistance of Steve Early and Max Kaye with the prelaunch calibrations and of Hubert Shen with the data analysis have greatly benefited this work. Ellen Aguilar and Florence Pickett ably performed much of the routine data analysis.

I am indebted to Professor Charles Barnes for permission to calibrate the instrument at the Kellogg Tandem Accelerator. I would also like to thank Professor Barnes and Dr. Hay Boon Mak for their assistance with the calibration.

The excellent job of typing this thesis was performed by Irene Logsdon. The figures and reproduction of the thesis are due to the fine work by the staff of Graphic Arts.

The fabrication and detailed design of the experiment was the responsibility of the Analog Technology Corporation.

I received assistance from a NASA traineeship during part of my study. This research has been supported by NASA under NAS5-11066 and NGR 05-002-160.

ABSTRACT

The isotopic composition of the enhanced low energy nitrogen and oxygen cosmic rays can provide information regarding the source of these particles. Using the Caltech Electron/Isotope Spectrometer aboard the IMP-7 satellite, a measurement of this isotopic composition was made. To determine the isotope response of the instrument, a calibration was performed, and it was determined that the standard range-energy tables were inadequate to calculate the isotope response. From the calibration, corrections to the standard range-energy tables were obtained which can be used to calculate the isotope response of this and similar instruments.

The low energy nitrogen and oxygen cosmic rays were determined to be primarily ^{14}N and ^{16}O. Upper limits were obtained for the abundances of the other stable nitrogen and oxygen isotopes. To the 84% confidence level the isotopic abundances are: $^{15}N/N \leq 0.26$ (5.6 - 12.7 MeV/nucleon), $^{17}O/O \leq 0.13$ (7.0 - 11.3 MeV/nucleon), $^{18}O/O \leq 0.12$ (7.0 - 11.2 MeV/nucleon). The nitrogen composition differs from higher energy measurements which indicate that ^{15}N, which is thought to be secondary, is the dominant isotope. This implies that the low energy enhanced cosmic rays are not part of the same population as the higher energy cosmic rays and that they have not passed through enough material to produce a large fraction of ^{15}N. The isotopic

composition of the low energy enhanced nitrogen and oxygen is consistent with the local acceleration theory of Fisk, Kozlovsky, and Ramaty, in which interstellar material is accelerated to several MeV/nucleon. If, on the other hand, the low energy nitrogen and oxygen result from nucleosynthesis in a galactic source, then the nucleosynthesis processes which produce an enhancement of nitrogen and oxygen and a depletion of carbon are restricted to producing predominantly ^{14}N and ^{16}O.

TABLE OF CONTENTS

		PAGE
I.	INTRODUCTION	1
II.	EXPERIMENT	3
	A. Spacecraft	3
	B. Instrument	3
	C. Isotope Response	20
	D. Calibrations	25
III.	OBSERVATIONS	35
	A. Definition of Quiet Time Data	35
	B. Energy Spectra	40
	C. Element Abundances	55
	D. Isotope Abundances	63
IV.	DISCUSSION OF RESULTS - POSSIBLE SOURCES	78
	A. Introduction	78
	B. Solar Origin	79
	C. Galactic Source	83
	D. Local Source	84
V.	SUMMARY AND CONCLUSIONS	87
APPENDIX A	- Data Analysis	89
APPENDIX B	- Cross-Talk Between Detectors	97

		PAGE
APPENDIX C -	Calibrated Isotope Response	102
	A. Introduction	102
	B. Calibration	106
	C. Results	111
REFERENCES		148

1. INTRODUCTION

Recently, a new component with unusual composition has been reported in the low energy cosmic rays (Hovestadt et al., 1973; McDonald et al., 1974). The 3 - 30 MeV/nucleon nitrogen and oxygen fluxes are enhanced relative to an extrapolation from higher energies, while no similar enhancement is observed in the carbon flux. As a result, at 10 MeV/nucleon oxygen is about 30 times as abundant as carbon, whereas at higher energies (Webber et al., 1972) carbon is slightly more abundant than oxygen. In addition, at 10 MeV/nucleon oxygen is almost as abundant as hydrogen and helium, while at ~ 1 GeV/nucleon (Webber et al., 1972; Webber and Lezniak, 1974). the oxygen/hydrogen and oxygen/helium ratios are typically 0.002 and 0.02.

The unusual elemental composition of these low energy cosmic rays has prompted numerous investigators to study their properties in the hope of determining their origin. McDonald et al. (1974) have found a positive radial gradient for the low energy oxygen, indicating that these particles are not solar in origin. The large time variations which have been observed in the low energy oxygen flux also argue against a solar origin. For example, at 10 MeV/nucleon the 1968 and 1969 oxygen fluxes (Teegarden et al., 1969; Mogro-Campero et al., 1973) are a factor of 10 - 50 below the 1972 flux. The more recent 1972 - 1973 measurements also show time variations. These variations do not correlate with the variations of the low intensity 1.3 - 2.3 MeV

protons, which are likely of solar origin, but they are correlated with the variations of higher energy galactic cosmic rays (Mewaldt et al., 1974a).

One possible explanation for the low energy nitrogen and oxygen is that they originate from a galactic source. According to the present theory of solar modulation of cosmic rays, it is difficult to account for the enhancements of the low energy fluxes observed at earth (Fisk, 1974). However, this may result from the inadequacy of present modulation theory.

Fisk et al. (1974) have suggested an alternative explanation. They proposed that the low energy nitrogen and oxygen are due to neutral interstellar particles which penetrate the solar cavity, are singly ionized, and are then accelerated. Since interstellar carbon is mostly ionized (Rogerson et al., 1973), it cannot penetrate the solar cavity. If this theory is correct, it can explain the large oxygen/carbon ratio at low energies in a natural way.

The enhanced nitrogen and oxygen make an interesting topic of study whether they represent a sample of the interstellar medium or of a galactic object of unusual composition. In order to learn more about the nature of the source of the low energy nitrogen and oxygen cosmic rays, we undertook to measure their isotopic composition with the Caltech Electron/Isotope Spectrometer aboard the IMP-7 satellite. A preliminary account of this work has been presented elsewhere (Hurford et al., 1974; Mewaldt et al., 1974b).

II. EXPERIMENT

A. Spacecraft

Two similar versions of the Caltech Electron/Isotope Spectrometer (EIS) were launched in September 1972 and October 1973 aboard the IMP-7 and IMP-8 satellites respectively. The spacecrafts are spin stabilized with the spin axis pointing perpendicular to the ecliptic. The telescope on each spacecraft is mounted perpendicular to the spin axis so that it scans the ecliptic plane as the spacecraft rotates. A list of selected orbital parameters for each satellite is given in Table II - 1. The large orbital radii ensure that the satellites spend more than 2/3 of the time in the interplanetary medium outside the earth's magnetotail.

B. Instrument

Figure II - 1 schematically illustrates the Caltech EIS telescope aboard IMP-7. The telescope consists of a stack of 11 fully depleted silicon surface-barrier solid state detectors, D0-D10, surrounded by a plastic anticoincidence shield, D11, which is viewed by a photomultiplier tube. The dead layers on each side of the detectors are less than 50 $\mu g/cm^2$. A 2.4 mg/cm^2 aluminized mylar window covers the front of the telescope to prevent the sun from illuminating the detectors.

Each detector is connected to a charge-sensitive preamplifier. The outputs of D0-D9 are analyzed by 1024 or 4096 channel analog to digital converters (ADC's), while D10 and D11 are connected

TABLE II - 1

Nominal Orbit Characteristics

of IMP-7 and IMP-8 Satellites

	IMP-7 (9/25/72)	IMP-8 (11/23/73)
Apogee	201,110 km	155,978 km
Perigee	235,607 km	286,129 km
Orbit period	12.3 days	12.5 days
Spin period	1.3 sec	2.6 sec

FIGURE II - 1

Cross section view of the
Caltech Electron/Isotope
Spectrometer on IMP-7.

CALTECH ELECTRON/ISOTOPE SPECTROMETER

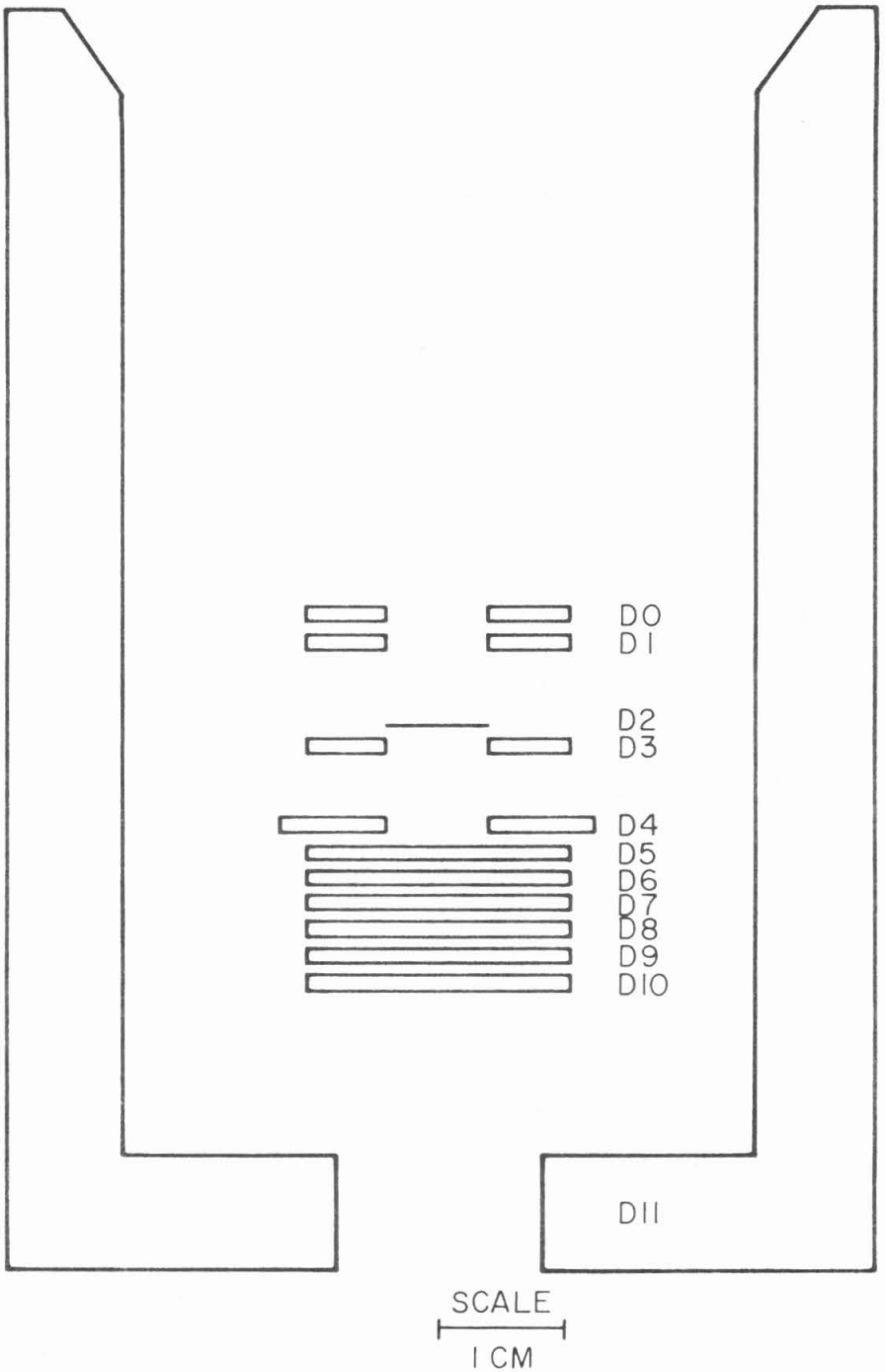

to discriminators. Table II - 2 lists the nominal detector and ADC parameters.

Two types of information are generated by the instrument: event and rate information. Each 0.64 seconds an event is read out. A five-level priority system selects the most interesting event during each 0.64 second interval. For each event the telemetry contains several items of information. The identities of the triggered detectors are telemetered along with 2 pulse heights: the pulse height in the first detector and the sum of the pulse heights in the remaining detectors. In addition, the azimuthal angle of the telescope at the time of the event is retrieved.

The rate data are useful for studying time varying events and for normalizing the event data. Table II - 3 defines the rates that are useful for the present work.

For this study, the primary events of interest are those that trigger D2 and D5 and no other detector. The pulse height information then corresponds to the energy loss in D2 and the energy loss in D5. The annular detectors are active collimators in this analysis mode and provide a clean, low background geometry. Table II - 4 lists the energy range of selected isotopes in D25. Column 1 indicates the energy at which D5 is triggered and the energy at which D6 is triggered. Column 3 indicates the energy intervals contributing to the PHI rate. Note that the low energy limits in column 3 differ from the low energy limits in column 1 since the high discriminator of D5 must be triggered for the PHI rate. (See Table II - 3.)

TABLE II -2

Nominal Detector and ADC Characteristics for IMP-7

Detector	Type	Thickness (μm)	Outer[++] Diameter (mm)	Inner[++] Diameter (mm)	Dead Layer on Each Surface (ug/cm^2)	Discriminator[‡] Threshold (MeV)	ADC[‡] Resolution (MeV)	Number of ADC Channels
D0,D1,D3	annular	1000	22	8	40	0.16	0.165	1024
D4	annular	1000	25	8	40	0.16	0.165	1024
D2	solid	50	9	-	40	0.16 0.4 (D2H)[+]	0.041	1024
D5	solid	1000	21	-	40	0.16 3.2 (D5H)[+]	0.041[*]	4096
D6,D7,D8,D9	solid	1000	21	-	40	0.16	0.165	1024
D10	solid	1000	21	-	40	0.16	-	-

[*] Above channel 1023 the resolution is 0.165 MeV since the least 2 significant bits are deleted from the telemetry.

[+] D2H and D5H represent high level thresholds for the D2 and D5 ADC's.

[‡] Detailed results can be found in the report by Mewaldt and Vidor (1975).

[++] Detailed detector parameters can be found in the report by Hartman (1973).

TABLE II - 3

Selected Rates

Rate	Logic Requirement	Nominal Physical Significance
PLO	N D2H $\overline{d5}$ $\overline{d5h}$ $\overline{d6}$ $\overline{d7}$ $\overline{d10}$ $\overline{aip}$	Low energy nuclei that stop in D2
PHI	N D2 D5H $\overline{d6}$ $\overline{d10}$ $\overline{d11}$	Higher energy nuclei[+] that stop in D5
PEN	N D5 D6 D10 $\overline{d11}$	Charged particles that penetrate the detector stack
DO[*]	DO $\overline{d10}$ $\overline{d11}$	Charged particles that enter DO and stop in the stack
NEUT	N $\overline{d5}$ D7 $\overline{d10}$ $\overline{d11}$	Neutral particles that interact in the detector stack

---

N = narrow geometry = $\overline{d0}$ $\overline{d1}$ $\overline{d3}$ $\overline{d4}$

$\overline{aip}$ = analysis not in progress

[+] See Table II - 4 for energy intervals

TABLE II-4

Calculated IMP-7 Energy Intervals*

	D25 (MeV/nucleon)	D25 Isotope Identification (MeV/nucleon)	PHI Rate (MeV/nucleon)
$^{1}H^{+}$	2.36 - 12.65	2.36 - 12.65	4.30 - 12.65
$^{4}He^{+}$	2.40 - 12.74	2.40 - 12.74	2.68 - 12.74
$^{6}Li^{\ddagger}$	2.87 - 15.86	2.87 - 15.86	3.10 - 15.86
$^{7}Be^{\ddagger}$	3.65 - 20.12	3.65 - 20.12	3.86 - 20.12
$^{11}B^{\ddagger}$	3.50 - 20.00	3.50 - 16.19	3.68 - 20.00
$^{12}C^{\ddagger}$	4.09 - 23.38	4.09 - 15.27	4.27 - 23.38
$^{14}N^{+}$	4.87 - 25.80	5.59 - 13.57	4.93 - 25.80
$^{15}N^{+}$	4.66 - 24.83	5.45 - 12.74	4.71 - 24.83
$^{16}O^{+}$	4.91 - 27.59	6.95 - 12.45	5.05 - 27.59
$^{17}O^{+}$	4.71 - 26.66	6.87 - 11.81	4.84 - 26.66
$^{18}O^{+}$	4.52 - 25.81	6.77 - 11.24	4.65 - 25.81

*Corrected for energy loss in mylar window.

+Based on calibrated instrument response (see Appendix C). H, He accurate to ~ 1%; N, O accurate to ~ 0.2 MeV/nucleon.

‡Based on Janni's (1966) range - energy tables with corrections for electron pickup as given by Northcliffe and Schilling (1970). Accurate to ~ 0.3 MeV/nucleon.

Because of ADC saturation, isotope identification is not possible over the entire D25 energy range. Figure II - 2 illustrates this point. The boundaries of the figure are limited by the number of channels in the D2 and D5 ADC's. The tracks are shown for several isotopes. Elements heavier than carbon saturate the D2 ADC when the particles have just enough energy to enter D5. Elements heavier than beryllium can lose enough energy in D5 to saturate the D5 ADC. Note than in the regions of D2 or D5 ADC saturation, element information is somewhat restricted. For events that saturate D2, only a lower limit can be placed on the charge of the particle. For events that saturate only D5, the element can either be unambiguously identified (for example, boron), or it can be limited to only a few possibilities (for example, either nitrogen or oxygen). Table II - 5 lists the channels and the corresponding energies for which the D2 or D5 ADC is saturated by selected isotopes.

A cross section view of the Caltech Electron/Isotope Spectrometer aboard IMP-8 is shown in Figure II - 3. The basic changes from IMP-7 are the compactness of the detector stack and the replacement of 2 annular detectors by 2 solid detectors. The relevant physical parameters for D25 events on IMP-7 and IMP-8 are given in Table II - 6. The energy intervals on IMP-8 for selected isotopes are given in Table II - 7, and Table II - 8 lists the channels and corresponding energies for which the IMP-8 D2 or D5 ADC is saturated. Except for detector type,

FIGURE II - 2

D2 vs D5 plot illustrating regions of ADC saturation.

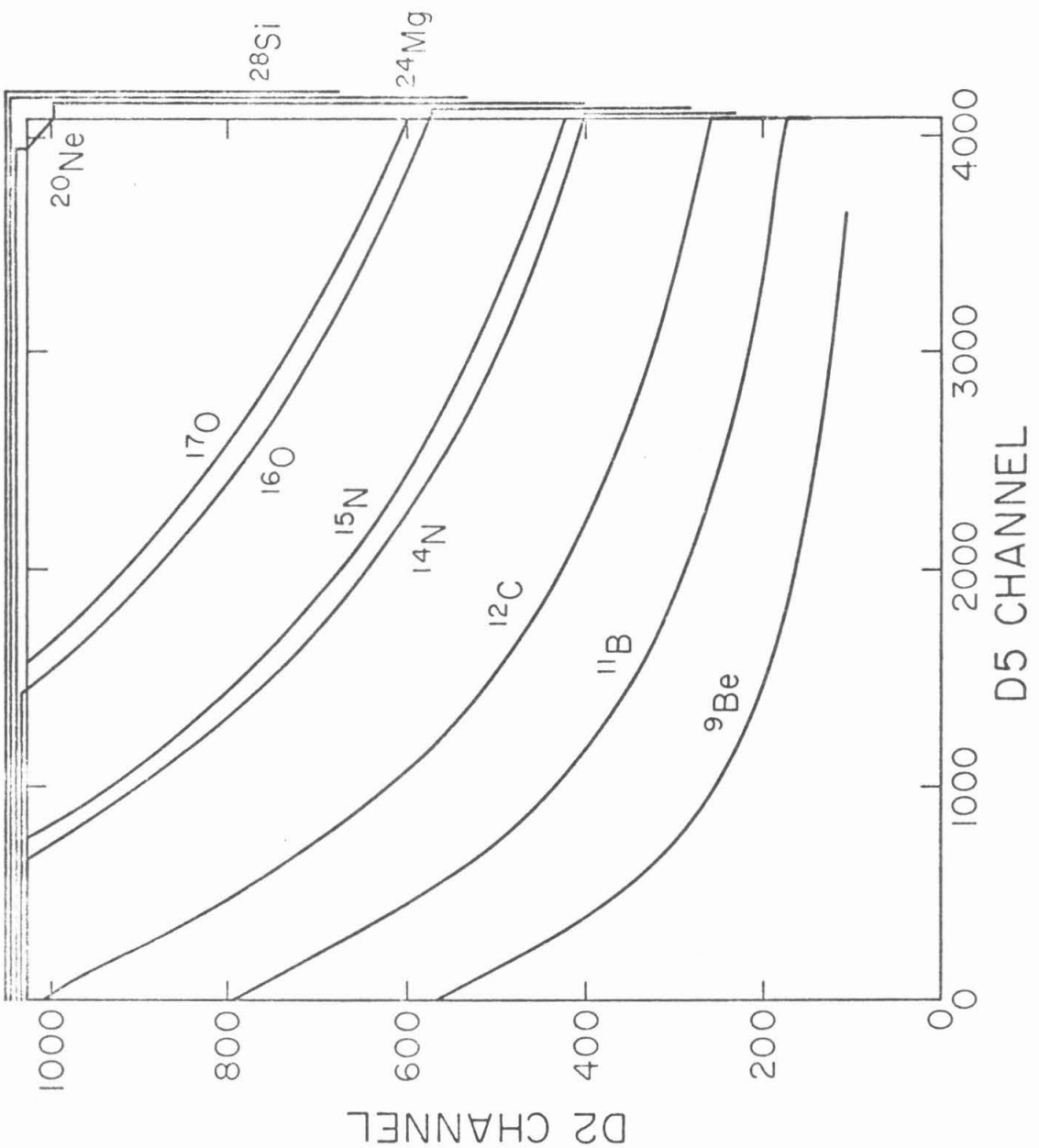
^{28}Si
^{24}Mg
^{20}Ne
^{17}O
^{16}O
^{15}N
^{14}N
^{12}C
^{11}B
^{9}Be
D2 CHANNEL
D5 CHANNEL
0
200
400
600
800
1000
1000
2000
3000
4000

TABLE II - 5

Average Energies of D2 and D5 ADC Saturation for IMP-7*

Isotope	D2 Saturated		D5 Saturated	
	D5 Channels	Energy (MeV/nucleon)	D2 Channels	Energy (MeV/nucleon)
^{11}B			149 - 174	16.2 - 20.0
^{12}C			187 - 262	15.3 - 23.4
^{14}N	0 - 649	4.9 - 5.6	234 - 406	13.6 - 25.8
^{15}N	0 - 731	4.7 - 5.5	241 - 427	12.7 - 24.8
^{16}O	0 - 1423	4.9 - 7.0	288 - 575	12.4 - 27.6
^{17}O	0 - 1557	4.7 - 6.9	296 - 600	11.8 - 26.7
^{18}O	0 - 1677	4.5 - 6.8	303 - 624	11.2 - 25.8
^{20}Ne	0 - 3956	6.2 - 10.8	405 - 1005	11.1 - 31.5
^{24}Mg	0 - 4092	6.9 - 16.1	535 - 3+	10.5 - 34.9
^{28}Si	0 - 4092	7.6 - 23.1	679 - 3+	10.2 - 38.0

*Corrected for energy loss in mylar window. Energies are calculated from range - energy tables and are accurate to ~ 0.3 MeV/nucleon. D2 channels are accurate to ~ 3 channels. D5 channels are accurate to 20 channels. Note that,due to resolution effects (see Section II - C),the actual spread in channels may be larger than the errors quoted for the mean channel numbers.

+The D2 ADC saturates at channel 3. Highest energy D2 channels are: ..., 1021, 1022, 1023, 0, 1, 2, 3.

FIGURE II - 3

Cross section view of the Caltech Electron/Isotope Spectrometer on IMP-8.

IMP-J
CALTECH ELECTRON/ISOTOPE SPECTROMETER

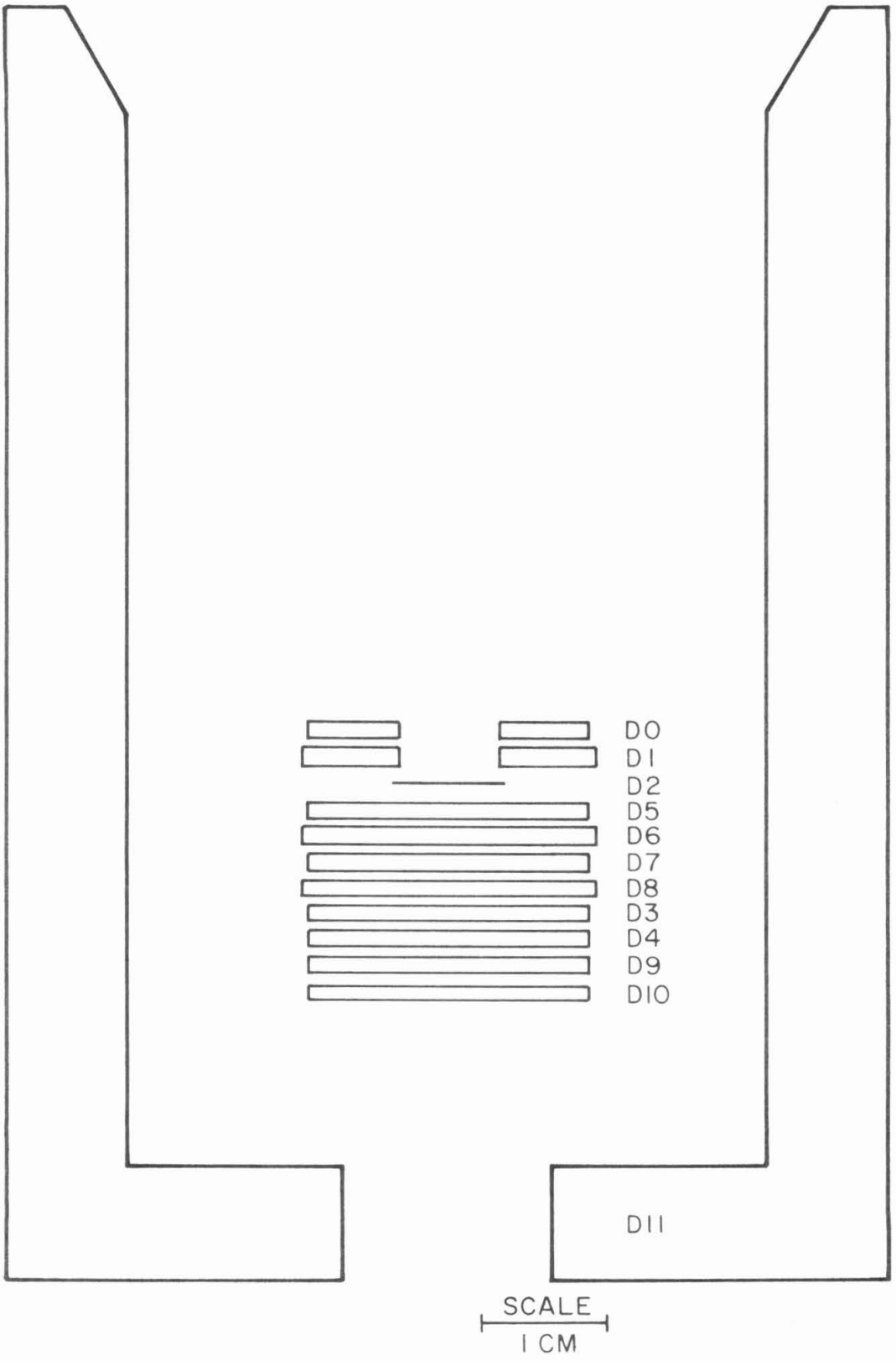

TABLE II - 6

Physical Parameters for IMP-7 and IMP-8 D25 Events

	IMP-7	IMP-8
Geometrical Factor*($cm^2 sr$)	0.069 ± .005	0.232 ± .01
Average secant θ*	1.0234	1.0459
Maximum θ* (degrees)	23.6	26.7
D2 thickness+ (μm silicon)	47.36 ± .1	46.7 ± .5
Window thickness‡ (mg/cm^2 mylar)	2.4 ± .1	3.2 ± .2

*Calculated from physical dimensions of detector system. (Hartman, 1973; Vidor, 1974).

+Normalized to flight data. Quoted errors assume electronic calibration known precisely.

‡Measured with 6.051 MeV and 8.785 MeV α-particles from ^{212}Pb.

TABLE II - 7

Calculated IMP-8 Energy Intervals*

	D25 (MeV/nucleon)	D25 Isotope Identification (MeV/nucleon)	PHI Rate (MeV/nucleon)
$^{1}H^{+}$	2.49 - 12.97	2.49 - 12.97	4.39 - 12.97
$^{4}He^{+}$	2.53 - 13.06	2.53 - 13.06	2.80 - 13.06
$^{6}Li^{\ddagger}$	3.04 - 16.26	3.04 - 16.26	3.26 - 16.26
$^{7}Be^{\ddagger}$	3.87 - 20.63	3.87 - 20.63	4.07 - 20.63
$^{11}Be^{\ddagger}$	3.72 - 20.51	3.72 - 16.18	3.89 - 20.51
$^{12}C^{\ddagger}$	4.35 - 23.97	4.35 - 15.26	4.52 - 23.97
$^{14}N^{+}$	5.15 - 26.44	5.89 - 13.66	5.19 - 26.44
$^{15}N^{+}$	4.92 - 25.44	5.74 - 12.81	4.97 - 25.44
$^{16}O^{+}$	5.21 - 28.28	7.29 - 12.58	5.35 - 28.28
$^{17}O^{+}$	5.00 - 27.33	7.17 - 11.90	5.13 - 27.33
$^{18}O^{+}$	4.80 - 26.46	7.05 - 11.32	4.93 - 26.46

*Corrected for energy loss in mylar window.

+Based on calibrated instrument response. H, He accurate to ~ 1%; N, O accurate to ~ 0.2 MeV/nucleon.

‡Based on Janni's (1966) range - energy tables with corrections for electron pickup as given by Northcliffe and Schilling (1970). Accurate to ~ 0.3 MeV/nucleon.

TABLE II - 8

Average Energies of D2 and D5 ADC Saturation for IMP-8*

Isotope	D2 Saturated		D5 Saturated	
	D5 Channels	Energy (MeV/nucleon)	D2 Channels	Energy (MeV/nucleon)
^{11}B			149 - 178	16.2 - 20.5
^{12}C			188 - 268	15.3 - 24.0
^{14}N	0 - 686	5.1 - 5.9	234 - 413	13.7 - 26.4
^{15}N	0 - 770	4.9 - 5.7	241 - 435	12.8 - 25.4
^{16}O	0 - 1485	5.2 - 7.3	288 - 584	12.6 - 28.3
^{17}O	0 - 1612	5.0 - 7.2	295 - 611	11.9 - 27.3
^{18}O	0 - 1731	4.8 - 7.1	303 - 636	11.3 - 26.5
^{20}Ne	0 - 4057	6.6 - 11.2	393 - 1021	11.2 - 32.3
^{24}Mg	0 - 4092	7.3 - 16.6	521 - 3+	10.7 - 35.7
^{28}Si	0 - 4092	8.0 - 23.6	662 - 3+	10.5 - 39.0

*Corrected for energy loss in mylar window. Energies are calculated from range - energy tables and are accurate to ~ 0.3 MeV/nucleon. D2 channels are accurate to ~ 3 channels. D5 channels are accurate to ~ 20 channels. Note that, due to resolution effects (see Section II - C), the actual spread in channels may be larger than the errors quoted for the mean channel numbers.

+The D2 ADC saturates at channel 3. Highest energy D2 channels are: ..., 1021, 1022, 1023, 0, 1, 2, 3.

Table II - 2 closely represents the nominal detector and ADC parameters for IMP-8. A more detailed description of the EIS experiments on IMP-7 and IMP-8 can be found in the report by Garrard (1974a).

The IMP-8 EIS has a larger geometrical factor than the IMP-7 EIS for D25 events. However, the trade-off is that the mass resolution is worse for IMP-8. Therefore, in order to obtain the best possible mass resolution, the isotope data presented here will be from the IMP-7 experiment.

C. Isotope Response

The isotope identification technique, herein referred to as the ΔE - E' technique, used for this experiment will now be described. A particle of mass M, charge Z, and energy E will, through ionization energy loss, deposit an average energy ΔE in D2 and a residual energy E' in D5. If the range-energy relation of the isotope is known, ΔE and E' can be calculated. Otherwise, ΔE and E' can be determined from a calibration. If the energy of the isotope is varied, the result is a track on a ΔE - E' plot. (See for example, Figure II - 2.) For a more detailed discussion of the range - energy relation and the isotope tracks, the reader is referred to Appendix C.

In reality the ΔE and E' form a distribution about the average mass track. A nonintegral mass can be assigned to the particle by interpolating between neighboring mass tracks. (In practice equation C - 4 is used to calculate the mass.)

The distribution of particles about the mass track implies a finite mass resolution. Since the calculated mass M ($\Delta E, E', T$) is a function of ΔE, E', and the thickness T of D2, a variation in any of these quantities results in a variation in the calculated mass. The mass variation can be expressed as:

$$\sigma_M^2 = \left(\frac{\partial M}{\partial T}\right)^2_{\Delta E,\, E'} \sigma_T^2 + \left(\frac{\partial M}{\partial \delta E}\right)^2_{E,\, T} \sigma_{\delta E}^2$$

$$+ \left(\frac{\partial M}{\partial \Delta E}\right)^2_{E',\, T} \sigma_{\Delta E}^2 + \left(\frac{\partial M}{\partial E'}\right)^2_{\Delta E,\, T} \sigma_{E'}^2 \qquad \text{II - 1}$$

where σ_M, σ_T, $\sigma_{\delta E}$, $\sigma_{\Delta E}$, and $\sigma_{E'}$, are, respectively, the rms deviations of the calculated mass, of the pathlength in the ΔE detector, of the energy loss ΔE due to ionization energy loss fluctuations, of the measured energy loss ΔE due to noise and channel width, and of the measured energy loss E' due to noise and channel width.

The largest contribution to the mass resolution for the nitrogen and oxygen D25 events is the uncertainty in the pathlength in D2. This pathlength uncertainty is due to the spread in acceptance angles and to the intrinsic thickness variations of D2. Since D2 has a slightly concave shape, the two effects are correlated. From Figure II - 1 it can be seen that the

trajectories which deviate the most from perpendicular incidence must pass near the center of D2, which is also the thinnest region of the detector. Therefore the pathlength variations due to angle are partly compensated by the concave shape of D2. The D2 thickness profile was measured with an 8.785 MeV α - beam from a collimated ^{212}Pb source. The pathlength variation was obtained from a Monte Carlo calculation which incorporated both angle and thickness effects.

Energy loss fluctuations in D2 are a second contribution to the mass resolution. Since ionization energy loss is a statistical process, a particle with energy E travelling through a thickness T of D2 will not always lose the same energy ΔE in D2 (Seltzer and Berger, 1964). For the particle types and energies considered here, the standard deviation in MeV of the energy loss in D2 is given by (Hurford, 1974)

$$\sigma_{\delta E} = 0.435 \; Z\sqrt{T} \qquad D \sqrt{\frac{1 - \beta^2/2}{1 - \beta^2}} \qquad \text{II - 2}$$

where β is the velocity of the incident particle relative to the velocity of light, Z is the charge of the incident particle in units of proton charge, T is the thickness of D2 in cm, and D is a deceleration factor of order unity that corrects for the change of velocity as the particle traverses the detector.

$$D = \sqrt{1 - 0.8705 \left[1 + R/T \ln (1 - T/R) \right]} \qquad \text{II - 3}$$

where R is the range of the incident particle in cm.

The uncertainty in the ΔE and E' measurements make a relatively small contribution to the nitrogen and oxygen mass resolution. The variations in the ΔE and E' measurements are due to 2 effects: electronic noise and intrinsic channel width, which can be combined in quadrature to give the total rms variation.

The contributions to the IMP-7 EIS mass resolution are given in Table II - 9. Although the resolution is calculated for discrete energies, the total mass resolution is within 0.05 amu of the values in Table II - 9 for all energies at which isotope identification is possible.

It should be noted that the relative size of the individual contributions is a function of the isotope. As an example, for 10 MeV protons the contributions in order of decreasing importance are (Hurford, 1974): ionization energy loss fluctuations, uncertainty in the ΔE measurement, pathlength variations, and uncertainty in the E' measurement. This contrasts with ^{16}O, for which the dominant contribution is the pathlength uncertainty. For D25 events the pathlength variation tends to increase in relative importance for the heavier elements.

TABLE II - 9

Contributions to IMP-7 Mass Resolution

Parameter	Significance	Value	Equivalent σ_M (amu) ^{14}N (7.6 MeV/nuc)	Equivalent σ_M (amu) ^{16}O (8.5 MeV/nuc)
σ_T	Rms pathlength uncertainty in D2	0.85μm	0.336	0.388
$\sigma_{\delta E}$	Rms ionization energy loss fluctuation in D2	0.233 MeV(^{14}N) 0.261 MeV(^{16}O)	0.148	0.163
$\sigma_{\Delta E}$	D2 rms noise	0.023 MeV		
	D2 channel width*	0.041 MeV		
	Rms error in ΔE measurement	0.026 MeV	0.020	0.020
$\sigma_{E'}$	D5 rms noise	0.014 MeV		
	D5 channel width*	0.166 MeV		
	Rms error in E' measurement	0.050 MeV	0.004	0.003
σ_M	Total rms mass resolution		0.368	0.421

*Rms deviation in energy measurement due to channel width W is $W/\sqrt{12}$

D. Calibrations

The calibrations can be conveniently divided into 2 classes: electronic and particle calibrations. Those calibrations which are pertinent to the discussion of cosmic ray nuclei will be discussed.

Each ADC contains an internal test pulser. To perform electronic calibrations, the internal test pulsers were initially calibrated against the energy loss of α - particles from an ^{241}Am source. This initial calibration related the voltage used in conjunction with the pulsers to the energy of the α - particle. Since the voltage - energy relation is linear, the pulser could then be used to determine the energy corresponding to the ADC channel thresholds (Mewaldt and Vidor, 1975).

The linearity and the stability of the gain and offset were investigated over a period of 8 1/2 months. The linearity and gain stability are listed in Table II - 10 along with the effect on the calculated mass of an ^{16}O particle. Note the extremely small error in mass determination due to calibration uncertainties. The linearity of the system allows us to use only the 2 parameters of gain and offset to calculate the thresholds of the higher channels.*

---

*The gain and offset are used to calculate energy thresholds for D2 and D5 channels above 400. Below channel 400 the thresholds are calculated by linear interpolation from a set of calibrated channel thresholds.

TABLE II - 10

Linearity and Stability of IMP-7 Detector Electronics

	D2		D5	
	MeV	ΔM for ^{16}O (amu)	MeV	ΔM for ^{16}O (amu)
Linearity*	0.009	0.008	0.026	0.005
Gain stability (full scale)+	0.012	0.008	0.20	0.02
Offset stability‡	0.013	0.011	0.003	0.0006

*Linearity is the deviation in channel threshold from the value obtained by linear interpolation between channels 100 and 1000 for D2 and between channels 400 and 4000 for D5. Table applies only to channels above 20.

+Measured over period of 8 1/2 months of calibrations. (Maximum deviation from mean).

‡For each of 3 periods of flight data during which offset was stable (9/30/72 - 3/26/73; 3/27/73 - 6/4/73; 6/5/73 - 10/22/74). (Maximum deviation from mean).

ΔM is evaluated at the maximum ADC channel for gain errors and at the minimum channel for linearity and offset errors.

The offset was not as stable as the gain over long time periods. However, for the IMP-7 instrument the D2 and D5 pulse heights are read out for certain types of events in which the detectors are not triggered, thus providing an in-flight calibration of the offset. For the post-launch data, a correction factor to the offset was derived for each of 3 time periods. Table II - 10 represents the variations in the offset in each of these time periods.

Calibrations with isotopes of hydrogen and helium at several angles of incidence and at several energies were done at the Caltech Tandem van de Graaff accelerator. These calibrations confirmed the predicted mass resolution of hydrogen and helium. For a more detailed discussion of the Tandem van de Graaff calibrations, the reader is referred to Hurford (1974) and Vidor (1975).

A calibration of a spare telescope identical to that on IMP-8 was done with a variety of isotopes of charge $1 \leq Z \leq 8$ at the Berkeley 88" Cyclotron. The main result of the calibration was the accurate determination of the mass response for selected isotopes. This aspect of the calibration is described in Appendix C. In addition, the technique of calculating the mass resolution was tested with elements up through oxygen, and an estimate was obtained of the background level relevant to isotope separation.

A histogram of the observed mass distribution is shown in Figure II - 4 for a portion of the ^{16}O calibration data. Superimposed on the histogram is a Gaussian curve with a 0.30 amu σ and a height normalized to the 19,929 events in the histogram. The width of the curve was determined from equation II - 1 and the parameters of the detector system.* The Gaussian curve is a reasonable fit, although not the best fit, to the peak of the histogram. However, the Gaussian curve does not fit the tails of the mass histogram. On the low mass side especially, the number of events in the histogram is significantly larger than predicted by the Gaussian curve. If the tails of the distribution are due to the intrinsic response of the instrument to an ^{16}O beam, then we can estimate the background level affecting isotope resolution. At 15 and 14 amu the non-Gaussian tails are respectively 2 and 3 orders of magnitude below the histogram peak. At 17 amu the tail

---

*The D2 rms thickness variation of 0.5μ was a free parameter obtained from the cyclotron calibration data (excluding the data in Figure II - 4) by fitting the mass resolution of the isotopes of several elements. This compares with a value of 0.6 $\pm$ .1μ obtained by scanning the detector with a collimated α - source. The dominant source of the 0.6μ variations were thickness fluctuations on a scale smaller than the 1/16" diameter of the α - beam. The energy fluctuations in D2 were measured directly. The small scale thickness variations were then obtained by subtracting out the contributions of ionization energy loss fluctuations and noise from the total measured energy fluctuations.

FIGURE II - 4

Mass histogram for oxygen particles depositing between 148.0 and 151.5 MeV in D25. The ^{16}O beam was obtained at the Berkeley 88" Cyclotron. The superimposed Gaussian curve represents the predicted mass response.

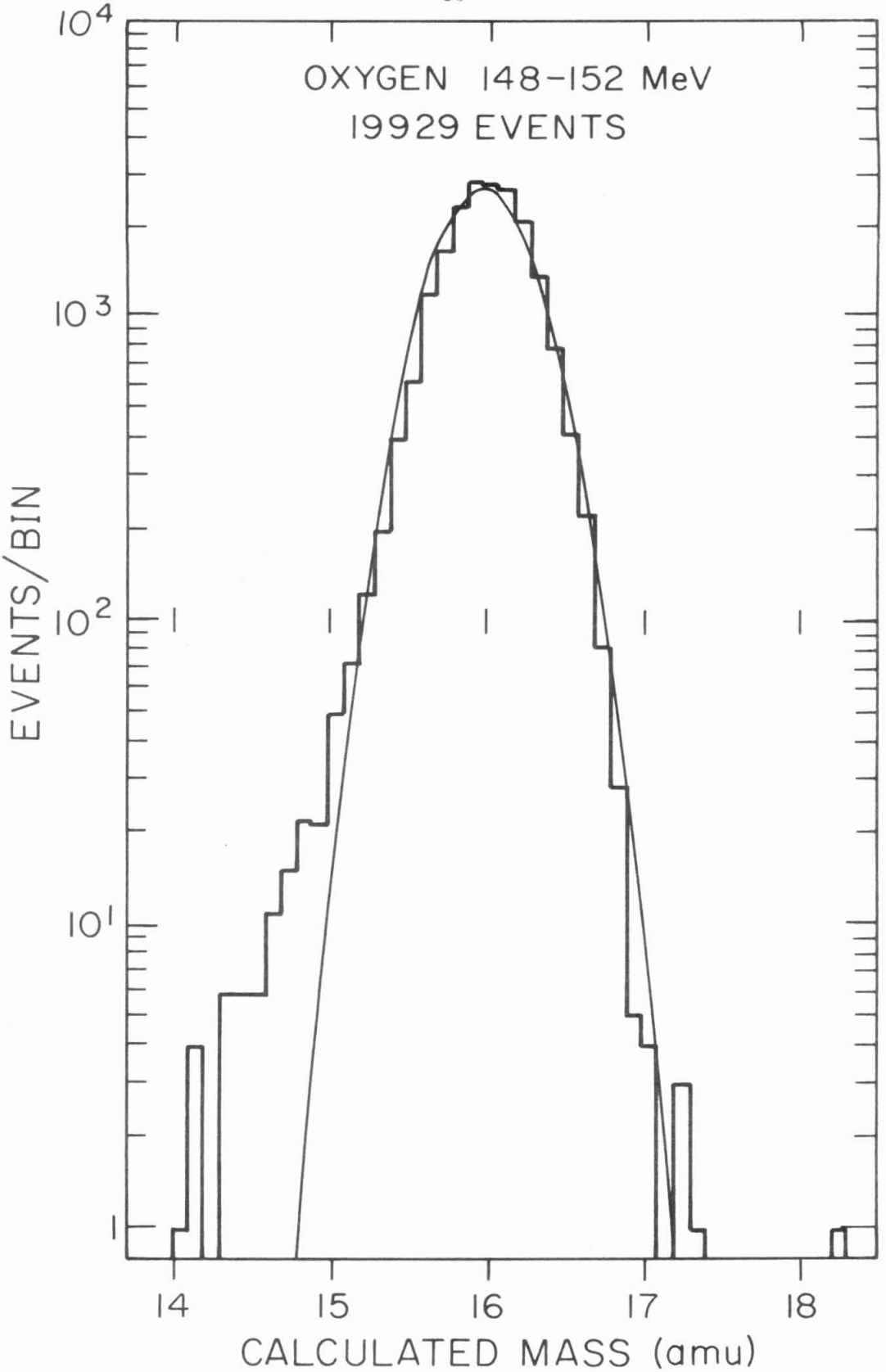
OXYGEN 148–152 MeV
19929 EVENTS
EVENTS/BIN
10^4
10^3
10^2
10^1
1
14
15
16
17
18
CALCULATED MASS (amu)

is 3 orders of magnitude below the peak. There is only 1 event at 18.0 ± .5 amu out of a total of 19,929 events in the histogram. The background level due to a normally incident ^{16}O beam is therefore extremely small, especially on the high mass side. Note that the spare telescope calibrated at the cyclotron is not the same telescope that is aboard the IMP-7 or IMP-8 satellite. Therefore, there is always the possibility that the response of the spare telescope does not simulate the response of the flight instrument. However, we see no reason for any fundamental difference between the responses of the spare and flight telescopes.

Using the measured detector parameters, the mass resolution was calculated as a function of isotope for 8.5 MeV/nucleon particles. Figure II - 5 is a plot of the calculated mass resolution vs. nuclear charge for selected isotopes. The observed mass resolution from the cyclotron calibration is shown for comparison. The dashed error bars on the data points indicate errors that are caused by lack of reproducibility, as opposed to errors due to statistics. The cause of the non-reproducibility has not been investigated. However, one possible source may be that the non-Gaussian tails of the mass distribution are not being excluded in an identical manner from run to run. The variation in the ratio Z/A for the isotopes is the primary reason that the calculated resolution vs. nuclear charge is not monotonic. The dominant sources of the rms mass resolution range from energy loss fluctuations for protons to pathlength variations for oxygen.

FIGURE II - 5

Mass resolution as a function of charge for selected isotopes at 8.5 MeV/nucleon. The solid line indicates the predicted mass resolution. Dotted error bars indicate uncertainties dominated by lack of reproducibility, while solid error bars indicate uncertainties dominated by statistics.

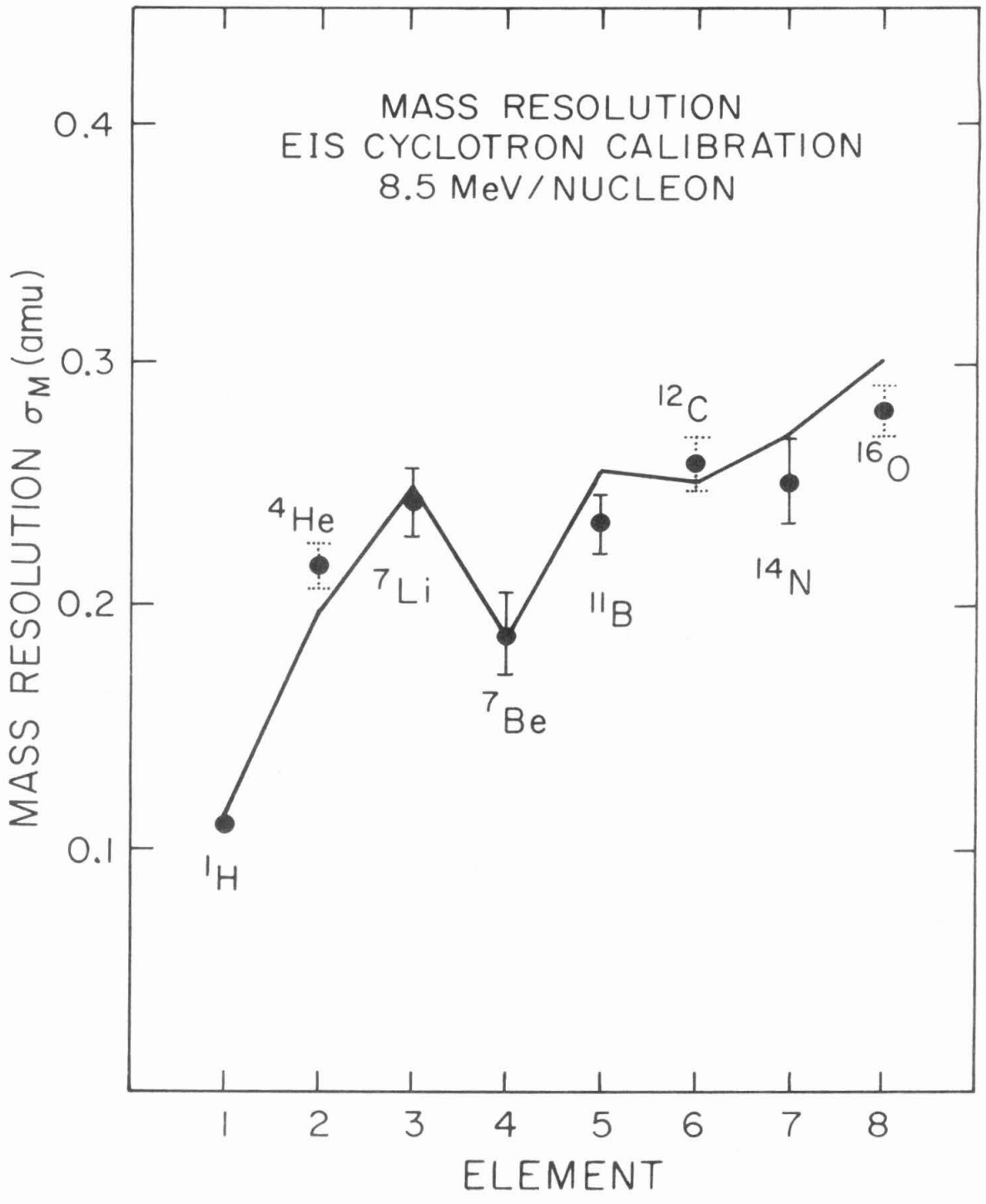
MASS RESOLUTION
EIS CYCLOTRON CALIBRATION
8.5 MeV/NUCLEON
MASS RESOLUTION σ_M (amu)
0.4
0.3
0.2
0.1
^{1}H
^{4}He
^{7}Li
^{7}Be
^{11}B
^{12}C
^{14}N
^{16}O
1
2
3
4
5
6
7
8
ELEMENT

The agreement between the observed and calculated mass resolution over a large charge interval confirms the accuracy of the calculation technique to better than 10%.

III. OBSERVATIONS

A. Definition of Quiet Time Data

The combined flux of solar and galactic cosmic ray nuclei from 4 - 13 MeV/nucleon has been observed to vary by more than 5 orders of magnitude over a 2 year span. The higher fluxes are correlated with solar particle emission, with the largest fluxes associated with solar flares. In order to study the quiescent flux of nitrogen and oxygen cosmic rays, it is necessary to select periods that minimize contamination by solar flare particles. The selection criterion makes use of the instrument's PHI rate, which is sensitive to protons from 4.30 - 12.65 MeV and to alpha particles from 2.68 - 12.74 MeV/nucleon. (See Table II - 4).

If the relative elemental abundances are independent of the particle flux from a solar flare, one expects the solar oxygen flux to vary linearly with the solar hydrogen and helium flux, which is monitored by the PHI rate. Figure III - 1 is a plot of the 6.3 - 8.2 MeV/nucleon carbon, nitrogen, and oxygen (CNO) rate vs. the daily average PHI rate for the 22 months of IMP-7 data from October, 1972 - July, 1974. The CNO rate was measured with a single detector DO, which, because of its large geometrical factor, gives good statistical precision. The absolute fluxes derived this way agree with the results of other investigators (Mewaldt et al., 1974a).

FIGURE III - 1

IMP-7 6.3 - 8.2 MeV/nucleon CNO rate vs. PHI rate from October, 1972 - July, 1974. The solid line represents the least-squares fit to the data. The dashed lines represent the 2 contributions to the solid line.

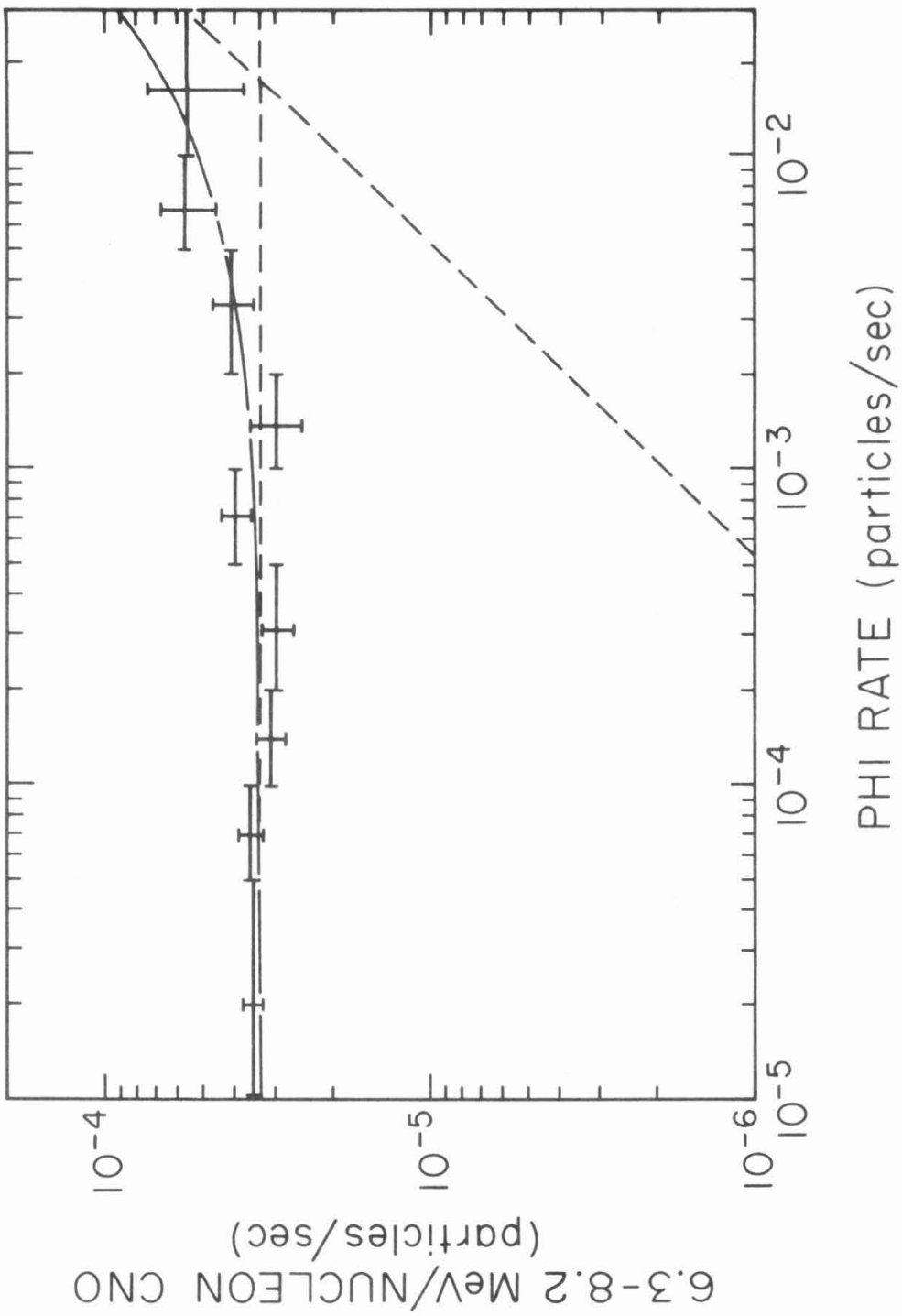
6.3-8.2 MeV/NUCLEON CNO
(particles/sec)
10^{-4}
10^{-5}
10^{-6}
10^{-5}
10^{-4}
10^{-3}
10^{-2}
PHI RATE (particles/sec)

For PHI rates $\leq 10^{-3}$/second, the CNO flux is relatively independent of the PHI rate. Therefore, the amount of solar contamination of the CNO must be small. A least squares fit to the data was performed using a functional form

$$R_{CNO} = a + bR_{PHI}$$

where R_{CNO} and R_{PHI} are the CNO and PHI rates respectively, and a and b are the fitted parameters. The results for a and b are $3.4 \pm .1 \times 10^{-5}$ and $1.9 \pm .8 \times 10^{-3}$ with a reduced χ^2 of 1.2. The best fit and the contributions of the 2 terms are shown in Figure III - 1. The contribution of the linear term at PHI = 10^{-3}/sec is $0.054 \pm .022$ of the total, and at PHI = 2×10^{-4}/sec (average PHI rate for PHI $\leq 10^{-3}$/sec) the contribution is $0.011 \pm .005$.

The preceeding argument has shown that a PHI rate of 10^{-3}/sec is a reasonable upper limit for the quiescent CNO data. Days on which the average IMP-7 PHI rate $\leq 10^{-3}$/sec will be referred to as solar quiet periods, and days on which the PHI rate $> 10^{-3}$/sec will be referred to as solar active periods.

The solar contamination to the flux of element Z can best be estimated by expressing the flux as a fraction of the CNO flux.

$$J_{Z,F} = f_{Z,F} \; J_{CNO,F}$$

where $J_{Z,F}$ and $J_{CNO,F}$ are, respectively, the fluxes of element Z and of CNO during solar flares, and $f_{Z,F}$ is the relative abundance of element Z to CNO during solar flares. Similarly,

$$J_{Z,PHI} = f_{Z,PHI} \quad J_{CNO,PHI}$$

where the subscript PHI refers to the fluxes and relative abundances for a given PHI rate interval rather than for a solar flare. Note that the value of $f_{Z,PHI}$ depends on the chosen PHI interval. Dividing the first equation by the second,

$$\frac{J_{Z,F}}{J_{Z,PHI}} = \frac{f_{Z,F}}{f_{Z,PHI}} \quad \frac{J_{CNO,F}}{J_{CNO,PHI}} \qquad \text{III - 1}$$

Taking as the PHI interval PHI $\leq 10^{-3}$/sec, the quantity on the left hand side of the equation is the relative solar contribution to the flux of element Z for PHI $\leq 10^{-3}$/sec, and it can be calculated from the known quantities on the right hand side of the equation. The ratio $J_{CNO,F} \,/ J_{CNO,PHI}$ is just the solar contribution to the CNO flux. For PHI $\leq 10^{-3}$sec this ratio was previously determined to be 0.011 ± .005 in the energy interval 6.3 - 8.2 MeV/nucleon. The quantity $f_{Z,F}$ is obtained from the literature. (See, for example, Teegarden et al., 1973.) We shall approximate the quantity $f_{Z,PHI}$ from 6.3 - 8.2 MeV/nucleon by its known value from

5 - 12.5 MeV/nucleon. (See Section III - C for a calculation of $f_{Z,\ PHI}$.) Table III - 1 lists the solar contribution to the Z = 3 - 8 fluxes as computed from equation III - 1. At energies of ~ 6 - 8 MeV/nucleon, there is no significant solar contribution to any of the fluxes listed in Table III - 1 for a PHI rate $\leq 10^{-3}$/sec.

The data sets used in this thesis are for quiet times, with one exception. Table III - 2 summarizes the data sets used.

B. Energy Spectra

In order to obtain the elemental energy spectra, the IMP-8 data were used. There are 2 reasons for using IMP-8 rather than IMP-7 data. First, the larger geometrical factor of IMP-8 results in better statistical precision. Second, on the IMP-7 instrument the cross-talk between detectors (see Appendix B) makes the absolute flux normalization less certain.

Since the geometrical factor of D25 events for IMP-8 is more than 3 times as large as for IMP-7 (see Table II - 6), the PHI rate for IMP-8 is also more than 3 times as large. Therefore, the criterion for solar quiet times on IMP-8 of PHI $\leq 3 \times 10^{-3}$ events/sec guarantees minimal contamination by solar flare particles.

TABLE III - 1

Solar Contribution to Quiet Time Fluxes (PHI $\leq 10^{-3}$/sec)

Element	$f_{Z,PHI}$ Relative Quiet Time Abundance*	$f_{Z,F}$ Relative Solar Flare Abundance+	Fraction Solar Flare Contribution to Quiet Time Flux
Li	$0.014 \begin{smallmatrix} + .032 \\ - .014 \end{smallmatrix}$	< 0.002	
Be	< 0.022	< 0.002	
B	$0.007 \begin{smallmatrix} + .016 \\ - .006 \end{smallmatrix}$	< 0.005	< 0.05
C	$0.026 \begin{smallmatrix} + .021 \\ - .013 \end{smallmatrix}$	0.31 ± .02	0.13 ± .10
N	0.13 ± .03	0.072 ± .007	0.006 ± .003
O	0.85 ± .03	0.62 ± .01	0.008 ± .004
CNO	1.00	1.00	0.011 ± .005

*See TABLE III - 3

+September 1, 1971 flare (Teegarden et al., 1973)

TABLE III - 2

Data Sets Used in Thesis

DATE SET	INCLUSIVE DATES	IMP SATELLITE	RESTRICTIONS	NUMBER OF DAYS INCLUDED*	PURPOSE
1	10/1/72-7/31/74	7		662	D25 CNO vs. PHI (Figure III - 1)
2	10/31/73-9/25/74	8	PHI $\leq 3 \times 10^{-3}$/sec	210	He, C, N, O, spectra (Figure III - 4) Elemental spectra (Figures III - 4, 5)
3	9/30/72-10/22/74	7	PHI $\leq 10^{-3}$/sec D4 enabled	470	Elemental abundances (Table III - 3) and mass abundances (Figures III - 7,8,9; Tables III - 4,6)

*Excludes several days not analyzed because of data gaps.

Figure III - 2 is a ΔE-E' plot of the Z >3 IMP-8 quiet time data which were used to obtain energy spectra and element abundances. For clarity, events that saturate the D2 or D5 ADC are not shown. Except for beryllium, the bands used to distinguish real particles from background extend $\pm$ 2.5 amu from the isotope which is dominant at higher energies. Since the IMP-8 rms mass resolution is ~ 1 amu for oxygen and is smaller for the lighter elements, the bands exclude fewer than 5% of the real particles. For beryllium the band extends from 6 - 11 amu so that the isotopes ^{7}Be, ^{9}Be, and ^{10}Be fall within the allowed band. Since the beryllium mass resolution is better than the oxygen mass resolution, fewer than 7% of the real ^{7}Be and ^{10}Be particles are excluded by the boundaries 1 amu away.

It was previously pointed out that element information could also be obtained from events that saturate the D2 or D5 ADC (see Section II - B). To extend the energy range of the spectra, we made use of data in the saturation regions. The IMP-8 quiet time events that saturate the ADC's are plotted in Figure III - 3. Also shown are the expected channel intervals for selected elements.

FIGURE III - 2

IMP-8 quiet time D25 data for $Z > 3$ from October 31, 1973 - September 25, 1974. No data below the dashed line are included in the plot. The $Z = 5 - 8$ element bands are centered on ^{11}B, ^{12}C, ^{14}N, and ^{16}O and are 5 amu wide. The $Z = 4$ band extends from 6 - 11 amu. The dotted lines of constant energy indicate the energies for which the element abundances of Table III - 3 were determined. The highest energies correspond to the energy (in MeV/nucleon) at which ^{16}O saturates the D5 ADC, and the lowest energies, except for ^{14}N, correspond to the energy at which ^{16}O enters D5.

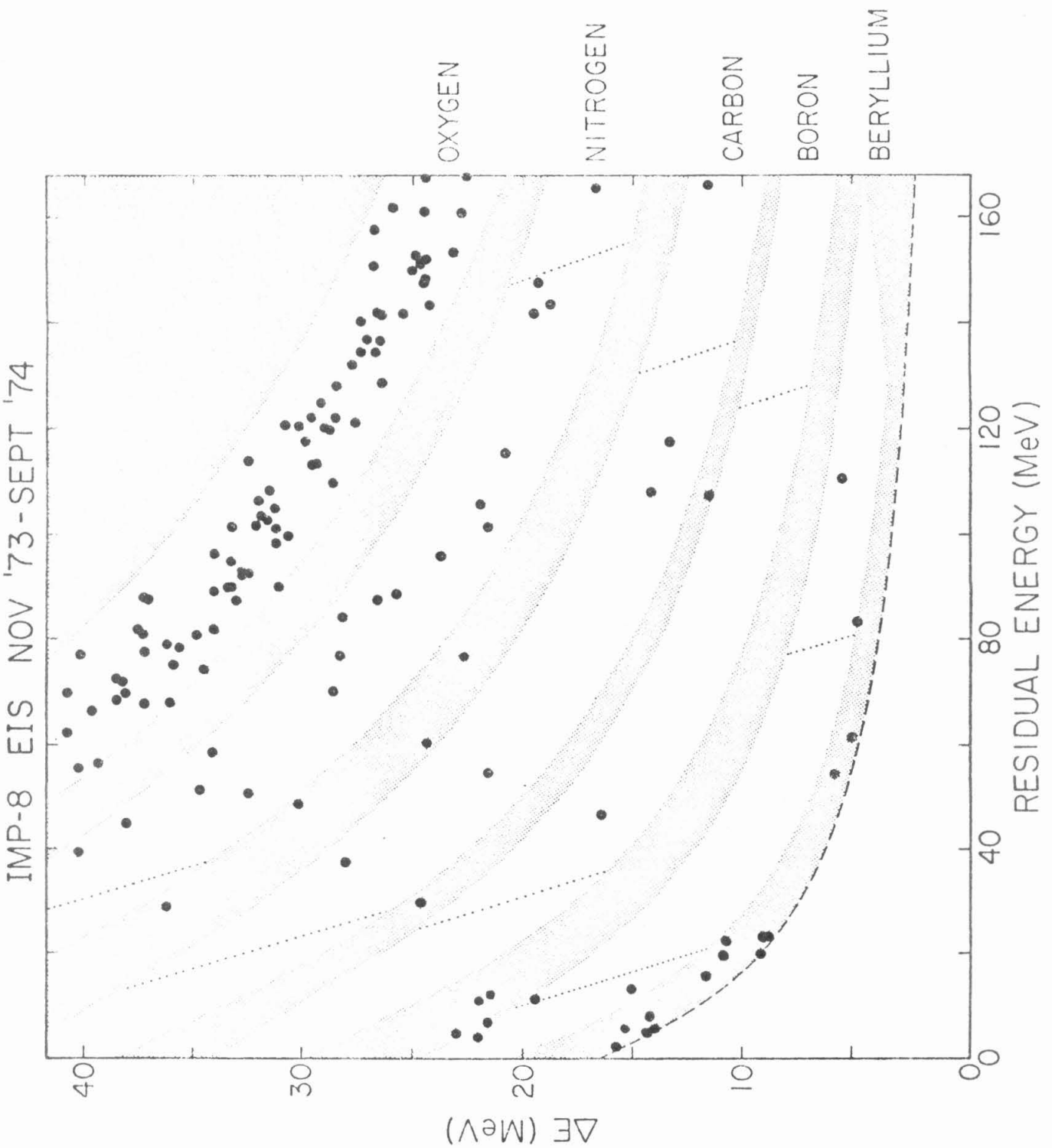
IMP-8 EIS NOV '73-SEPT '74
OXYGEN
NITROGEN
CARBON
BORON
BERYLLIUM
ΔE (MeV)
RESIDUAL ENERGY (MeV)
0
10
20
30
40
0
40
80
120
160

FIGURE III - 3

IMP-8 quiet time data from October 31, 1973 - September 25, 1974 for events that saturate the D2 or D5 ADC. The channels for which selected elements can saturate the D2 or D5 ADC are indicated on the plot. (Compare with Table II - 8.) The events in the highest bin in each plot saturate both the D2 and D5 ADC's.

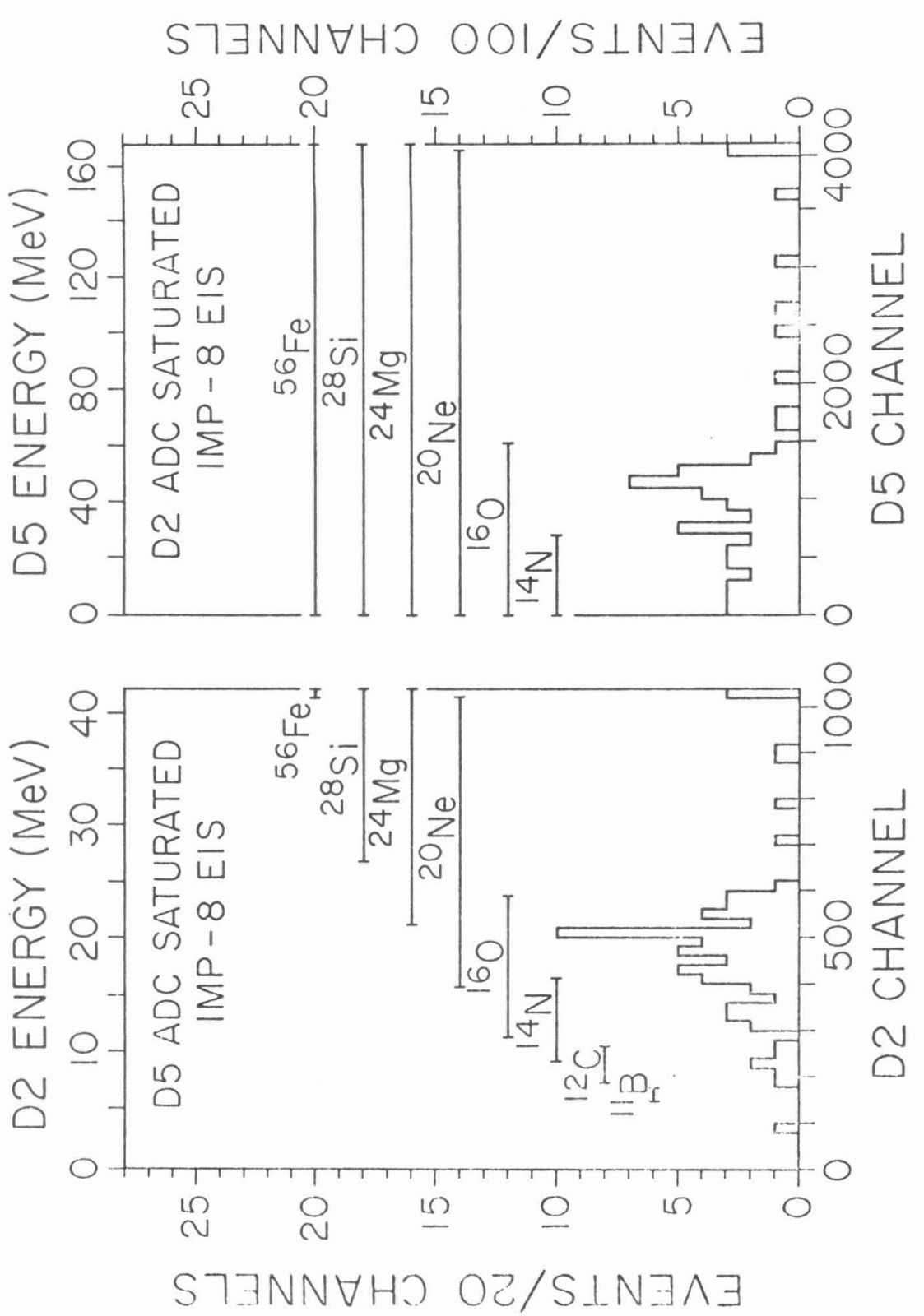
D2 ENERGY (MeV)
D5 ADC SATURATED
IMP-8 EIS
$^{56}Fe_H$
^{28}Si
^{24}Mg
^{20}Ne
^{16}O
^{14}N
^{12}C
$^{11}B_f$
EVENTS/20 CHANNELS
D2 CHANNEL
D5 ENERGY (MeV)
D2 ADC SATURATED
IMP-8 EIS
^{56}Fe
^{28}Si
^{24}Mg
^{20}Ne
^{16}O
^{14}N
EVENTS/100 CHANNELS
D5 CHANNEL

Note that there is a single event that saturated the D5 ADC with a D2 channel less than 149. This event falls outside the expected channel range for any real particle and can therefore be attributed to background. Since the background typically decreases with increasing pulse height (compare with Figure III - 6), an upper limit to the background can be estimated for events that saturate D5. If there is one background event for every 150 D2 channels, then there are 2 background events out of a total of 51 in the energy region for which oxygen saturates the D5 ADC. We can also estimate how far the observed channel numbers deviate from the expected channel numbers due to instrumental resolution. The highest expected D2 channel for an ^{16}O event that saturates D5 is channel 584, while the highest observed D2 channel near the oxygen group is 601, implying a 17 channel spread due to resolution. Finally, it should be noted that in this energy region, the abundance of elements with $Z > 8$ is much smaller than the abundance of CNO.

The energy spectra of oxygen, nitrogen, carbon, and helium for almost 11 months of quiet time data are shown in Figure III - 4. The lowest and highest energy oxygen points are obtained from the region in which the D2 or D5 ADC is saturated and in which clean element identification is not possible. The low energy oxygen point includes a small amount of nitrogen and $Z \geq 9$, and the high energy point includes a small amount of nitrogen and $Z = 9 - 12$. However, because of the smaller energy intervals and the lower fluxes,

FIGURE III - 4

IMP-8 oxygen, nitrogen, carbon, and helium quiet time spectra from October 31, 1973 - September 25, 1974.

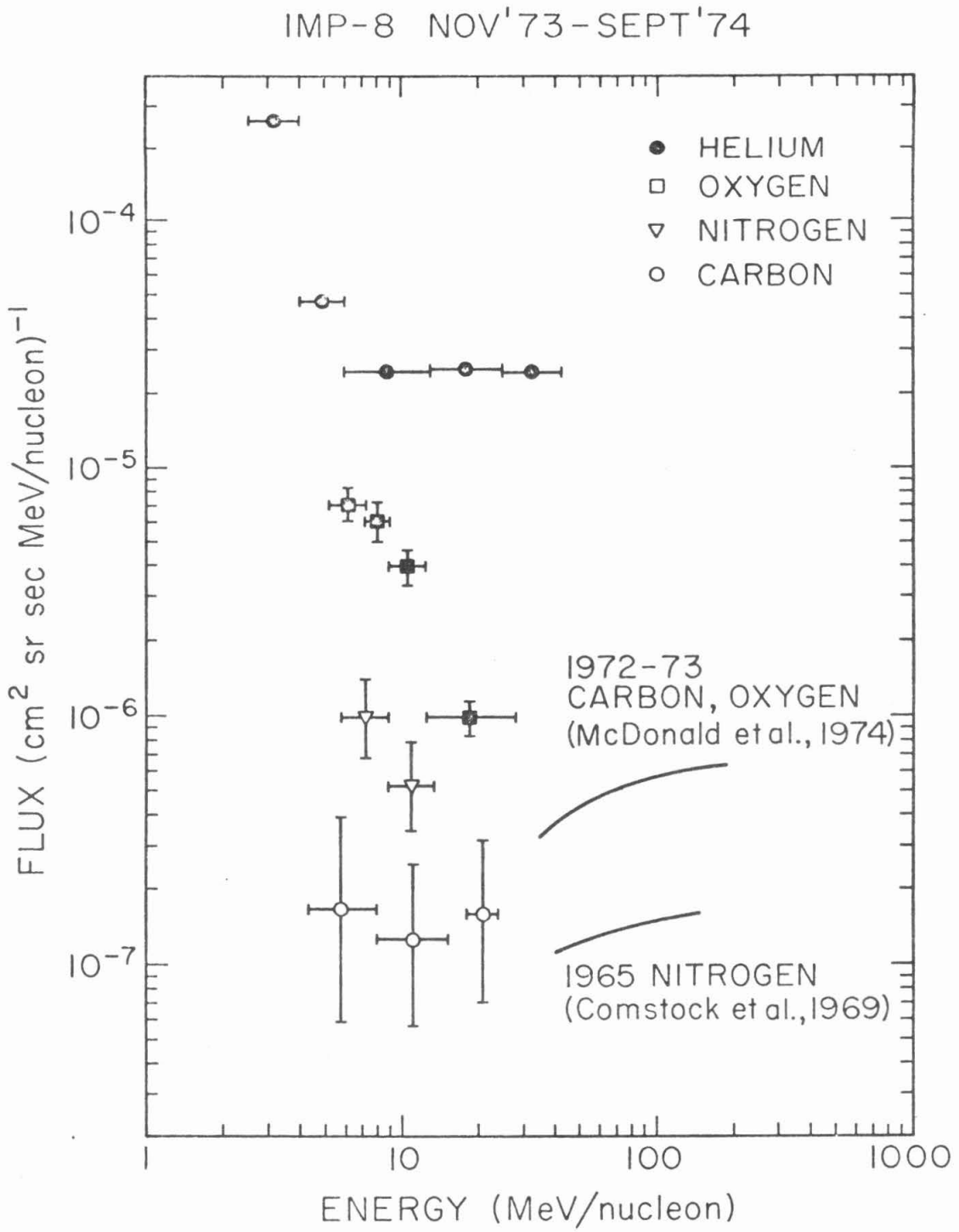
IMP-8 NOV'73-SEPT'74
HELIUM
OXYGEN
NITROGEN
CARBON
1972-73
CARBON, OXYGEN
(McDonald et al., 1974)
1965 NITROGEN
(Comstock et al., 1969)
FLUX (cm² sr sec MeV/nucleon)⁻¹
ENERGY (MeV/nucleon)
10⁻⁴
10⁻⁵
10⁻⁶
10⁻⁷
1
10
100
1000

the amount of contamination is smaller than the uncertainties due to statistics. Therefore, no attempt has been made to subtract out these contributions. The highest energy carbon point is obtained from the region in which the D5 ADC is saturated. However, in this energy region (corresponding to D2 channel = 188 - 233) only carbon is expected. Therefore, the contamination should be minimal. To extend the helium spectrum to higher energies, the 2 highest energy helium points were taken from particles that triggered D0 and at least one other detector. Except for the highest energy carbon point and the lowest and highest energy oxygen points, neither ADC is saturated for any of the other data points.

There are striking differences between the spectra for the several elements. While the helium spectrum remains flat, the oxygen and nitrogen fluxes increase rapidly as the energy decreases below 30 MeV/nucleon. The oxygen to helium ratio increases from 0.02 at ~ 1 GeV/nucleon (Webber et al., 1972; Webber and Lezniak, 1974) to ~ 0.2 at 6 - 10 MeV/nucleon. Similarly, the nitrogen spectrum increases at energies below 30 MeV/nucleon. However, the carbon, which is approximately as abundant as oxygen at high energies (Webber et al., 1972), does not increase from 30 MeV/nucleon down to 4 MeV/nucleon. This anomalous enhancement of low energy nitrogen and oxygen relative to carbon and helium is consistent with observations of other experimenters (Hovestadt et al., 1973; McDonald et al., 1974).

The large helium fluxes below 6 MeV/nucleon are probably of solar origin. By using stricter criteria for quiet time helium, the helium flux below 6 MeV/nucleon is reduced considerably.

For completeness, the quiet time fluxes have also been calculated for lithium, beryllium and boron although the statistics are not as good as for the more abundant elements. The spectra are shown in Figure III-5. The low energy beryllium and boron data points are from IMP-8 D25 events. Since there is background in the vicinity of beryllium on the IMP-8 ΔE-E' plot (see Figure III-2), only an upper limit to the low energy beryllium flux can be obtained at this stage of analysis. The low energy lithium point was obtained from the IMP-7 D25 data since the IMP-7 lithium response (see Section III-C) is cleaner than the IMP-8 response. To extend the spectra to higher energies, the high energy lithium, beryllium, and boron points were obtained from events that triggered the detector combinations D256 or D2567 on the IMP-8 telescope.

FIGURE III - 5

Lithium, beryllium, and boron
quiet time spectra from
October 31, 1973 - September 25, 1974.

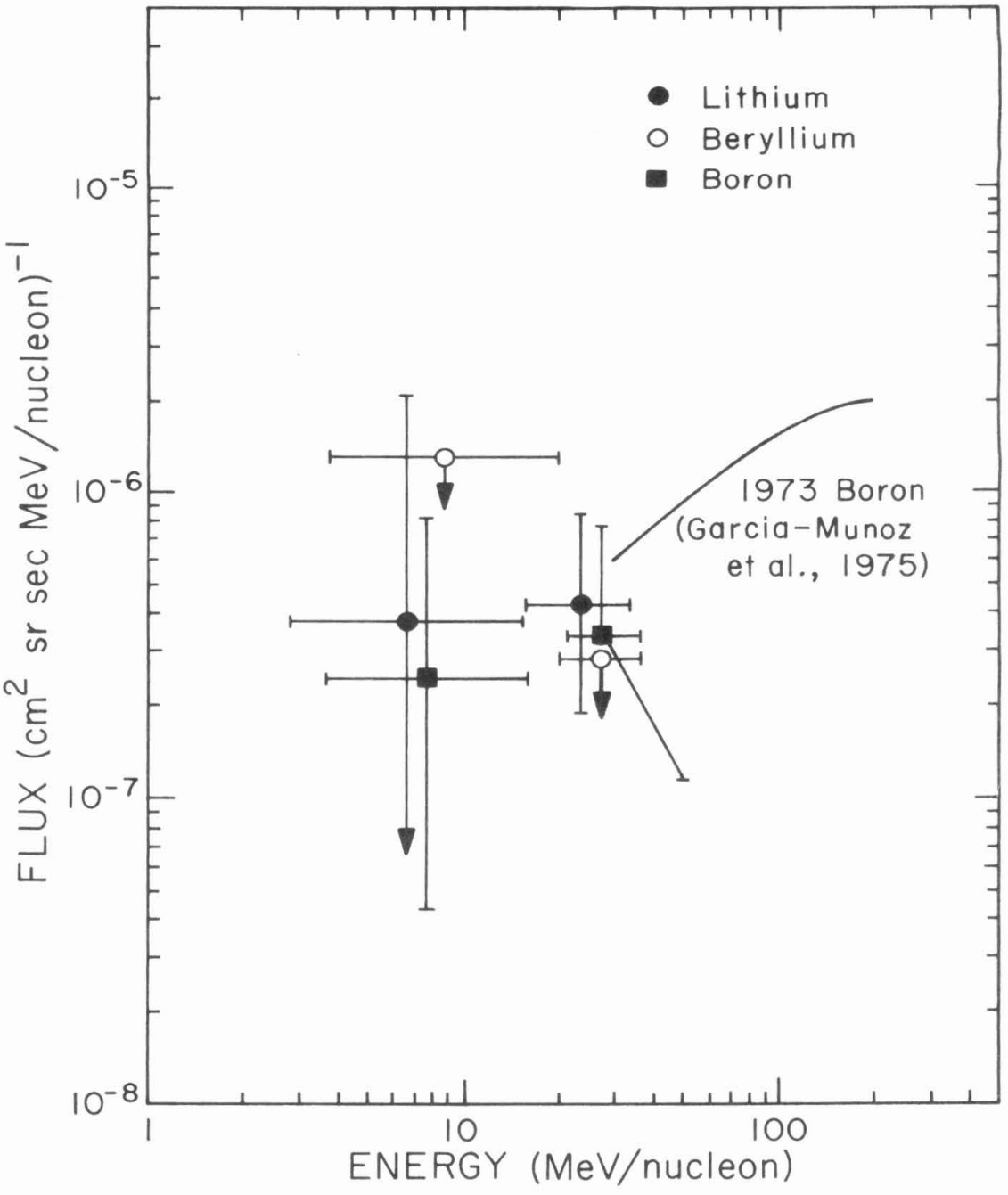
Lithium
Beryllium
Boron
1973 Boron
(Garcia-Munoz
et al., 1975)
FLUX (cm² sr sec MeV/nucleon)⁻¹
10⁻⁵
10⁻⁶
10⁻⁷
10⁻⁸
1
10
100
ENERGY (MeV/nucleon)

The low energy boron flux shows no evidence of an enhancement similar to the nitrogen and oxygen fluxes. Although the statistics are poor, the low energy lithium and beryllium fluxes are also consistent with not being enhanced.

C. Element Abundances

A plot of ΔE vs residual energy for all the IMP-7 D25 data with $Z > 2$ from September 30, 1972 to October 22, 1974 is shown in Figure III-6*. For clarity, the events along the border that saturate either the D2 or D5 ADC have been omitted, but no background has been subtracted from the plot. Note that the events represented by the open circles are not necessarily of solar origin; they just do not fit our criteria for quiet time events. The D2 thickness used to calculate the isotope tracks was obtained by fitting proton and alpha particle flight data to masses of 1.007 and 4.002 amu.

It is apparent that the signal to noise is extremely good for $Z > 3$. However, below $Z = 3$ there is a distribution of background events which extend almost up through lithium. All the data shown below lithium are more than 2 standard deviations (based on

---

*18 days of data during which D4 was disabled have been omitted. During this period particles can pass through D4 without being detected and then deposit the remaining energy in D5. The total energy is therefore not observed.

FIGURE III - 6

IMP-7 D25 data from September 30, 1972 - October 22, 1974. Solid circles represent data obtained during solar quiet periods (PHI $\leq 10^{-3}$/sec), and open circles represent data obtained during solar active periods (PHI $> 10^{-3}$/sec). No data below the broken line were included in the plot. The solid lines for the isotope tracks are based on calibration data, while the dashed lines are calculated using standard range - energy tables. The dashed lines are adequate for element identification but should not be used for isotope identification. The dotted lines of constant energy indicate the energies for which the element abundances of Table III - 3 were determined.

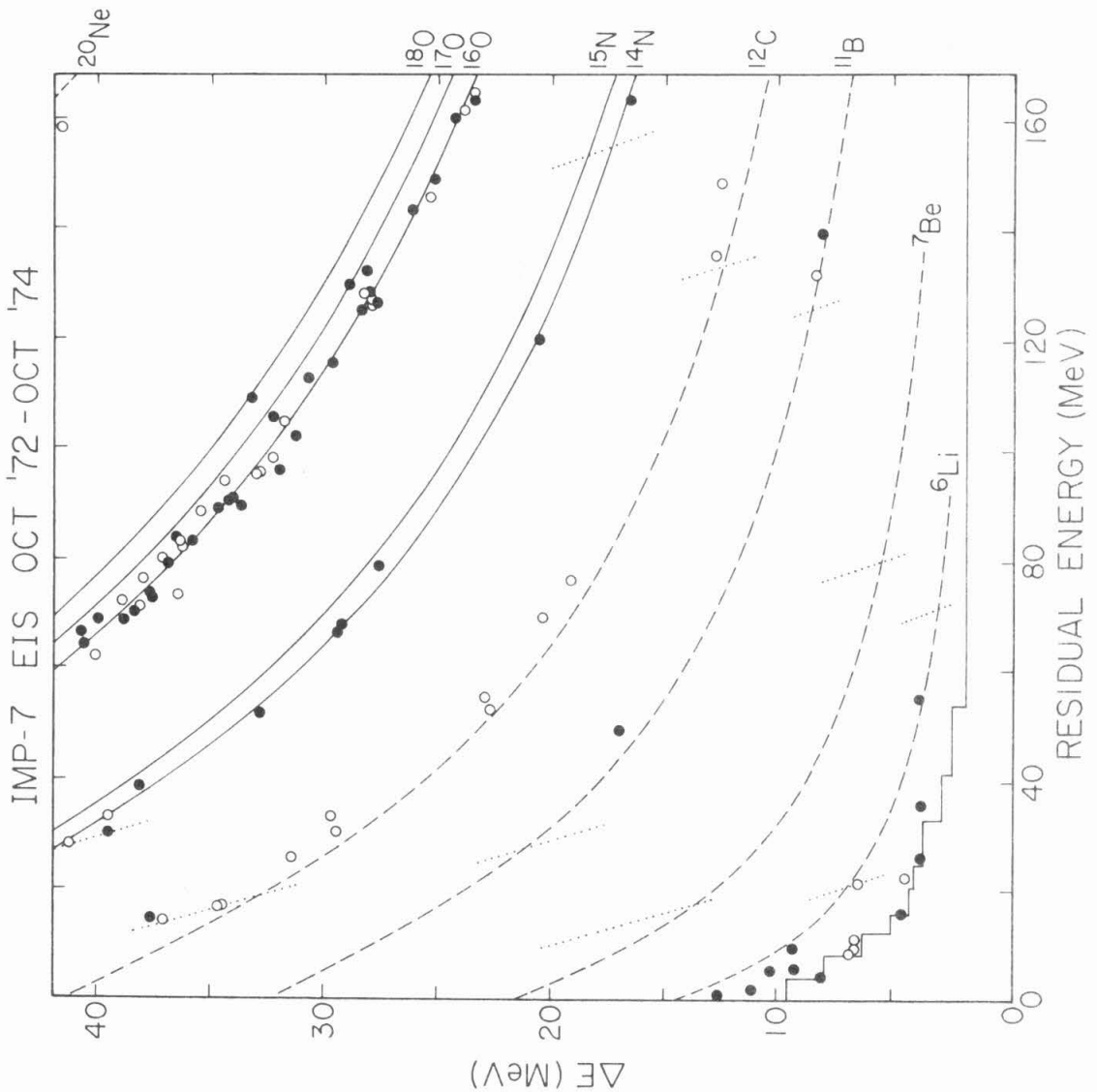
IMP-7 EIS OCT '72-OCT '74
ΔE (MeV)
RESIDUAL ENERGY (MeV)
0
10
20
30
40
0
40
80
120
160
^{20}Ne
^{18}O
^{17}O
^{16}O
^{15}N
^{14}N
^{12}C
^{11}B
^{7}Be
^{6}Li

the calculated mass resolution) from ^{6}Li. In addition, there is one event which is consistent with ^{6}Li. This event also has a larger D5 (residual energy in Figure III-6) pulse height than the background events below lithium, and it may therefore be beyond the background region. However, at this stage of analysis, we cannot be certain that the event is not an extension of the background, and we can only say that there is at most one lithium event in Figure III-6.

To extend the oxygen abundances to lower energies, data were used from the region in which the D2 ADC is saturated. A plot of the IMP-7 quiet time data that saturate the D2 ADC is shown in Figure III-7. It is clear from the plot that contamination due to particles heavier than oxygen is minimal.

The clean instrument response of the IMP-7 EIS allows us to calculate the elemental abundances in a straightforward manner. However, because of instrumentation limits discussed in Appendix B, we have restricted the upper energy limit for the IMP-7 instrument to values below saturation of the D5 ADC. Elemental abundances can also be obtained from the IMP-8 EIS data presented in Section III-B.

The abundances of selected elements relative to oxygen are given in Table III-3. For comparison, the ratios obtained by McDonald et al. (1974) and the ratios at energies above 1 GeV/nucleon (Webber, 1972) are also shown. The 5 - 12.5 MeV/nucleon energy interval corresponds to the energies at which oxygen enters D5 and at which it saturates the D5 ADC (see Tables II-5 and II-8). The

FIGURE III - 7

IMP-7 quiet time data from September 30, 1972 - October 22, 1974 for events that saturate the D2 ADC. The channels for which elements can saturate the D2 ADC are also indicated on the plot. (Compare with Table II - 5.)

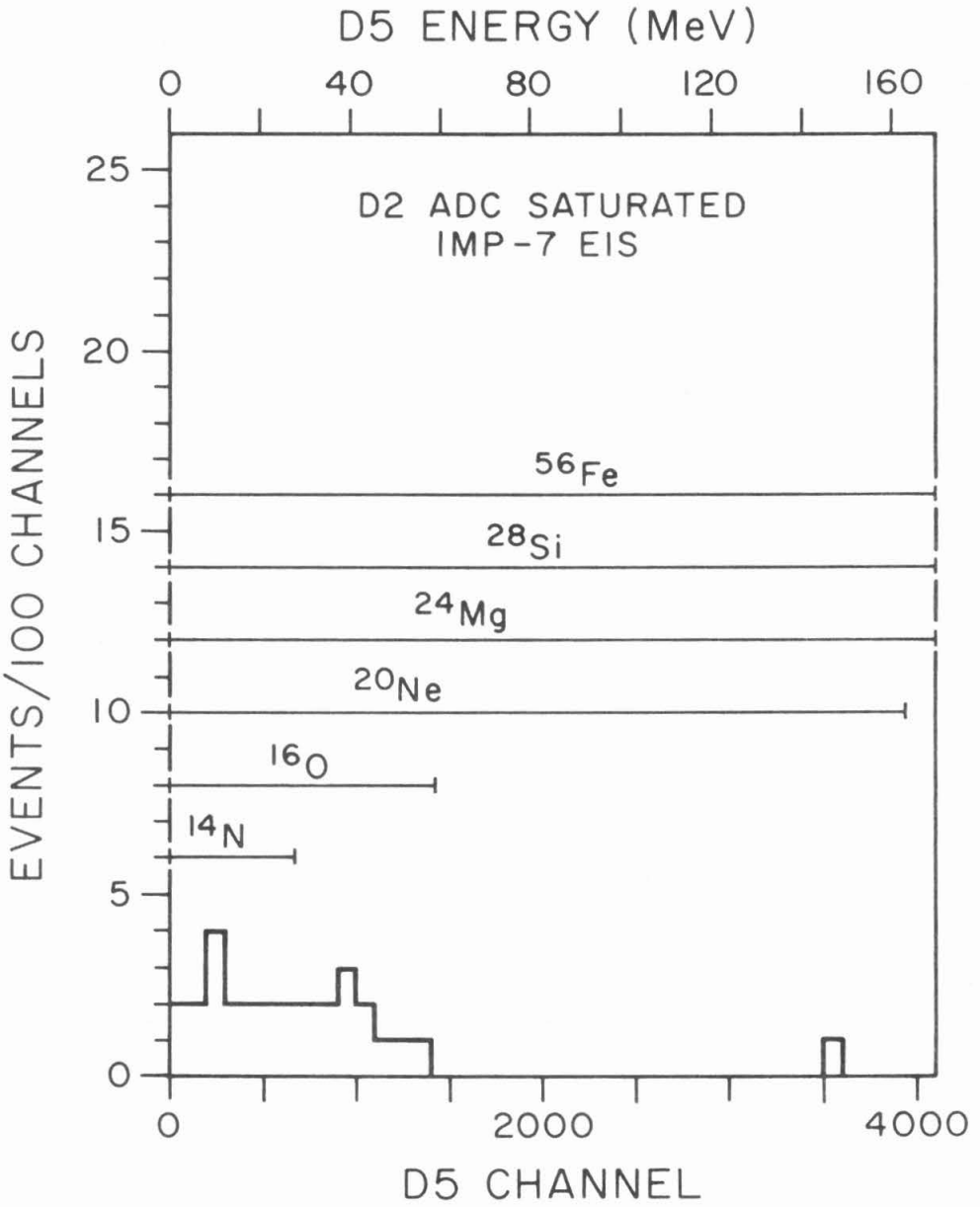
D5 ENERGY (MeV)
0
40
80
120
160
D2 ADC SATURATED
IMP-7 EIS
56Fe
28Si
24Mg
20Ne
16O
14N
EVENTS/100 CHANNELS
25
20
15
10
5
0
0
2000
4000
D5 CHANNEL

TABLE III - 3

Elemental Abundances During Solar Quiet Periods

Element	Energy (MeV/nucleon)	IMP-7[++] (Oct '72-Oct '74) #	Ratio	IMP-8 (Nov '73-Sept '74) #	Ratio	MTTW* (Mar '72-Mar '73)	>1 GeV/nucleon[+]
He/O	6-13	278/62[++]	$4.5 \pm .7$[++]	564/114	$4.9 \pm .5$		36 ± 1[‡]
	7.3-10.6					$2.4 \pm .3$	
	7.3-30					11.0 ± 1.0	
Li/O	5-12.5	≤1/58	$0.017^{+.040}_{-.017}$				0.172 ± .004
Be/O	5-12.5	0/58	≤0.032	≤1/128	≤0.026		0.101 ± .003
B/O	5-12.5	1/58	$0.017^{+.040}_{-.014}$	1/128	$0.008^{+.018}_{-.007}$		0.308 ± .005
	8.3-30					0.031 ± .016	
C/O	5-12.3	1/58	$0.017^{+.040}_{-.014}$	4/128	$0.031^{+.025}_{-.015}$		1.125 ± .011
	9.0-30					0.087 ± .029	
N/O	5.7-12.5	7/46	$0.152^{+.082}_{-.056}$	17/114	$0.149 \pm .039$		0.290 ± .005
	7.3-10.6					0.211 ± .065	
Ne/O	7.2-11.1	≤1/25	≤0.132				0.174 ± .005
	17.2-17.0			≤4/60	≤0.120		
	12-30					0.071 ± .032	
Mg/O	7.7-10.5	≤1/17	≤0.194				0.205 ± .005
	10.7-17.0			≤3/69	≤0.086		
	13.4-30					<0.036	
Si/O	8.1-10.2	≤1/13	≤0.253				0.137 ± .004
	10.5-28.3			≤5/74	≤0.113		
	14.5-30					<0.042	
Fe/O	11.5-28.3			≤3/63	≤0.094		0.110 ± .004

[++] He/O ratio corrected for cross-talk (see Appendix B).

* MTTW = McDonald, Teegarden, Trainor, and Webber (1974). The numbers in this column are calculated from their tabulated element abundances relative to helium and from their oxygen and helium fluxes, which are given in the form of a graph.

[+] From Webber (1972).

[‡] From MTTW.

energy intervals used for the elements Z = 3 - 7 are indicated in Figures III-2 and III-6. Note that since there is background in the vicinity of beryllium on the IMP-8 ΔE - E' plot, the single beryllium event is to be taken as an upper limit. Particles with $Z \geq 10$ saturate the D2 or D5 ADC over most of the energy range. (See Figure III-2.) Since unambiguous element identification is not possible, upper limits to the abundances are obtained by assuming, in turn, that all particles are neon, magnesium, silicon, and iron.

The element abundances from IMP-7 and IMP-8 are in good agreement. The results of the present work are also consistent with the results of McDonald et al. (1974). Their B/O and C/O ratios are somewhat higher than ours, but their ratios extend to higher energies, where the oxygen flux is lower.

Comparing the low energy ratios with the high energy ratios of Webber (1972), it can be seen that,except for nitrogen, none of the elements listed in Table III-3 exhibit the same dramatic enhancement at low energies as oxygen. McDonald et al. (1974) had previously noted that there were no enhancements in the boron and carbon fluxes at energies down to ~ 9 MeV/nucleon. We are now able

to rule out enhancements at lower energies. (Compare with Figures III-4 and III-5).

D. Isotope Abundances

Masses were calculated for each nitrogen and oxygen event in Figure III-6. A mass histogram for the IMP-7 quiet time oxygen data is shown in Figure III-8. The Gaussian curve centered at mass sixteen indicates the expected mass response to ^{16}O. The 0.42 amu 1σ width of the curve was obtained from the predicted mass resolution (see Table II-9), and the height was normalized to the total number of events in the histogram. Except for the single event near mass 18, the data are consistent with a pure ^{16}O composition and no admixture of ^{17}O.

The mass histogram for the IMP-7 quiet time nitrogen data is shown in Figure III-9. The Gaussian curve with a 1σ width of 0.37 amu indicates the expected mass response to ^{14}N cosmic rays. The nitrogen data are consistent with a pure ^{14}N composition.

Excluding the oxygen event near mass 18, the observed nitrogen and oxygen mass distributions are compared in Table III-4 with the distributions expected from a pure ^{14}N and ^{16}O composition. The mean masses indicate that the nitrogen and oxygen are consistent with pure ^{14}N and ^{16}O and are inconsistent with a large fraction of ^{15}N or of ^{17}O or ^{18}O. In addition, the observed mass resolution indicates that the nitrogen and oxygen are each consistent with being composed of a single isotope.

FIGURE III - 8

Mass histogram of quiet time IMP-7 oxygen data from September 30, 1972 - October 22, 1974. The Gaussian curve centered on mass 16 indicates the predicted mass response to ^{16}O. There are 29 events in the histogram.

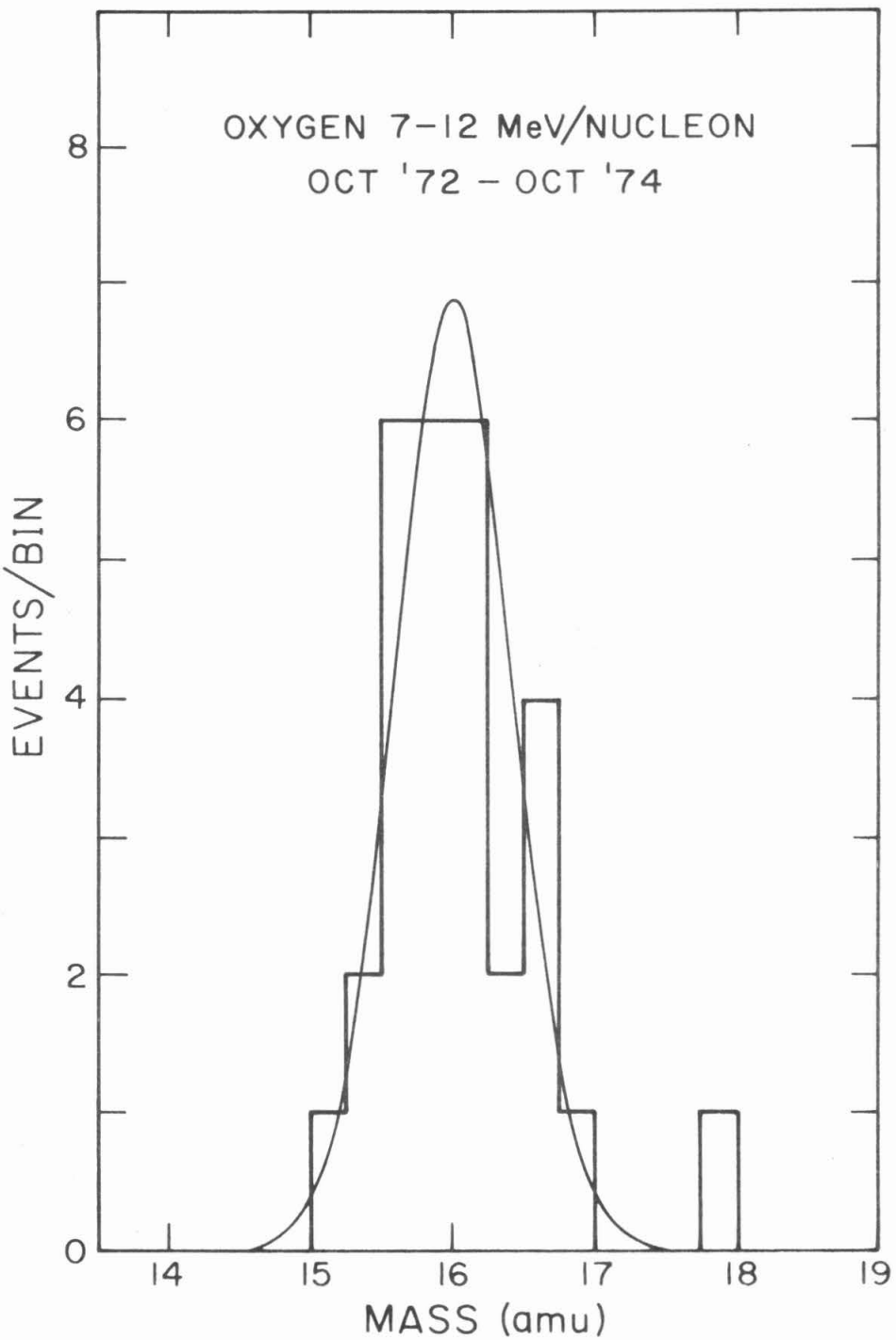
OXYGEN 7–12 MeV/NUCLEON
OCT '72 – OCT '74
EVENTS/BIN
0
2
4
6
8
14
15
16
17
18
19
MASS (amu)

FIGURE III - 9

Mass histogram of quiet time IMP-7 nitrogen data from September 30, 1972 - October 22, 1974. The Gaussian curve centered on mass 14 indicates the predicted mass response to ^{14}N. There are 8 events in the histogram.

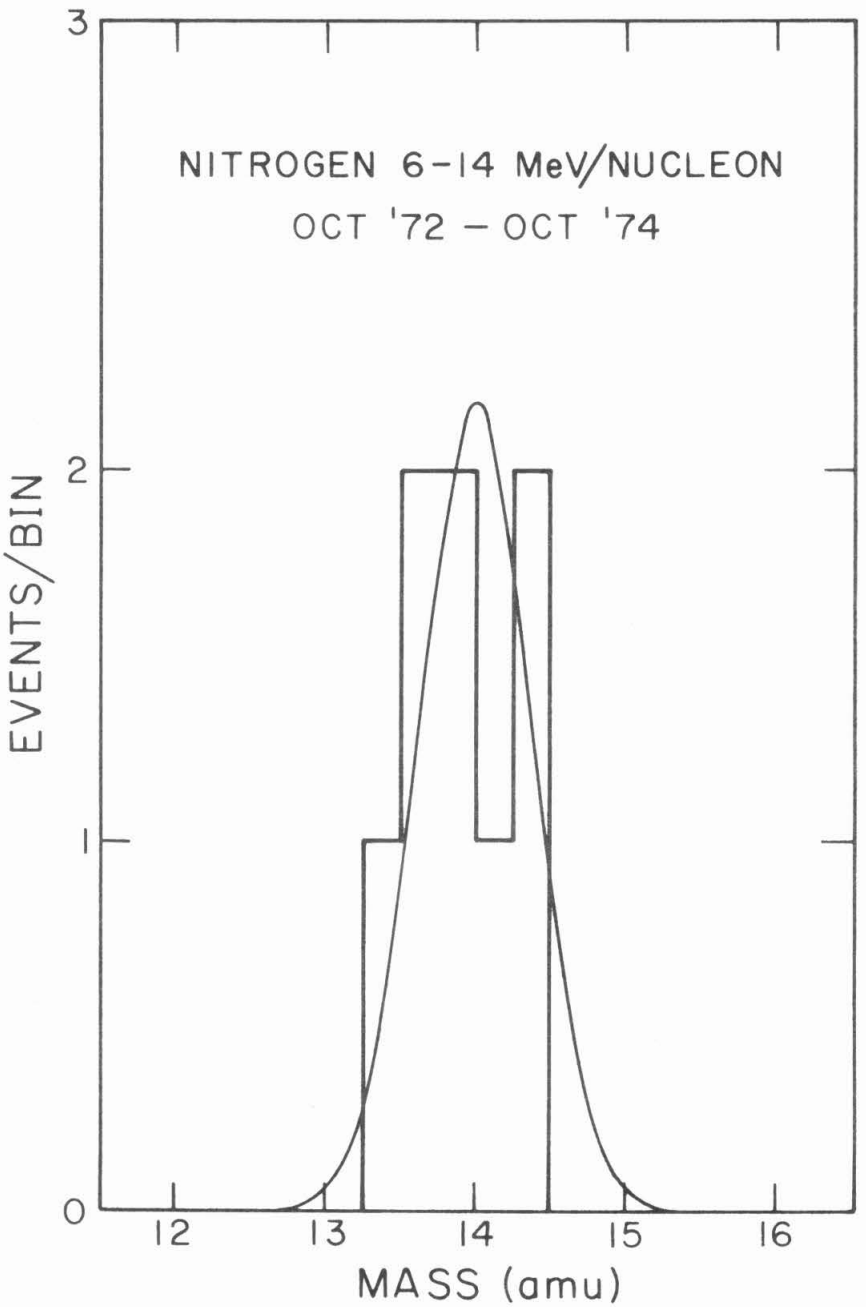
NITROGEN 6-14 MeV/NUCLEON
OCT '72 – OCT '74
EVENTS/BIN
0
1
2
3
12
13
14
15
16
MASS (amu)

TABLE III - 4

IMP-7 Nitrogen and Oxygen Mass Distributions

	OBSERVED		EXPECTED*	
	Quiet Periods	Active Periods	Quiet Periods	Active Periods
$\overline{M}_{Nitrogen}$ (amu)	13.94 ± .13	13.94 ± .08+	14.00	14.00
$\sigma_{M_{Nitrogen}}$ (amu)	0.38 ± .10	$0.12^{+.25}_{-.06}$+	0.37	0.41
$\overline{M}_{Oxygen}$ (amu)	15.98 ± .08‡	15.92 ± .10	15.99	15.99
$\sigma_{M_{Oxygen}}$ (amu)	0.43 ± .06‡	0.46 ± .07	0.42	0.42

*Assumes pure ^{14}N and ^{16}O composition. The resolution is calculated at the average energy of the observed data.

+Based on 2 events.

‡Doesn't include event near mass 18.

It is reasonable to ask whether the nitrogen and oxygen mass scales can be offset: for example,whether the dominant isotopes are ^{15}N and ^{17}O (a 1 amu offset). There are two possible contributions to the uncertainty of the mean mass: the error in predicting the mass response to nitrogen and oxygen from the observed response to hydrogen and helium and the error in the energy calibration relating the ADC channel to energy.

From the calibration at the Berkeley 88" cyclotron, the nitrogen and oxygen masses can be predicted to approximately 0.05 amu. (See Appendix C.)

The electronic calibrations indicate the high stability of the D2 and D5 gain and offset as a function of time. Table II-10 illustrates that the direct effects of the drifts in the gain and offset are unimportant for calculating the mass of oxygen. However, an uncertainty in the offset also has an indirect effect on the nitrogen and oxygen mass. The D2 thickness is obtained by fitting the proton and alpha mass peaks. An error in the D2 offset is compensated by adjusting the value of the D2 thickness. The D2 thickness, in turn, affects the nitrogen and oxygen mass. The maximum observed uncertainty in the D2 offset is 0.013 MeV (Table II-9), and the rms uncertainty is 0.003 MeV. The alpha particles which were used to determine the D2 thickness deposited an average energy of 3.7 MeV/nucleon in D25. At 3.7 MeV/nucleon, a 0.003 MeV shift

in the D2 offset gives rise to a 0.005 amu or a 0.12% shift in the helium mass. The resulting shift in the D2 thickness also causes a 0.12% shift in the other masses. Table III-5 summarizes the resulting mass uncertainties for nitrogen and oxygen.

The events obtained during solar active periods provide further evidence against a mass shift of 1 amu. The mean masses and the mass resolution of the solar active nitrogen and oxygen are consistent with the values for the quiet time data (see Table II-4). Since solar nitrogen and oxygen are expected to be predominantly ^{14}N and ^{16}O (Cameron, 1973), this indicates that the calculated masses are not shifted by 1 amu.

To calculate the relative isotopic abundances for nitrogen and oxygen, the method of maximum likelihood was used. (See, for example, Mathews and Walker, 1965). The cosmic rays of each element were assumed to be composed of 2 isotopes of relative abundance f_1 and f_2 where $f_1 + f_2 = 1$. The likelihood can then be expressed as

$$L(f_1, f_2) = \prod_i \left[\frac{f_1}{\sqrt{2\pi}\ \sigma_1} e^{-\frac{1}{2}\frac{(M_1 - M_i)^2}{\sigma_1^2}} + \frac{f_2}{\sqrt{2\pi}\ \sigma_2} e^{-\frac{1}{2}\frac{(M_2 - M_i)^2}{\sigma_2^2}} \right] \qquad \text{III-2}$$

TABLE III - 5

Estimated Rms Errors in Mass

	Electronics*	Error in D2 Thickness+	Calibrated Isotope Response‡	Total
^{4}He(amu)	0.005++	0.005		
^{14}N(amu)	0.006	0.02	0.06	0.06
^{16}O(amu)	0.007	0.02	0.05	0.05

*Similar to Table II - 10 except that results here are rms errors rather than maximum errors.

+The D2 thickness error results from compensating for the error in the ^{4}He mass due to the error in the D2 offset. (See text.)

‡See Appendix C.

++Uncertainty in the D2 offset is the major contribution.

where L is the likelihood function, M_1 and M_2 are the masses of isotopes 1 and 2, σ_1 and σ_2 are the resolution of isotopes 1 and 2, and M_i are the observed masses. This is a straightforward procedure for nitrogen,which has only 2 stable isotopes: ^{14}N and ^{15}N. However, oxygen has 3 stable isotopes: ^{16}O, ^{17}O, and ^{18}O. Therefore, for oxygen the fractions of ^{17}O and ^{18}O were calculated separately. The event near mass 18 (mass = 17.84 amu) is 1.9 σ away from ^{17}O and 0.3 σ away from ^{18}O, implying a 0.85 probability that the event is ^{18}O rather than ^{17}O. Therefore, it was included in the calculation of the ^{18}O abundance but not in the calculation of the ^{17}O abundance. In all of the maximum likelihood calculations, the energy range was restricted to equal energy per nucleon intervals.

Figure III-10 illustrates the likelihood functions of the fractions ^{15}N, ^{17}O, and ^{18}O in the quiet time cosmic rays. The functions are normalized to

$$\int_0^1 L(f)\, df = 1$$

where L is the likelihood function and f is the fraction of ^{15}N, ^{17}O, or ^{18}O. From the plots it can be seen that the most likely value for the relative fraction of ^{15}N and ^{17}O is 0. For ^{18}O the most likely value for the $^{18}O/(^{16}O + {}^{18}O)$ abundance is 0.04.

The integral of the likelihood function between the limits f_1 and f_2 gives the probability that the fraction f lies between

FIGURE III - 10

Likelihood functions for the fractions of ^{15}N, ^{17}O, and ^{18}O in the low energy cosmic rays. The area under each curve is 1.

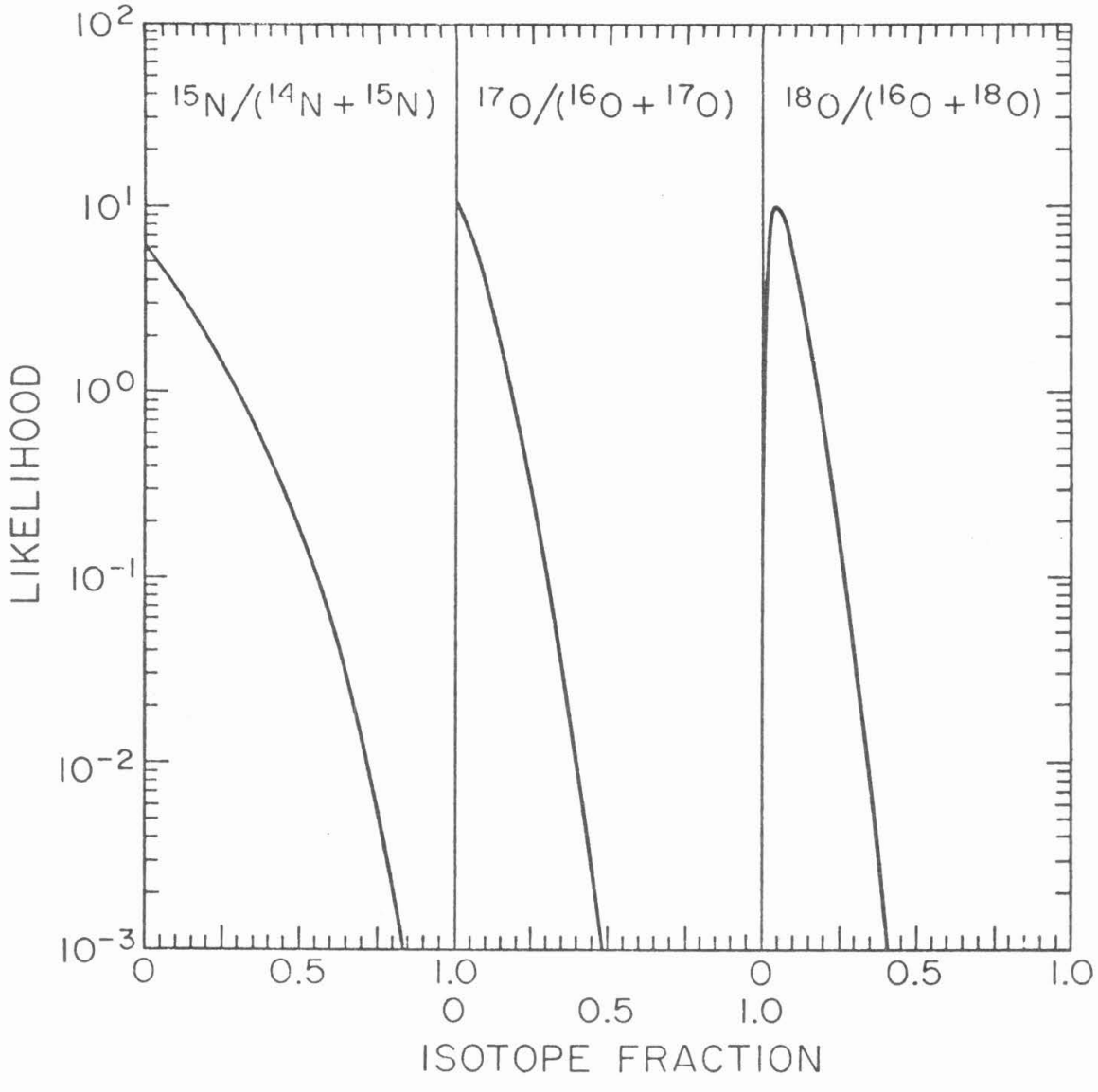
10^2
10^1
10^0
10^{-1}
10^{-2}
10^{-3}
LIKELIHOOD
$^{15}N/(^{14}N + ^{15}N)$
$^{17}O/(^{16}O + ^{17}O)$
$^{18}O/(^{16}O + ^{18}O)$
0
0.5
1.0
0
0.5
1.0
0
0.5
1.0
ISOTOPE FRACTION

f_1 and f_2. The upper limit f_u on the fraction f is obtained by integrating from 0 to f_u such that the integral equals 0.84 and 0.95 for the 84% and 95% confidence intervals respectively. The most probable value of f is taken to be at the peak of the likelihood function. The relative abundances of the isotopes of nitrogen and oxygen obtained by this technique are given in Table III-6.

The 0.04 $^{18}O/O$ ratio of Table III-6 is the result of a formal calculation of the maximum likelihood based on a single ^{18}O event. If the event were due to background or to some other unidentified instrument problem, then the best estimate of the $^{18}O/O$ ratio would be 0. We have looked at other possibilities* and could not find a reasonable alternative to the hypothesis that the event is ^{18}O (except the 0.15 probability that it is ^{17}O, which would also be interesting). However, since we cannot have full confidence in only a single event we are setting a lower limit of 0 on the $^{18}O/O$ ratio.

---

*Since the event is 4.4 σ away from ^{16}O and only 0.3 σ away from ^{18}O, a Gaussian response implies that for 29 oxygen events, there is a $29 \times 6 \times 10^{-5} = 2 \times 10^{-3}$ probability that the event is ^{16}O rather than ^{18}O. Background in the vicinity of ^{18}O is also expected to be minimal. Figure II-4 illustrates that from calibration data, only 1 event was near mass 18 out of a total of 20,000 ^{16}O events.

TABLE III - 6

Isotopic Composition of the Low Energy Nitrogen and Oxygen Cosmic Rays

Isotope Ratio	MeV/nucleon	84% Confidence Interval	95% Confidence Interval
$^{15}N/N$	5.6 - 12.7	≤ 0.26	≤ 0.39
$^{17}O/O$	7.0 - 11.8	≤ 0.13	≤ 0.18
$^{18}O/O$	7.0 - 11.2	$0.04^{+.08}_{-.04}$	≤ 0.17

The calculated upper limits for the ^{15}N, ^{17}O and ^{18}O isotopic abundances are not sensitive to the assumed mass resolution. However, they do depend somewhat on any offset in the mass scale. If the calculated masses are all increased by 0.05 amu (see Table II -5), then the 84% and 95% confidence intervals of Table III-6 are increased by approximately 0.03 for the ^{15}N and ^{17}O fraction, and the ^{18}O fraction is increased by 0.01. Similarly, if the masses are all decreased by 0.05 amu, then the confidence intervals are also decreased.

IV. DISCUSSION OF RESULTS - POSSIBLE SOURCES

A. Introduction

The energy spectra of the cosmic rays indicate that the enchanced low energy nitrogen and oxygen may not be part of the same population as the higher energy cosmic rays. The isotopic composition of the cosmic rays provide additional evidence that the low energy nitrogen is not part of the same population as the higher energy nitrogen. In the region of enhancement, the nitrogen is predominantly ^{14}N. This contrasts with measurements at higher energies of ~ 50 - 250 MeV/nucleon which indicate that at least 1/2 the nitrogen is ^{15}N (Webber et al., 1973; Garcia-Munoz et al., 1974).

The large ^{15}N composition at higher energies is due to spallation of the heavier cosmic rays as they pass through 6 - 10 g/cm^2 (Brown, 1973) of interstellar material. Since the nitrogen in the low energy region is primarily ^{14}N, this indicates that the low energy nitrogen is not part of a higher energy population which has passed through several g/cm^2 of material and has been decelerated by the solar wind.

The enhanced nitrogen and oxygen fluxes can be interpreted as a separate low energy nitrogen and oxygen component superimposed on the decelerated component. Several possible origins have been considered in the literature for the low energy nitrogen and oxygen cosmic rays. Two possibilities are that the particles are of

galactic origin (McDonald et al., 1974) or that they are accelerated locally in the heliosphere (Fisk et al., 1974). A variation of the second possibility is that the particles are accelerated on the sun.

B. Solar Origin

As pointed out by McDonald et al. (1974), a solar origin for these particles is unlikely for several reasons. First, the charge composition in the 10 MeV/nucleon region is unlike the composition of typical solar cosmic rays. Table IV - 1 compares the elemental abundances in the quiet time cosmic rays at about 10 MeV/nucleon with typical abundances of the cosmic rays in solar flares and with spectroscopically determined abundances in the solar photosphere and corona. A striking example of the differences in composition is that the carbon abundance in the quiet time cosmic rays at these energies is only ~ 3% of the oxygen abundance, while in the solar cosmic rays and in the solar photosphere and corona the carbon is at least 1/3 as abundant as the oxygen.

The oxygen flux from 8 - 30 MeV/nucleon exhibits a positive radial gradient (McDonald et al., 1974). This also argues against a solar origin for the low energy oxygen.

The spectra are unlike the typical steep spectra observed during solar flares. Figure IV - 1 illustrates the oxygen spectrum from 0.3 - 28 MeV/nucleon. Although the steep portion of the spectrum below 1 MeV/nucleon may be of solar origin (Hovestadt et al., 1973), it is unlikely that the higher energy part of the spectrum is also of solar origin.

TABLE IV - 1

Comparison of Low Energy Cosmic Ray Composition with Selected Solar Abundances

Ratio	Energy* (MeV/nucleon)	Present Work	Solar Flare+	Solar Photosphere‡	Solar Corona++
He/O	6 - 13	$4.9 \pm .5$	42.0 ± 2.5		4.4×10^{2}
Li/O	5 - 12.5	$0.017^{+.040}_{-.017}$	< 0.003	9.9×10^{-9}	
Be/O	5 - 12.5	≤ 0.026	< 0.003	2.5×10^{-7}	
B/O	5 - 12.5	$0.008^{+.018}_{-.007}$	< 0.008		
C/O	5 - 12.5	$0.031^{+.025}_{-.015}$	$0.49 \pm .03$	0.58	1.3
N/O	5.7 - 12.5	$0.149 \pm .039$	$0.116 \pm .011$	0.10	0.13

*Energy interval refers to present work

+September 1, 1971 flare from Teegarden et al. (1973)

‡From Goldberg et al. (1960)

++From Pottasch (1974)

FIGURE IV - 1

Low energy quiet time oxygen spectrum

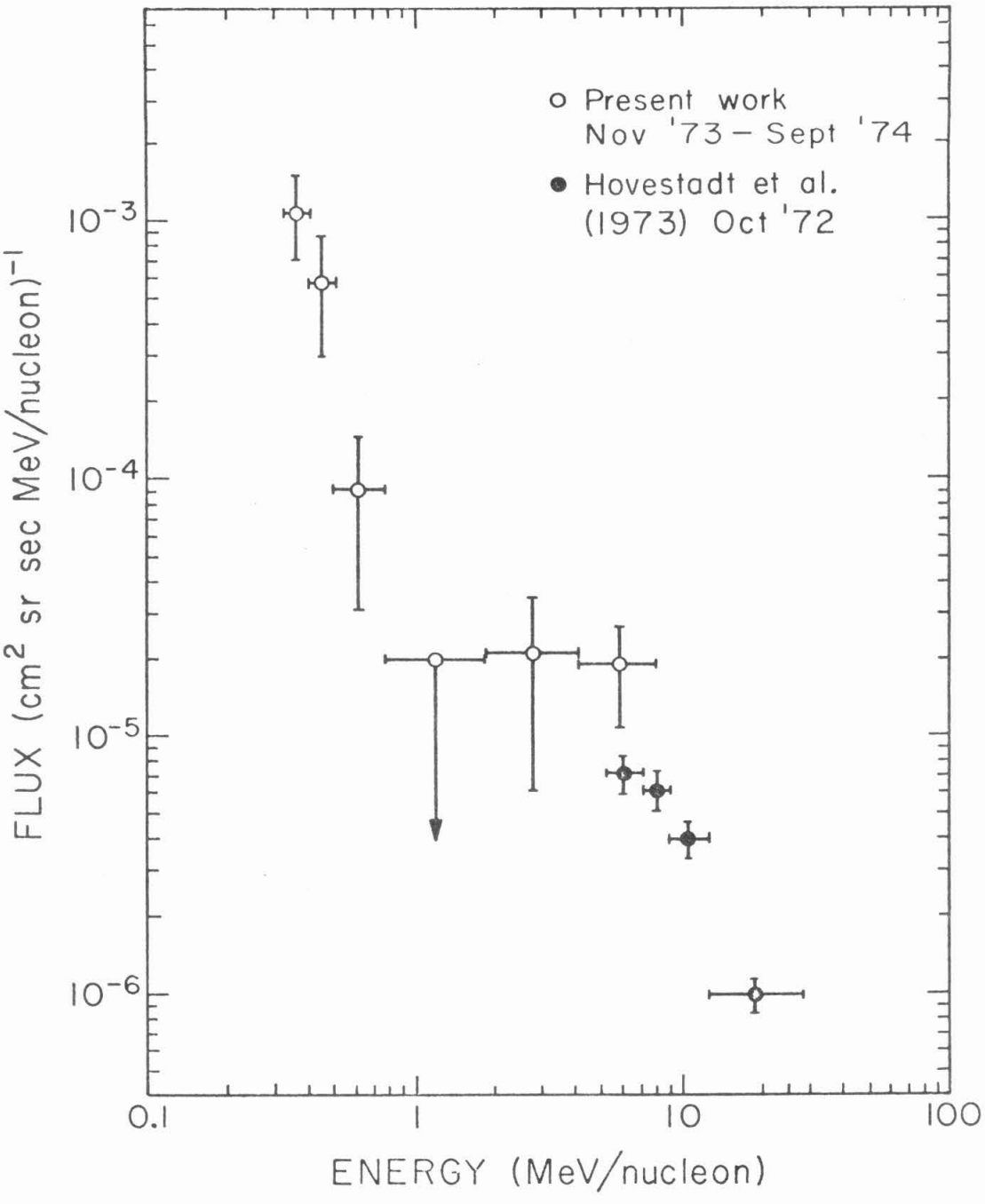
o Present work
Nov '73 – Sept '74
● Hovestadt et al.
(1973) Oct '72
FLUX (cm² sr sec MeV/nucleon)⁻¹
10⁻³
10⁻⁴
10⁻⁵
10⁻⁶
0.1
1
10
100
ENERGY (MeV/nucleon)

The time variations of the nitrogen plus oxygen nucleii indicate that these particles are modulated in a manner similar to the higher energy galactic cosmic rays (Mewaldt et al., 1974a). Since the intensity of galactic cosmic rays observed near earth is inversely related to solar activity, these variations are another indication that the low energy nitrogen and oxygen are not solar in origin.

The bulk of the evidence argues against a solar origin for the enhanced nitrogen and oxygen fluxes at low energies. Therefore, we shall not further discuss the solar origin theory.

C. Galactic Source

The possibility that these particles originate from an extra-solar source in the galaxy has been suggested previously (McDonald et al., 1974). In the context of present modulation theory, it is difficult to account for the enhanced nitrogen and oxygen fluxes that are observed near the earth (Fisk, 1974) if these particles are totally ionized. Modulation theory predicts that an enormously large flux of nitrogen and oxygen would have to exist in the interstellar medium (Fisk, 1974) to produce the fluxes observed near earth. Such large fluxes would produce much more ionization of the interstellar medium than is actually observed (Hughes et al., 1973). One way around this problem is to alter modulation theory. Fisk (1974) has suggested a modification which results in less modulation. Another approach is to have a nearby source of singly ionized particles. Since singly ionized particles have a much higher

rigidity than fully ionized particles at identical velocities, the modulation of the singly ionized particles is much less severe.

Whatever the solution to the difficulty of getting the enhanced nitrogen and oxygen fluxes to the earth from outside the heliosphere, any proposed nucleosynthesis source for these particles should also be able to explain the observed isotopic abundances. For example, Hoyle and Clayton (1974), in the course of investigating nucleosynthesis in white dwarfs, proposed that perhaps these white dwarfs could be the source of the low energy nitrogen and oxygen cosmic rays. In their model they expected the nitrogen and oxygen to be considerably in excess over carbon. They also expected ^{15}N and ^{17}O to be overabundant and, depending on initial conditions, perhaps even the dominant nitrogen and oxygen isotopes. The present isotopic measurements of the low energy cosmic rays rule out as a source a nucleosynthesis process in which ^{15}N and ^{17}O are more abundant than ^{14}N and ^{16}O.

D. Local Source

Fisk et al. (1974) proposed that the enhanced nitrogen and oxygen cosmic rays may be the result of an acceleration mechanism within the solar system that acts on the interstellar gas. Since the first ionization potentials of nitrogen and oxygen are larger than for hydrogen, a large fraction of the nitrogen and oxygen in the interstellar gas exists in the neutral state (Rogerson et al., 1973). This contrasts with the interstellar carbon, which exists primarily in the singly ionized state. As neutral particles,

the nitrogen and oxygen can penetrate the solar cavity, while the ionized carbon is excluded. When these neutral particles pass close enough to the sun, they can be ionized by ultraviolet light or by the solar wind (Axford, 1971). Once ionized, these particles have a higher rigidity in the rest frame of the solar wind than typical thermal solar wind particles. An acceleration mechanism is then postulated that selectively accelerates these relatively high rigidity particles to several MeV/nucleon.

If there is no preferential acceleration of one isotope over another, this theory predicts that the isotopic composition of the enhanced nitrogen and oxygen cosmic rays should be identical to the isotopic composition of the interstellar medium. Table IV - 2 compares the observed isotopic composition in the low energy cosmic rays with the isotopic composition of the interstellar medium. The isotopic composition of the low energy cosmic rays is consistent with the local acceleration theory in the respect that ^{14}N and ^{16}O are the dominant isotopes. Should the $^{18}O/O$ ratio of 0.04 be indicative of the abundances in the low energy cosmic rays, then a mechanism would be needed to enhance the cosmic ray ^{18}O abundance by a factor of 20 over the abundance in the interstellar medium for the theory of Fisk et al. (1974) to remain viable.

TABLE IV - 2

Low Energy Cosmic Ray and Interstellar Medium Abundances

Ratio	Low Energy Cosmic Rays	Interstellar Medium *
$^{15}N/N$	≤ 0.26	3.7×10^{-3}
$^{17}O/O$	≤ 0.13	3.7×10^{-4}
$^{18}O/O$	$0.04 \begin{smallmatrix} + .08 \\ - .04 \end{smallmatrix}$	2.0×10^{-3}

*Cameron (1973). Cameron's abundances were intended to apply to primitive solar matter. This table assumes that they apply equally well to the interstellar gas.

V. SUMMARY AND CONCLUSIONS

The Caltech Electron/Isotope Spectrometer has been used to obtain the first definitive measurements of the isotopic composition of the quiet time nitrogen and oxygen cosmic rays in the region of enhancement. We have also extended the energy range of previous measurements of the elemental composition of the low energy cosmic rays.

In order to accurately identify the nitrogen and oxygen isotopes, we calibrated a spare telescope with a variety of isotopes of $1 \leq Z \leq 9$. Using Janni's (1966) range - energy tables for protons in silicon as a basis, we calculated corrections to be applied (after scaling the tables by $\frac{M}{Z^2}$) for helium, nitrogen, and oxygen.

An enhancement, similar to that reported by other groups (Hovestadt et al., 1973; McDonald et al., 1974; Chan and Price, 1974), was observed in the low energy nitrogen and oxygen spectra. The dominant isotopes are ^{14}N and ^{16}O. To the 84% confidence level the upper limits on the $^{15}N/N$, $^{17}O/O$, and $^{18}O/O$ abundances are, respectively, 0.26 (5.6 - 12.7 MeV/nucleon), 0.13 (7.0 - 11.8 MeV/nucleon), and 0.12 (7.0 - 11.2 MeV/nucleon).

The nitrogen isotopic composition in the region of enhancement differs from the isotopic composition reported at higher energies. This indicates that the low energy nitrogen is not from the same population as the higher energy nitrogen. The enhancement

in the low energy nitrogen and oxygen relative to the carbon can be interpreted as a separate low energy nitrogen and oxygen component superimposed on the component decelerated from higher energies.

The dominance of ^{14}N and ^{16}O in the low energy nitrogen and oxygen cosmic rays is consistent with the theory of Fisk et al. (1974) in which neutral interstellar particles enter the solar system, are singly ionized, and are then accelerated. If, on the other hand, the particles are of galactic origin, then any proposed nucleosynthesis source must produce an isotopic composition consistent with our measurements.

APPENDIX A

DATA ANALYSIS

The data processing routines relevant to this thesis will be described briefly. The purpose of this appendix is not to discuss in any depth the computer programs or the day to day data processing, but rather to outline the general procedure. More detailed information can be found in several reports on the subject (Garrard and Hurford, 1973; Garrard, 1974b; Garrard, 1974c; Garrard and Petruncola, 1974; Hurford, 1974; Marshall, 1974).

The flow diagram in Figure A - 1 schematically illustrates the method used to analyze the IMP-7 and IMP-8 flight data for this thesis. Briefly, the data are received in the form of experiment tapes. The experiment tapes are routinely reformatted into abstract tapes for convenience in future analysis. From the abstract tapes the events of interest and the time averaged rates are obtained and recorded on a strip tape. For this thesis the events of interest are those that trigger D2 and D5 only, and the time interval over which rates are averaged is one day. The preceeding data analysis is done with a PDP-11/20 computer.

A program called HARVEST is used to analyze the strip tape on Caltech's IBM-370/158 computer. In addition to a listing of the rate data and an event plot of the D2 channel vs. the D5 channel, punched cards are obtained listing the number of events at each D2, D5 coordinate pair. The punched output from HARVEST is then

FIGURE A - 1

Flow diagram illustrating
processing sequence of
flight data.

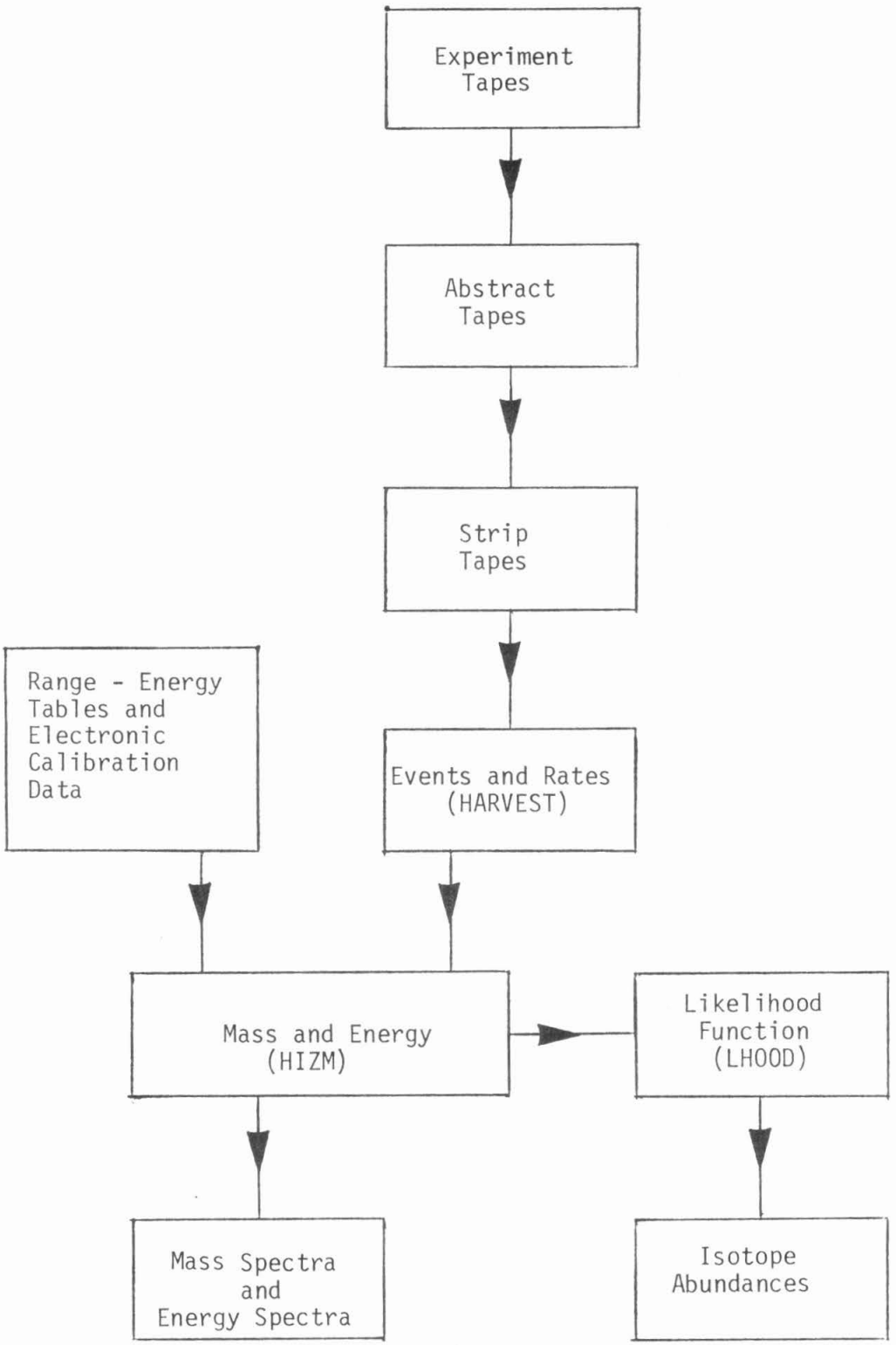
Experiment Tapes
Abstract Tapes
Strip Tapes
Range - Energy Tables and Electronic Calibration Data
Events and Rates (HARVEST)
Mass and Energy (HIZM)
Likelihood Function (LHOOD)
Mass Spectra and Energy Spectra
Isotope Abundances

submitted as input to a program called HIZM, which calculates the charge, mass, energy (corrected for the mylar window), and range of each event. The output of this program is used to obtain element abundances, energy spectra, mass spectra, etc. Knowledge of the channel-energy conversion and of the range - energy relation is required by the program HIZM. The channel - energy conversion is obtained from electronic calibration performed on the ground (see section II - C). The range - energy relation is based on calibration data for hydrogen, helium, nitrogen, and oxygen and is based on calculation for other elements. (See Appendix C.) A program called LHOOD uses the mass data to calculate the likelihood function for the relative isotopic abundances.

A separate, auxilliary program called MASCON, which is not involved in the data analysis, is used to calculate the isotope contours on a ΔE-E' plot. With the channel - energy conversion and the range - energy relation as input, MASCON calculates the D2 channel and the total energy (corrected for the mylar window) as a function of the D5 channel for any isotope.

Because of the different hardware and the larger number of interesting events, a slightly different procedure is used to analyze the calibration data. Figure A - 2 illustrates the relevant flow diagram. The pulse height data from each calibration run are recorded on one file of the PACE* tape.

---

*Acronym for Pulsed Analog to digital Converter and Encoder.

FIGURE A - 2

Flow diagram illustrating processing sequence of calibration data.

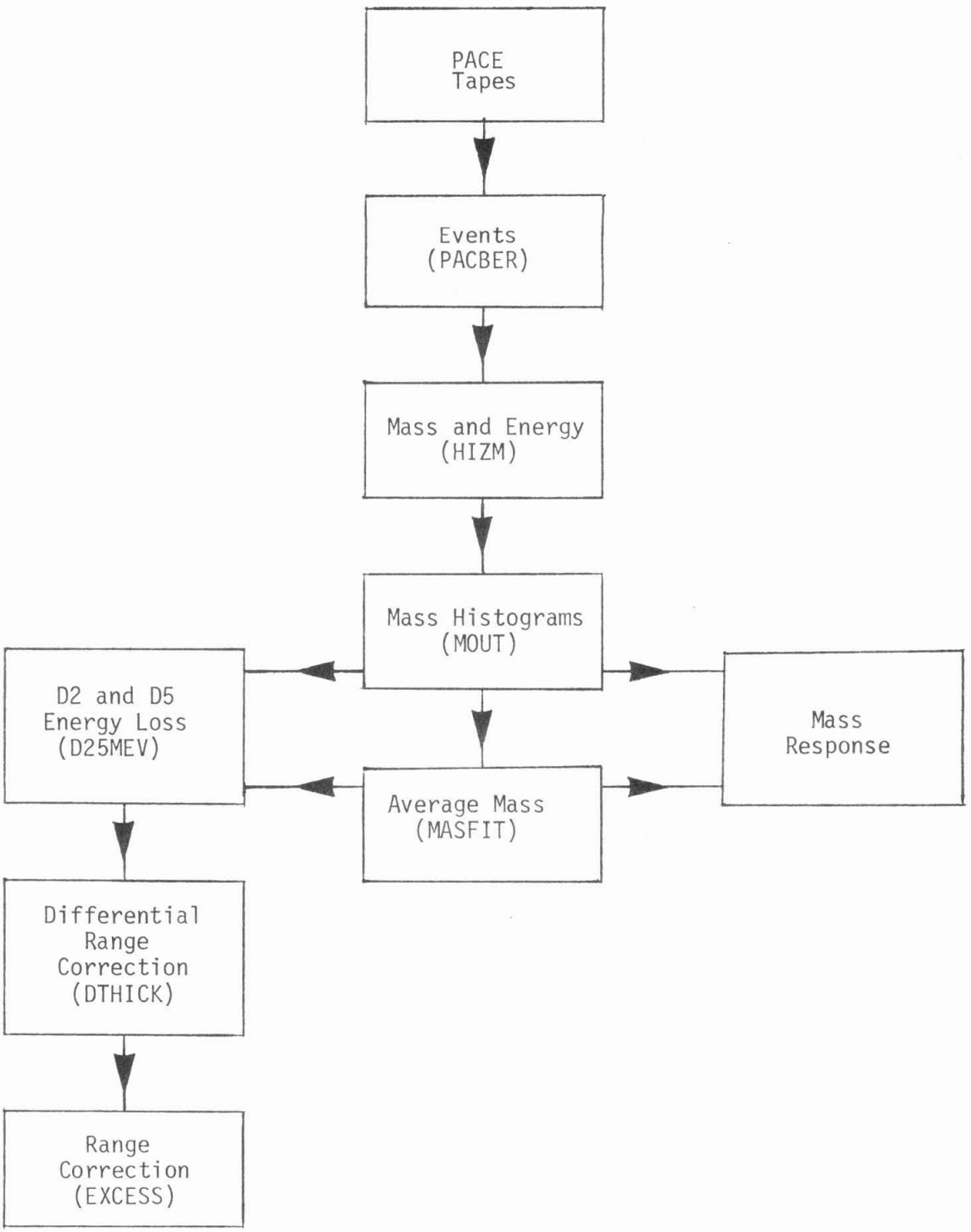
PACE
Tapes
Events
(PACBER)
Mass and Energy
(HIZM)
Mass Histograms
(MOUT)
D2 and D5
Energy Loss
(D25MEV)
Mass
Response
Average Mass
(MASFIT)
Differential
Range
Correction
(DTHICK)
Range
Correction
(EXCESS)

The program PACBER reads the PACE tape, calculates the number of events at each D2, D5 coordinate pair, and writes the results on tape. This tape is used as the input for the program HIZM, which calculates the charge, mass, energy, and range of each event, and creates a new tape as output. Note that since the calibrated range - energy relation is not known at this step of the analysis, other range - energy tables are used. (See Appendix C.) Using the new tape as input, the program MOUT calculates the means and standard deviations of the mass, energy, and range distributions and also produces mass histograms, which are converted into punched cards. Since several isotopes were obtained simultaneously for much of the calibration data, it is necessary to properly sort out the several mass peaks. Using the method of least squares, mass peaks are fitted to the mass histograms by the program MASFIT, and the result is a mean mass, a standard deviation, and a height for each mass peak. The outputs of MOUT and MASFIT can be used directly to obtain the isotope response of the instrument.

Several more steps are needed to obtain the calibrated range - energy tables. The outputs of MOUT and MASFIT are used by the program D25MEV to calculate the average energy loss in D2 and in D5 for a given charge, mean mass, and total energy. This program used the same range - energy tables that were originally used by HIZM to calculate the mass. Note that with this procedure

the isotopes have already been separated, and it is relatively easy to go back and calculate the average D2 and D5 energy loss for each isotope. It would have been more difficult to calculate the average D2 and D5 energy loss directly from the raw data, since, with an rms mass resolution of ~ 0.3 amu (for oxygen), it is not possible to associate the correct isotope with each event on an individual basis. The program DTHICK uses the D2 and D5 energy loss information to calculate a differential correction (equation C - 5) to the range - energy relation. Finally, the program EXCESS calculates a range - energy correction from the differential correction.

APPENDIX B

CROSS-TALK BETWEEN DETECTORS

There is an instrument anomaly on the IMP-7 EIS whereby, under certain circumstances,a particle that deposits energy in a certain combination of detectors can also trigger the discriminator of another detector in which it did not deposit any energy (Garrard, 1974a). This phenomeon is referred to as cross-talk. There are two manifestations of cross-talk which affect D25 events on IMP-7. Particles that deposit energy in both D2 and D5 have a certain probability of also triggering D6. In this instance the D2 pulse height is replaced in the telemetry by the D6 pulse height. Such events are identified by the D256 signature and by the zero pulse height in D6. In addition, particles that deposit a large amount of energy in D5 also trigger D4. Since D4 acts as an anticoincidence device, the event is not analyzed. D25 events on the IMP-8 EIS are not affected by cross-talk.

The cross-talk from the detector combination D25 into D6 was first observed during particle calibrations of the IMP-7 instrument at the Caltech Van de Graaff accelerator. A more detailed discussion than that presented here can be found in the report by Hurford (1974b).

Based on an analysis of solar flare events, the probability that a D25 hydrogen or helium event will result in cross-talk into

D6 is best expressed by the equation

$$P(A,B) = 0.5 \left\{1 + \text{erf}\left[0.1293 - 81.36\left(\frac{1.11}{A} - \frac{1}{B}\right)\right]\right\} \qquad B - 1$$

where P(A,B) is the cross-talk probability, erf represents the error function, and A and B represent the D5 and D2 pulse heights in units of channel number. The probability of cross-talk is greatest when both the D2 and D5 pulse heights are large, or when the D2 pulse height is ~ 0.9 the D5 pulse height. In order to establish a limit on the probability P(A,B) for elements with $Z \geq 3$, the number of D256 events with D5 channel $\geq$ 1500 and D6 channel = 0 were compared with the number of D25 events with D5 channel $\geq$ 1500. As a result, the maximum cross-talk probability was determined to be 0.40 $\pm$ .02. To calculate the cross-talk probability as a function of A and B for particles with $Z \geq 3$, equation B - 1 is used for values of $P(A,B) \leq 0.4$. For all other values of A and B, the probability P(A,B) is set equal to 0.4.

For the nitrogen and oxygen isotopic abundance measurements of Table III - D, the cross-talk probability given by this technique is identical for all isotopes. For the element abundances of Table III - 3, the average cross-talk probability varies both as a function of energy and of element. The correction factors for cross-talk are listed in Table B - 1 appropriate to the elements and

TABLE B-1

Correction Factors for D25→D6 Cross-Talk on IMP-7 EIS

Element	Energy (MeV/nucleon)	Minimum Correction Factor*	Maximum Correction Factor*	Average Correction
He	6.0 - 12.7			1.00
O	6.0 - 12.7	1.67	1.67	1.67
Li	4.9 - 12.5	1.14	1.67	1.30
O	4.9 - 12.5	1.00	1.67	1.60
Be	4.9 - 12.5	1.40	1.67	1.56
O	4.9 - 12.5	1.00	1.67	1.60
B	4.9 - 12.5	1.61	1.67	1.66
O	4.9 - 12.5	1.00	1.67	1.60
C	4.9 - 12.5	1.67	1.67	1.67
O	4.9 - 12.5	1.00	1.67	1.60
N	5.6 - 12.5	1.67	1.67	1.67
O	5.6 - 12.5	1.67	1.67	1.67
Ne	7.2 - 11.1	1.67	1.67	1.67
O	7.2 - 11.1	1.67	1.67	1.67
Mg	7.7 - 10.5	1.67	1.67	1.67
O	7.7 - 10.5	1.67	1.67	1.67
Si	8.1 - 10.2	1.67	1.67	1.67
O	8.1 - 10.2	1.67	1.67	1.67

To obtain the number of D25 events that would have been observed if there were no cross-talk, the observed number of events should be multiplied by the correction factor.

*Calculated at the energy for which the cross-talk correction is a minimum.

+Calculated at the energy for which the cross-talk correction is a maximum.

energy intervals of Table III - 3. To obtain the average cross-talk correction factor, the lithium, beryllium, and boron differential fluxes were assumed to be independent of energy. The shape of the oxygen spectrum was taken from the IMP-8 data (Figure III - 4). The shapes of the carbon and nitrogen spectra are immaterial since the cross-talk correction factors are energy independent at these energies. Since most of the cross-talk events (i.e., D256 events with D6 pulse height = 0) within the D5 channel region (channel 506 - 1187) spanned by the 6.0 - 12.7 MeV/nucleon helium are due to helium particles, these events were included in the calculation of the helium flux. Therefore, no further correction for helium cross-talk was necessary.

From Tables B - 1 and III - 3 the size of the cross-talk corrections can be compared with the statistical uncertainties in the element ratios. A correction for cross-talk was made in Table III - 3 only to the He/O ratio. The N/O, Ne/O, Mg/O, and Si/O ratios are unbiased by the cross-talk since the correction factors are the same for all elements. For the B/O and C/O ratios, a correction for cross-talk would be much smaller than the statistical uncertainties in the ratios. If a correction factor had been applied to the Li/O and Be/O ratios of Table III - 3, then the upper limits to the ratios would have been slightly reduced. However,since only upper limits were obtained, the values in Table III - 3 are valid without a cross-talk correction.

The cross-talk from D5 into D4 was first observed during particle calibrations at the Berkeley Bevatron.* This type of cross-talk arises from the signal side of D5 being adjacent to the signal side of D4. In Figure II - 1 the signal side of D5 is on top, and the signal side of D4 is on bottom. Because of the large detector areas and the small spacing between D4 and D5, the two detectors are capacitively coupled. Thus, a large signal in D5 can cause the D4 discriminator to trigger. For a more detailed discussion of the D5 → D4 cross-talk, the reader is referred to the report by Vidor (1975c).

To evaluate the D5 → D4 cross-talk, the IMP-7 and IMP-8 oxygen intensities were compared. The energy interval for which the comparison was made extended to the highest energy for which element abundances were calculated for the IMP-7 instrument. (See Table III-3.) Since D25 events on the IMP-8 instrument are not affected by cross-talk, the IMP-8 instrument provides a reliable measurement of the oxygen intensity. Correcting the IMP-7 intensity for D25 → D6 cross-talk, the resulting intensities of the 5.21 - 12.74 MeV/nucleon oxygen are $4.4 \pm .6 \times 10^7$ particles/sec and $3.9 \pm .3 \times 10^7$ particles/sec for the IMP-7 and IMP-8 instruments respectively. Since, at these low energies, there is no evidence of a decreased IMP-7 flux resulting from D5 → D4 cross-talk, no correction was made for this effect.

---

*A telescope identical to that on the IMP-7 EIS was installed on the IMP-8 EIS for these calibrations.

APPENDIX C

CALIBRATED ISOTOPE RESPONSE

A. Introduction

In order to calculate the mass of nitrogen and oxygen isotopes using the ΔE - E' technique (see Section II-C), accurate knowledge of the range - energy relation is needed. To gain insight into the required accuracy, we shall derive an equation that expresses the relation between mass, range, and the measured energy loss (ΔE and E').

To first order, the range of a particle can be calculated from the known proton range (Evans, 1955). We shall express the range of the particle in a given material by

$$R(E,M,Z) = \frac{M}{Z^2} R_p \left(\frac{E}{M}\right) + \Delta R_{M,Z}(E) \qquad C\text{-}1$$

R is the range of a particle of energy E, mass M, and charge Z, where M and Z are in units of the proton mass and charge. R_p is the range of a proton of energy $\frac{E}{M}$. $\Delta R_{M,Z}$ is a range correction for a particle of mass M and charge Z. The value of $\Delta R_{M,Z}$ is defined by equation C-1. If the stopping power $\frac{dE}{dx}$ in a given material is a function of charge and velocity only, then the range of any isotope of element Z can be expressed in terms of the proton range and of the range correction of an isotope with mass M_Z:

$$R(E,M,Z) = \frac{M}{Z^2} R_p \left(\frac{E}{M}\right) + \frac{M}{M_z} \Delta R_{M_z,Z} \left(E \frac{M_z}{M}\right) \qquad C\text{-}2$$

An additional independent equation is needed to relate the mass to the measured energy loss ΔE and E':

$$R(E,M,Z) - R(E',M,Z) = T \qquad C\text{-}3$$

E is the total energy ($\Delta E + E'$) deposited in the two detectors D2 and D5, E' is the energy deposited in D5, and T is the thickness of D2.

Substituting equation C-2 into C-3 and rearranging terms, the calculated mass can be expressed as

$$M = \frac{Z^2 T}{R_p\left(\frac{E}{M}\right) - R_p\left(\frac{E'}{M}\right) + \frac{Z^2}{M_z}\left[\Delta R_{M_z,Z}\left(E\frac{M_z}{M}\right) - \Delta R_{M_z,Z}\left(E'\frac{M_z}{M}\right)\right]} \qquad C\text{-}4$$

The energies E and E' are measured quantities, and we shall assume, for the present, that the proton range and the range correction are known as a function of energy. For any charge Z the mass M can be calculated in a straightforward manner using an iterative procedure. It is interesting to note that the mass does not depend on either range alone but only on the difference between two ranges.

Using techniques similar to the one used to calculate the mass resolution (see Section II-C), it can be shown that the relative

uncertainty in mass is ~ 1.3 times as great as the relative uncertainty in the range - energy relation. Therefore, to calculate the mass of an ^{16}O nucleus to 0.5 amu, the range - energy relation must be known to 2.4%. By contrast, to calculate the mass of a ^{4}He nucleus to 0.5 amu, the range - energy relation must be known to 9.6%.

In light of this need for accurate range - energy information, we review the current state of knowledge in the energy region appropriate to this thesis. Several range - energy tables for protons in silicon have been published. (E.g. Janni, 1966; Bichsel and Tschalaer, 1967). Using the large amount of experimental data as a guide, the technique for producing the range - energy tables of protons has been considerably refined. For example, Janni (1966) estimates that his tables are typically accurate to better than 1%.

In order to use the proton range - energy tables for elements with $Z > 1$, the range corrections $\Delta R_{M_Z,Z}$ must be known. An alternative to using proton range - energy tables and an appropriate range correction is to use directly range tables for specific isotopes. Northcliffe and Schilling (N & S) (1970) have published range - energy tables for elements with $1 \leq Z \leq 103$ in a variety of media for the energy region $0.0125 \leq E \leq 12$ MeV/amu. Corrections were made for the effects of incomplete projectile ionization at low energies. The effects of incomplete ionization are to decrease the effective charge of the ion and thereby to reduce the stopping power and

increase the range of the particle. It should be noted that the N & S range - energy tables were derived with the assumption that the stopping power scales with Z^2, although for the value of Z they used an effective charge based on the ionization state as a function of energy. The dependence of the stopping power on Z^2 arises from Bethe's formula (Livingston and Bethe, 1937), and it has been the basis of many works on the subject of ionization energy loss. N & S claim that the overall accuracy of their tables is no better than 2%, implying an uncertainty of no less than 0.4 amu for the calculated ^{16}O mass.

Recent evidence, however, has pointed to deviations from the Z^2 scaling of the stopping power which was assumed by N & S. Several experiments have found a difference in the range of elementary particles of opposite charge. Barkas et al. (1963) found a 3% difference between the range of the Σ^+ and Σ^- hyperons at identical velocities. Heckman and Lindstrom (1969) reported a similar effect for positive and negative pions. In careful experiments with an absolute accuracy of 0.3%, Anderson et al. (1969) compared the stopping power of hydrogen and helium in tantalum and aluminum at several MeV/nucleon. They found that the stopping power of helium relative to hydrogen was larger than the factor of 4 predicted by the Bethe formula. The discrepancy was 2.6% in tantalum and 1.3% in aluminum at 2.5 MeV/nucleon,with the discrepancy decreasing at larger energies.

Ashley et al. (1972) and Jackson and McCarthy (1973) explained the deviations from the Bethe formula theoretically. Bethe's formula is based on the first Born approximation. By including the next higher order approximation, the authors found a term proportional to Z^3, the relative importance of which decreases with increasing velocity.

Sellers et al. (1973) and Kelley et al. (1973) performed experiments which support the inclusion of the Z^3 term for ^3He, ^4He, ^{12}C, ^{14}N, and ^{16}O from 2 - 10 MeV/amu. The discrepancies from the Bethe formula were typically several per cent. This compares with the 2.4% accuracy needed to calculate the ^{16}O mass to 0.5 amu.

B. Calibration

In order to determine the isotope response as a function of energy, a spare telescope, identical to that on the IMP-8 EIS, was calibrated at the Berkeley 88" Cyclotron. The primary ^{12}C, ^{14}N, and ^{16}O beams had energies up to 17 MeV/nucleon. Fragmentation nuclei provided calibration data for a variety of isotopes with $1 \leq Z \leq 9$.

In order to control the intensity, energy, and type of particle seen by the telescope, the primary beam was scattered from a target. A schematic illustration of the setup is shown in Figure C-1. Several targets were used throughout the calibration: a 1.4 mg/cm^2 thick gold target, tantalum targets of 11 mg/cm^2,

FIGURE C - 1

Schematic illustration (not drawn to scale) of the scattering chamber at the Berkeley 88" Cyclotron. The detector system D can move along a rail (dashed line) concentric with the chamber. The target T is at the center of the chamber, and it can rotate about its axis. Particles are transmitted when the target is oriented as the solid line, and they are reflected when the target is oriented as the dotted line.

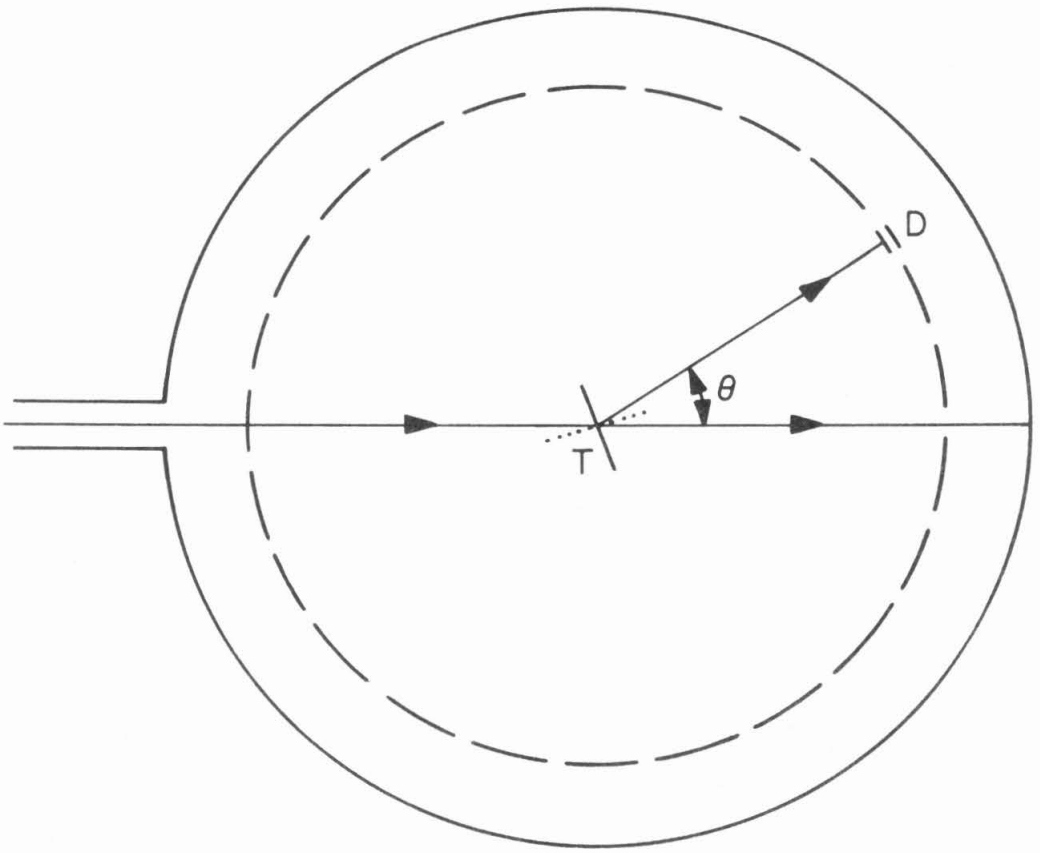
D
θ
T

41 mg/cm^2, and 55 mg/cm^2, a 25 mg/cm^2 polyethylene target, and a 2 g/cm^2 lead target. At small values of the scattering angle θ ($\leq$40 degrees for this setup), a large fraction of the particles reaching the detector system were elastically scattered by the gold and tantalum targets. By varying the scattering angle, the intensity of the elastically scattered beam was easily controlled. In addition, inelastic scattering reduced the energy of the particles, or, through nuclear interactions, produced a variety of isotopes and elements. The gold and tantalum targets were thin enough to allow the primary beam to be transmitted. However, since the ionization energy loss in the targets is a function of the target thickness, the energy reaching the detector system could be controlled by using the proper thickness target. The lead target was thick enough to stop the primary beam. By scattering the beam off the thick lead target, a continuous energy spectrum was obtained. The polyethylene target gave rise to an abundance of hydrogen and helium isotopes.

The major portion of calibration time was spent looking at those events that triggered the detectors D2 and D5. The signals from the detectors were processed by the PACE system. (See Marshall, 1974.) This is a highly versatile system which includes a 2048 channel pulse height analyzer. By properly adjusting the amplifier gains, full advantage was taken of the system's high resolution. From pulser calibrations it was determined that the system was

linear to ~ 0.03%, thus allowing use of only two parameters - gain and offset - to describe the calibration.

In the energy region for which nitrogen and oxygen isotopes can be measured in flight, our goal was to measure the mass response to within 0.1 amu. Since drifts in the electronics (offset and gain) cause drifts in the calculated mass (see Sections II-C, III-D), the electronic stability was checked with periodic calibrations. At constant temperature, the electronics were stable as a function of time. However, the temperature coefficient of the gain was ~ 0.1%/^{0}C, and during calibration runs the temperature varied by almost 5^{0}C. The largest contribution to the temperature coefficient was due to the preamplifiers. In order to improve the measurement of the isotope response, a temperature probe was placed near the preamplifiers. The temperature readout was digitized in 0.1^{0}C intervals and was monitored often. To obtain the approximate electronic calibration for each particle run*, the temperature measurements were used to perform linear interpolations between the immediately preceding and following electronic calibrations+.

---

*A typical run lasted about 5 minutes.

+For one case, in which there was a very rapid temperature change, a time rather than a temperature interpolation was performed. Since the temperature probe reaches temperature equilibrium more quickly than the massive preamplifiers, the probe did not reflect the true preamplifier temperatures in this one instance.

Following procedures used in Section II-C, the rms mass uncertainties due to the electronics are estimated in Table C-1 for ^{4}He, ^{14}N, and ^{16}O. The nitrogen and oxygen mass uncertainties are evaluated at the energies corresponding to the average energies of the quiet time flight data, while the helium mass uncertainties are evaluated at the average energy of the helium data that were used to determine the D2 thickness of the IMP-7 EIS telescope. The total mass uncertainties are obtained by combining the individual contributions in quadrature. It should be noted that the amplifier gains used for the helium calibrations differed from the amplifier gains for the nitrogen and oxygen calibrations. This explains some of the differences in the energy uncertainties between helium and the other two elements.

For a detailed list of the individual electronic and particle calibration runs, the reader is referred to the report by Vidor (1975b).

C. Results

A ΔE - E' plot for a sample run is shown in Figure C-2. The elements shown resulted from the nuclear interactions of a ^{14}N beam with a tantalum target. Note that the tracks for ^{6}Li, ^{7}Li, ^{8}Li; ^{7}Be, ^{9}Be, ^{10}Be; ^{10}B, ^{11}B, and ^{12}B are easily identifiable. In addition, a small amount of other isotopes, such as ^{9}Li, can be identified from the plot.

TABLE C - 1

Rms Mass Uncertainties Due to Electronics

	^{4}He (3.7 MeV/nuc)		^{14}N (7.6 MeV/nuc)		^{16}O (8.5 MeV/nuc)	
	MeV	amu	MeV	amu	MeV	amu
D2 Gain	0.001	0.002	0.008	0.006	0.009	0.007
D2 Offset	0.002	0.003	0.003	0.002	0.003	0.002
D2 Linearity	0.003	0.005	0.006	0.005	0.006	0.005
D5 Gain	0.004	0.0006	0.02	0.002	0.03	0.002
D5 Offset	0.002	0.0004	0.003	0.0002	0.003	0.0002
D5 Linearity	0.01	0.002	0.008	0.007	0.008	0.005
TOTAL		0.007		0.011		0.010

FIGURE C - 2

Plot of D2 (ΔE) vs. D5 (E') indicating typical isotope separation for the elements lithium, beryllium, and boron.

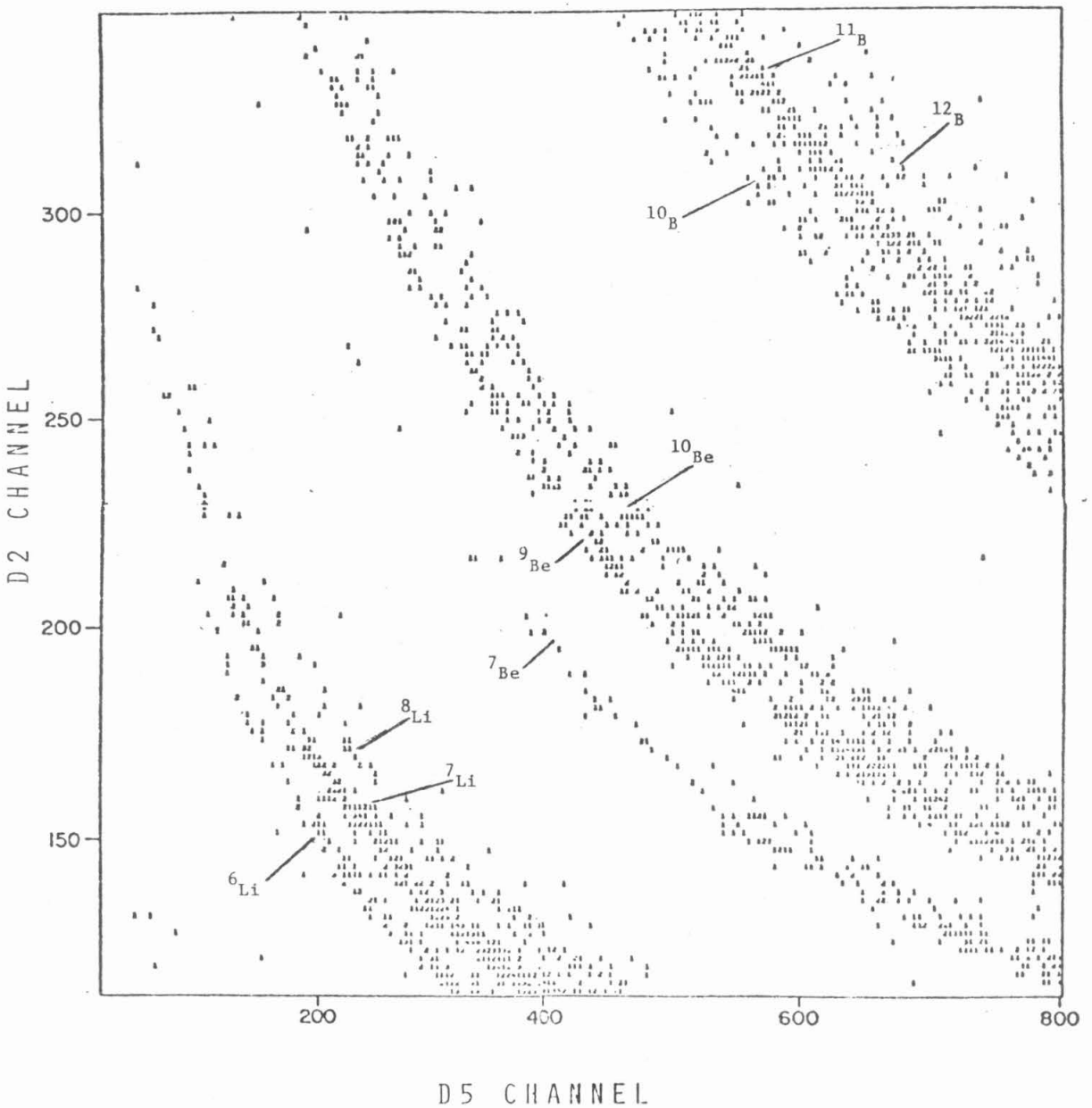
11B
12B
10B
10Be
9Be
7Be
8Li
7Li
6Li
300
250
200
150
200
400
600
800
D2 CHANNEL
D5 CHANNEL

The mass response of the instrument was investigated for the isotopes of hydrogen, helium, nitrogen, and oxygen. In order to calculate the mass from equation C-4, a range - energy relation had to be assumed. The analysis was done with two sets of range - energy tables. The first set was based on Janni's (1966) table for protons in silicon. To calculate the range for elements other than hydrogen, the range correction term in equation C-4 was assumed to be 0. The second set was also based on Janni's table for protons in silicon, but with a non-zero range correction for element Z, obtained by comparing the N & S range - energy table for element Z in aluminum with their table for protons in aluminum. It was assumed that the range correction, expressed in g/cm^2, was identical in silicon and aluminum. If the range correction were due to only electron pickup effects, one would expect the range correction to increase monotonically with energy and to approach a constant value at energies above which the projectile is essentially fully ionized. In fact, the range correction calculated from the N & S tables exhibits minor irregularities at high energies (~ 12 MeV/amu). Therefore, our calculated range correction was arbitrarily set equal to a constant at high energies.

The mass response of the instrument to protons is indicated in Figure C-3. A D2 thickness T (see equation C-4) of 44.85μ was chosen to properly normalize the proton mass data. Note that T is the only free parameter in equation 4. The same value of T must be used to calculate proton masses at all energies and also the

FIGURE C - 3

Calculated ^{1}H mass as a function of energy in D2 plus D5.

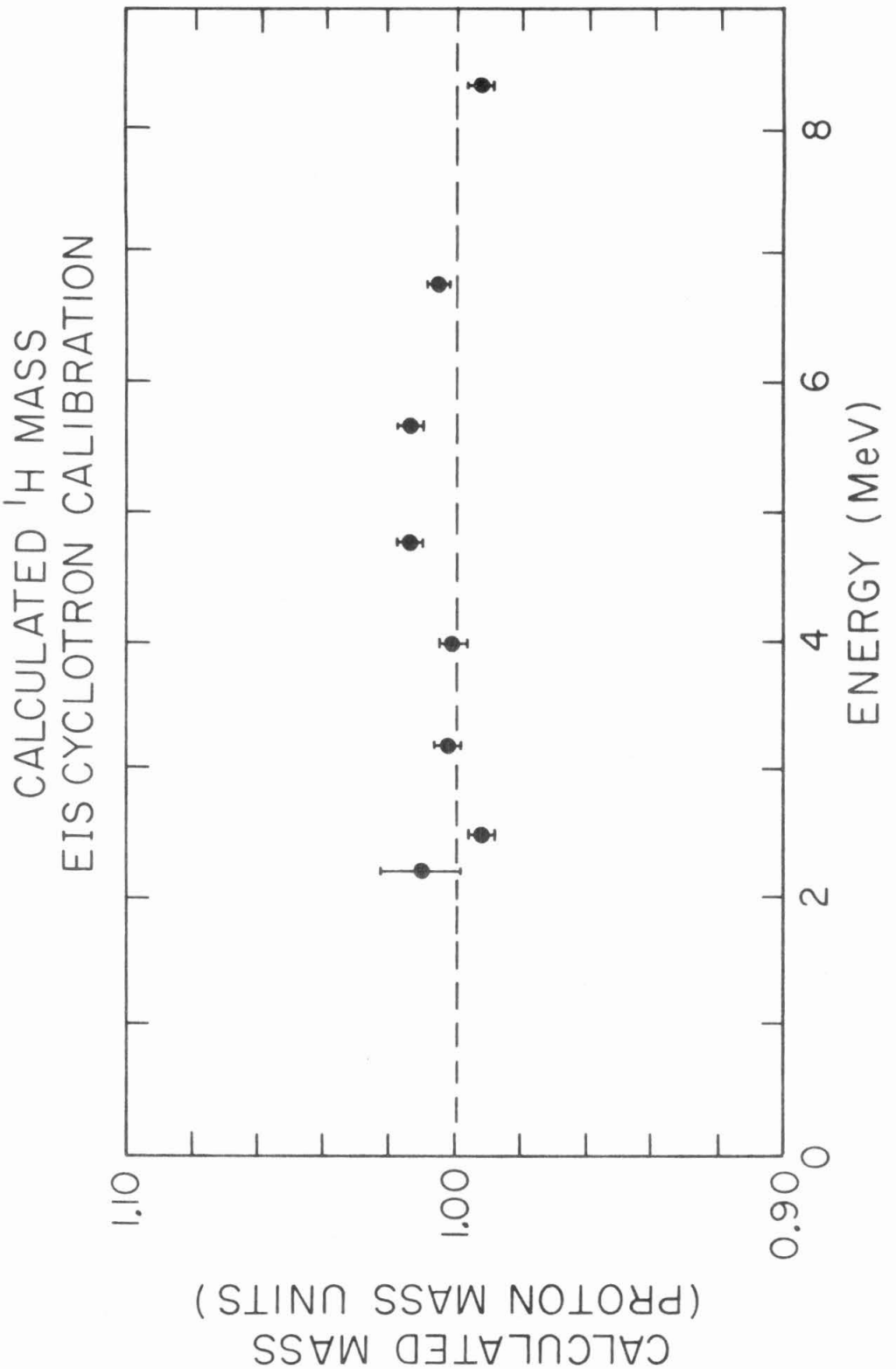
CALCULATED ^{1}H MASS
EIS CYCLOTRON CALIBRATION
CALCULATED MASS
(PROTON MASS UNITS)
1.10
1.00
0.90
0
2
4
6
8
ENERGY (MeV)

masses of other isotopes and elements. The calculated proton mass is at all energies within 0.014 proton mass units (pmu)* of 1.000 pmu over the entire measured energy range with an rms spread of 0.008 pmu in the observed mass. To within a precision of 0.6%, Janni's range - energy table for protons in silicon is in good agreement with our calibration data.

Using the same D2 thickness of 44.85μ that was used for protons, the mass of alpha particles was calculated as a function of energy. Figure C-4 illustrates the results obtained using the two sets of range - energy tables described previously. As expected, the two sets of tables give the same result at high energies where the helium is fully ionized. The observed helium mass is larger than the true mass, implying that the stopping power, as measured by ΔE in D2, is larger than the value predicted from our range - energy table for helium. This is qualitatively consistent with the theory of Ashley et al. (1972) and of Jackson and McCarthy (1973), in which a Z^3 term is included in the stopping power formula. The calculated helium mass approaches the true mass at higher energies, consistent with the decreasing importance of the Z^3 term at higher energies. Note that when no range correction is used, the calculated helium mass is closer to the true value than when a range correction obtained from N & S is used. The reason is that N & S correct for

---

*1.000 pmu = 1.007 amu

FIGURE C - 4

Calculated ^{4}He mass as a function of energy in D2 plus D5. The solid circles represent masses calculated with no range correction. The open circles were calculated using a range correction based on the tables of Northcliffe and Schilling (1970). The solid curve is associated with the solid circles, and the dotted curve is associated with the open circles. The curves represent the smoothed isotope response used to obtain a new range correction for helium. The dashed line indicates the true mass of a ^{4}He nucleus.

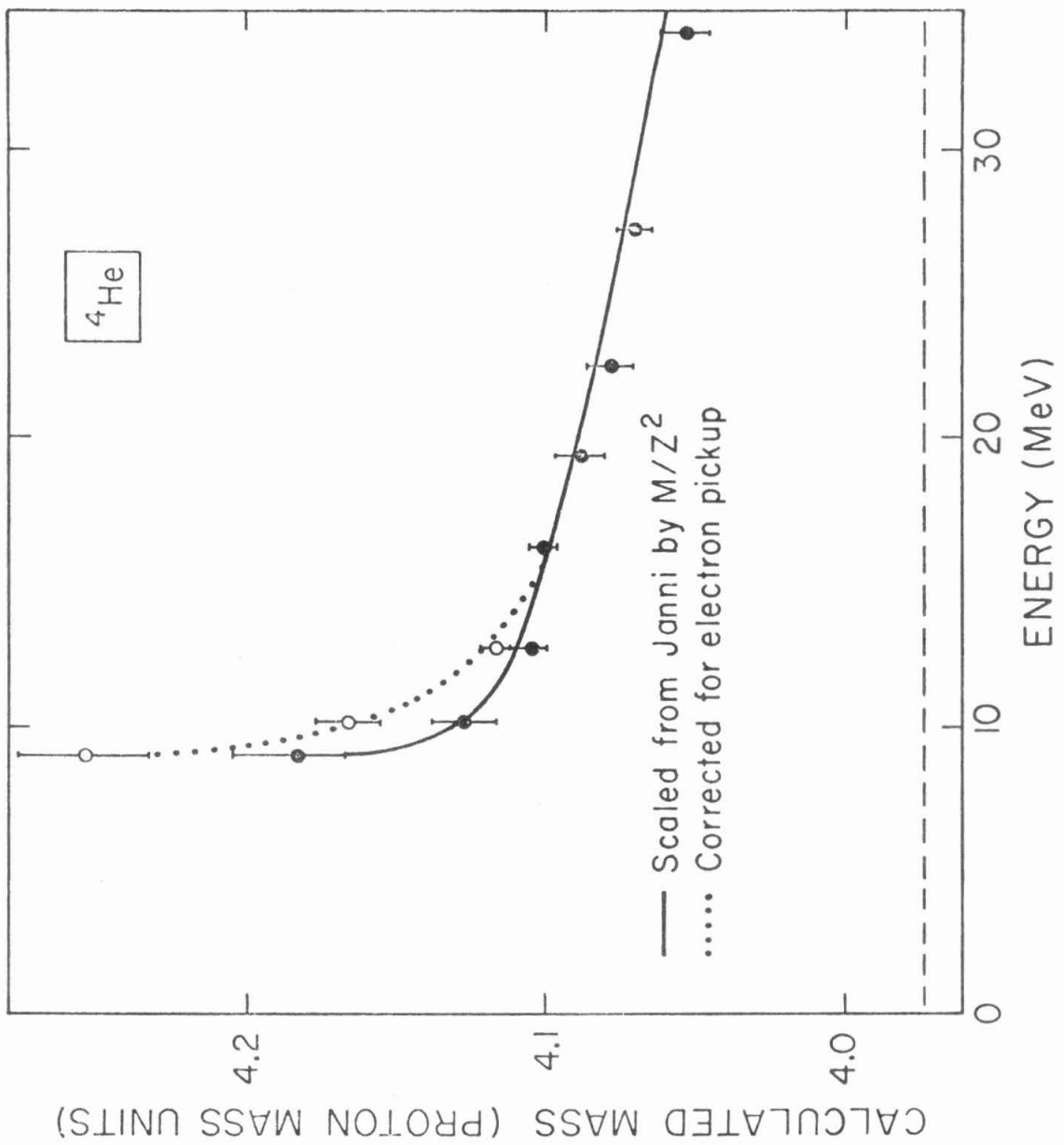
^{4}He
Scaled from Janni by M/Z^2
Corrected for electron pickup
CALCULATED MASS (PROTON MASS UNITS)
4.2
4.1
4.0
0
10
20
30
ENERGY (MeV)

electron pickup, which reduces the relative stopping power. However, they do not include the larger effect of the Z^3 term which increases the relative stopping power. Over the measured energy region, the calculated ^{4}He mass deviates from the true mass by 0.2 pmu at low energies and 0.1 pmu at the higher energies. This discrepancy is not important enough to seriously affect isotopic identification for helium.

The mass response to ^{14}N as a function of energy using the two sets of range energy tables is shown in Figure C-5. The two sets of tables give identical results at high energies. At high energies the calculated mass is too large. This is qualitatively consistent with the Z^3 correction term. Towards lower energies the calculated mass decreases if no range correction is assumed. This comes about because incomplete ionization of the ^{14}N, which becomes increasingly important at low energies, is not taken into account. On the other hand, the range correction obtained from N & S results in an increasing mass towards lower energies. At 10 - 15 MeV/nucleon the calculated ^{14}N mass is 0.5 pmu too high. The discrepancy between the true and calculated mass at lower energies depends on which of the two range - energy tables is used. The errors in the range - energy tables we used for nitrogen results in a large enough error in the mass that isotope identification is not possible unless the mass response of the instrument is known.

FIGURE C - 5

Calculated ^{14}N mass as a function of energy in D2 plus D5. The solid circles represent the masses calculated with no range correction. The open circles were calculated using a range correction based on the tables of Northcliffe and Schilling (1970). Unless shown, the error bars are comparable to or smaller than the circles representing the data points. The solid curve is associated with the solid circles, and the dotted curve is associated with the open circles. The curves represent the smoothed isotope response used to obtain a new range correction for nitrogen. The dashed line indicates the true mass of a ^{14}N nucleus.

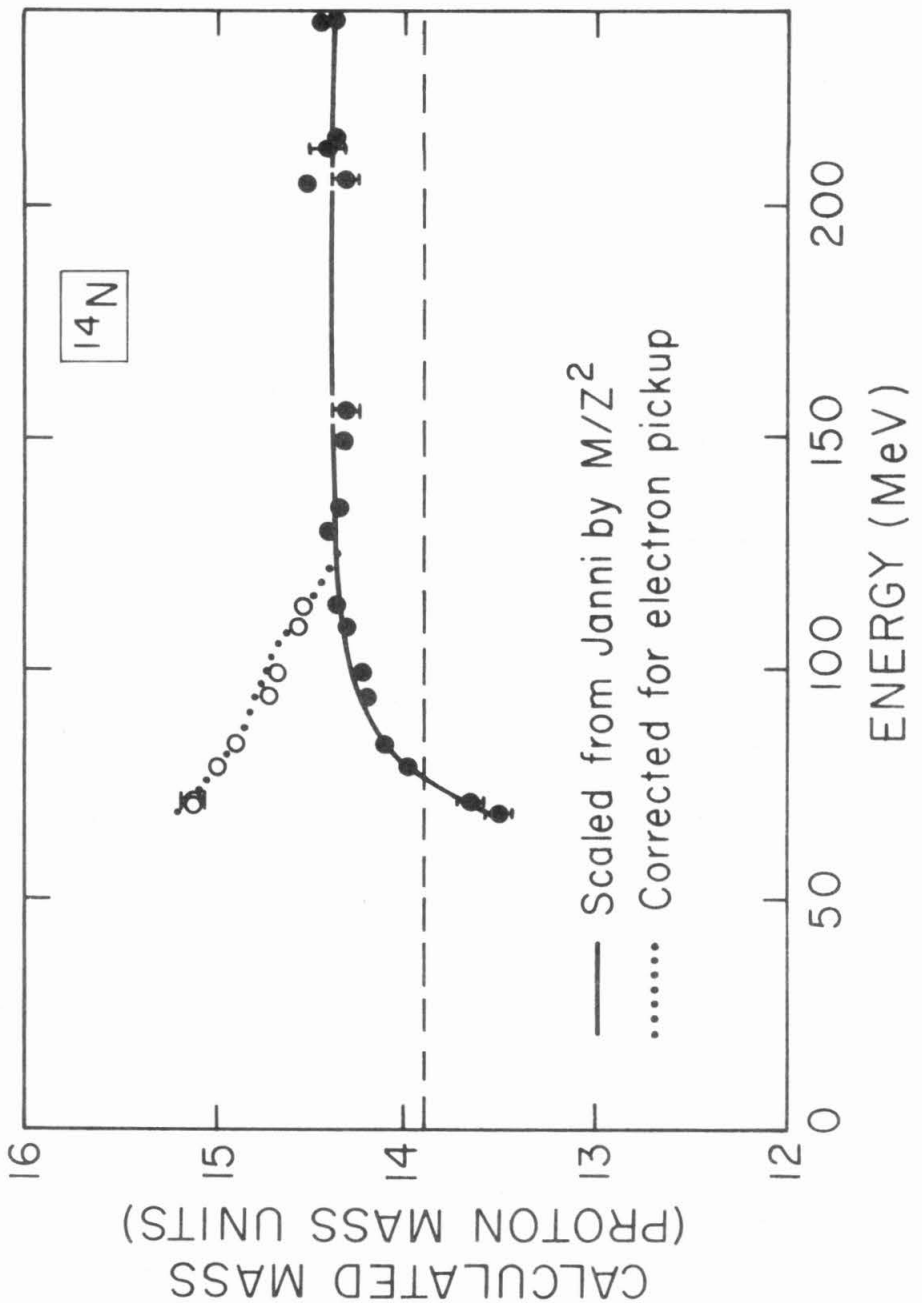
^{14}N
Scaled from Janni by M/Z^2
Corrected for electron pickup
CALCULATED MASS
(PROTON MASS UNITS)
ENERGY (MeV)
16
15
14
13
12
0
50
100
150
200

Large variations in the ^{16}O mass response were also observed as a function of energy. Mass histograms at different energies are shown in Figure C-6. To calculate the mass histograms in Figure C-6, a range correction based on the tables of N & S was used. At the lowest energies the mass response is varying rapidly as a function of energy. Although the energy interval for each histogram is less than 1 MeV/nucleon, the variation of the mass response in the energy interval can contribute to the broadening of the mass peak.

The mass response to ^{16}O as a function of energy using the two sets of range - energy tables is shown in Figure C-7. At high energies the calculated mass is 0.5 pmu too high. At low energies, depending on the range - energy table used, the mass is several pmu too high or too low. The kink in the curve obtained with a range correction for electron pickup arises from the high energy constant range correction mentioned previously. The range correction for ^{16}O was set equal to a constant value for energies above 7.5 MeV/nucleon with a discontinuity in the derivative $\frac{d}{dE}(\Delta R)$ at 7.5 MeV/nucleon. This gives rise to the discontinuity in the derivative $\frac{dM}{dE}$ observed in Figure C-7. Using our range - energy tables for oxygen, isotope identification is impossible below 13 MeV/nucleon unless the mass response of the instrument is known.

The smooth curves shown in Figures C-4, C-5, and C-7 define the

FIGURE C - 6

Mass histograms of ^{16}O as a function of energy. A range correction based on the tables of Northcliffe and Schilling (1970) was used to calculate the mass. The arrows indicate the true mass of an ^{16}O nucleus. Note that there may be minimal amounts of other isotopes in some of the histograms.

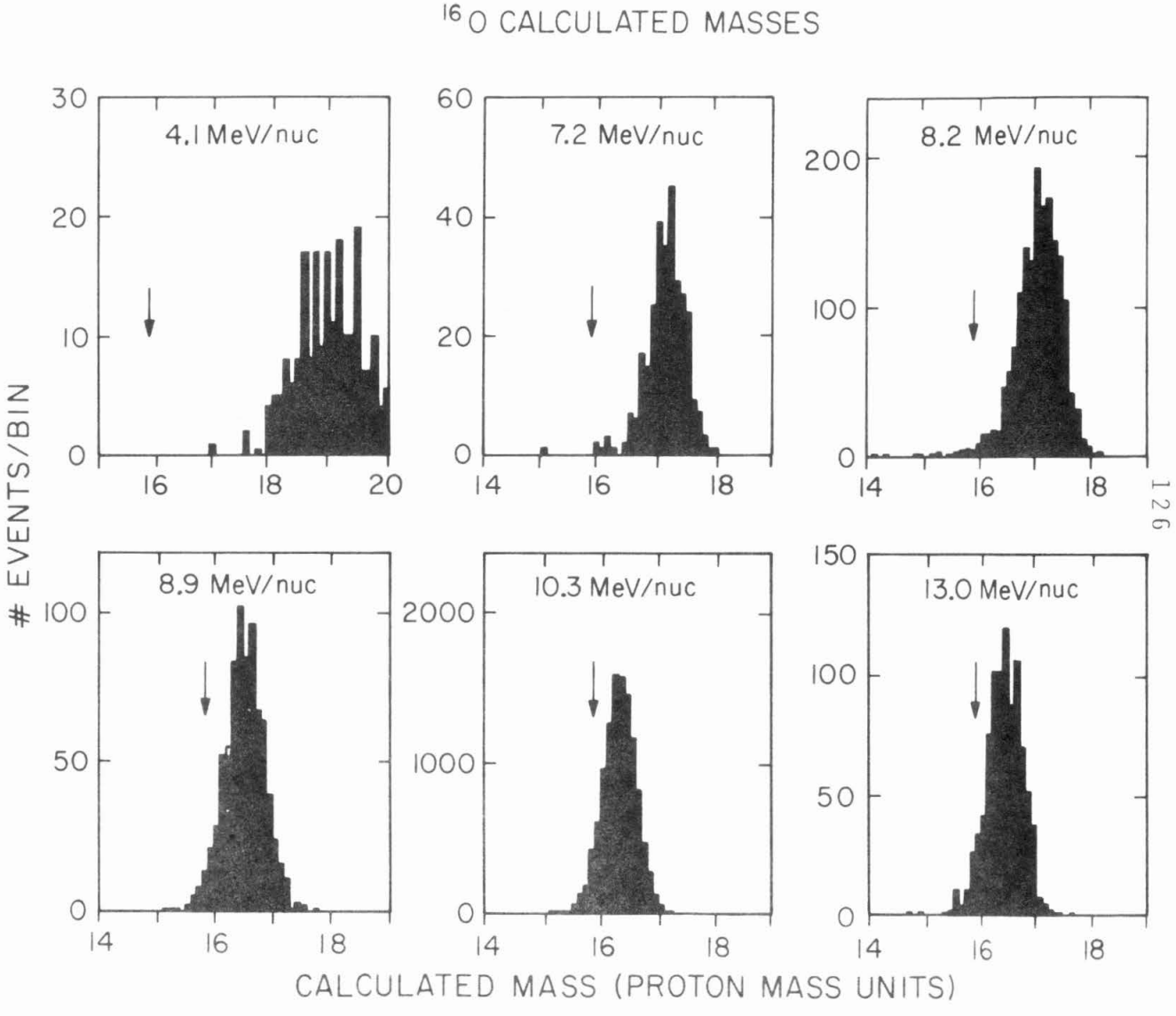
^{16}O CALCULATED MASSES
4.1 MeV/nuc
7.2 MeV/nuc
8.2 MeV/nuc
8.9 MeV/nuc
10.3 MeV/nuc
13.0 MeV/nuc
EVENTS/BIN
CALCULATED MASS (PROTON MASS UNITS)

FIGURE C - 7

Calculated ^{16}O mass as a function of the energy in D2 plus D5. The solid circles represent the masses calculated with no range correction. The open circles were calculated using a range correction based on the tables of Northcliffe and Schilling (1970). Unless shown, the error bars are comparable to or smaller than the circles representing the data points. The solid curve is associated with the solid circles, and the dotted curve is associated with the open circles. The curves represent the smoothed isotope response used to obtain a new range correction for oxygen. The dashed line indicates the true mass of an ^{16}O nucleus.

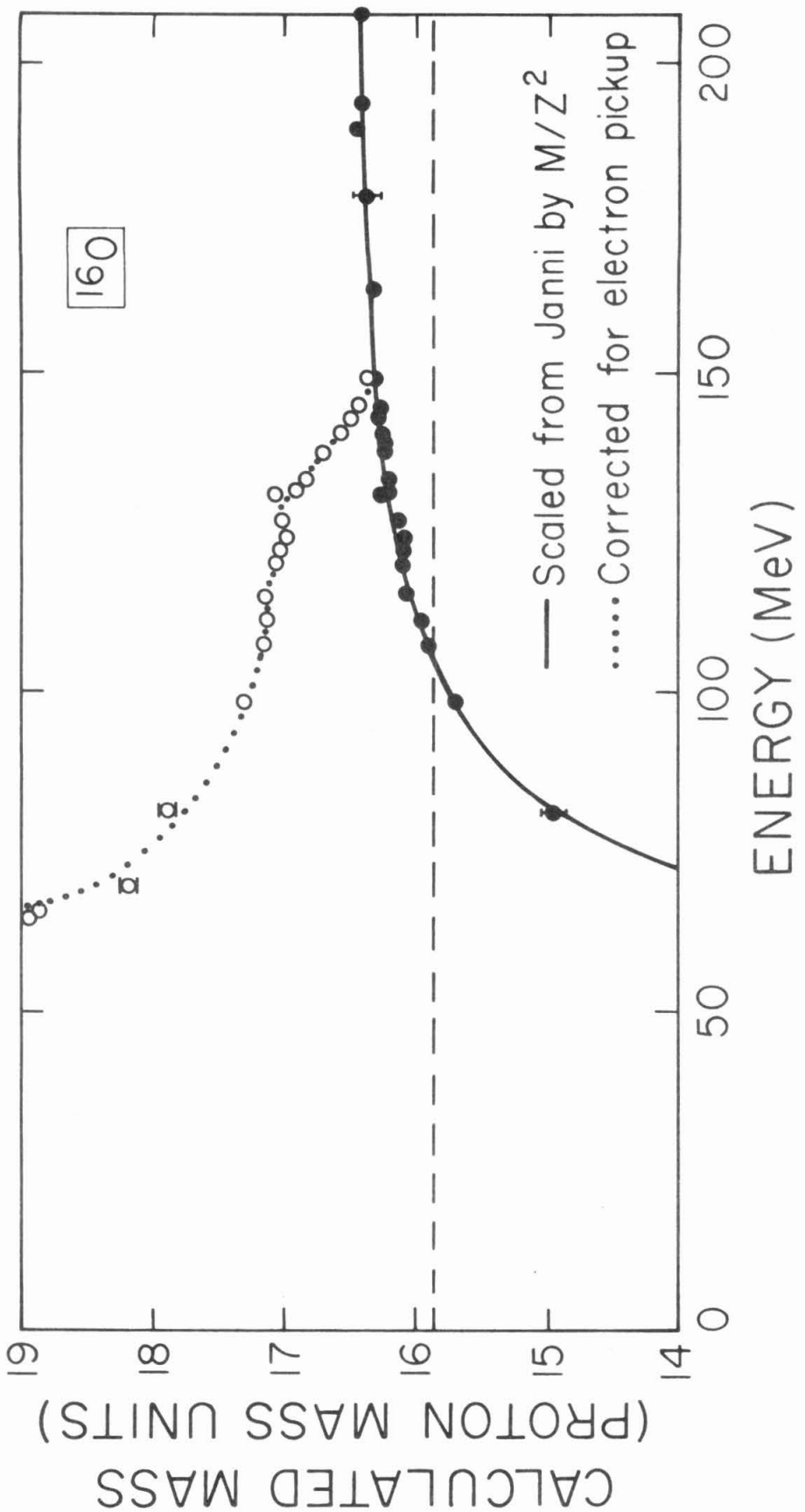
160
Scaled from Janni by M/Z²
Corrected for electron pickup
ENERGY (MeV)
CALCULATED MASS
(PROTON MASS UNITS)
0
50
100
150
200
14
15
16
17
18
19

mass response of the instrument to ^{4}He, ^{14}N, and ^{16}O. Note that the solid and dotted curves are not independent. One can be derived from the other since the relation between the two sets of range - energy tables is known.

It is useful to obtain a range correction to use in equation C-4 which gives the correct mass. The procedure used to obtain the proper range correction from the calibration data will now be outlined.

Equation C-4 can be rearranged as

$$\Delta R_{M_z,Z}(E) - \Delta R_{M_z,Z}(E') = T + \frac{M_z}{Z^2}\left[- R_p\left(\frac{E}{M_z}\right) + R_p\left(\frac{E'}{M_z}\right)\right] \qquad C\text{-}5$$

From the measured energies E and E', the thickness T, the isotope mass M_z, the charge Z, and the proton range - energy table, the difference in the range correction between any pair of energies E and E' can be calculated. Most quantities on the right hand side of the equation have already been calculated. T is known from the calibrated response to protons. For helium, nitrogen, and oxygen we shall take as M_z the masses of ^{4}He, ^{14}N, and ^{16}O. For the proton range - energy table it is reasonable to use Janni's table since it is in good agreement with our proton data. The quantity E is an independent variable. The only parameter on the right hand side of equation C-5 that is not known at this point is E'. However, it is easy to obtain E' from the calibration data. Using Janni's proton table and no range correction, the average mass as a function

of energy is known from Figures C-4, C-5, and C-7. The energy E' corresponding to the average mass can therefore be immediately calculated from equation C-4. Note that previously, the mass of each individual event with its associated ΔE and E' was calculated from equation C-4. However, the average energy E' over many events was not computed. Therefore, it is necessary to use equation C-4 to calculate the average E' from the known value of the average mass.

To obtain the range correction from the quantity $\Delta R_{M_z,Z}(E) - \Delta R_{M_z,Z}(E')$, a summation procedure was used. Symbolizing the difference between the range corrections at energies E_k and E_j by

$$\Delta\Delta R_{M_z,Z}(E_k,E_j) = \Delta R_{M_z,Z}(E_k) - \Delta R_{M_z,Z}(E_j) \qquad C\text{-}6$$

the range correction at energy E_K can be expressed as

$$\Delta R_{M_z,Z}(E_k) = -\left[\sum_{i=1}^{k-1} \Delta\Delta R_{M_z,Z}(E_i,E_{i+1})\right] + \Delta R_{M_z,Z}(E_1) \qquad C\text{-}7$$

Temporarily normalizing the range correction at energy E_1 to an arbitrary value ΔR_1, the range function $\Delta R_{M_z,Z}(E_k)$ can be obtained at those discrete energies E_k for which the ranges of energies

E_k and E_{k-1} are separated by T (i.e., E_k corresponds to the total energy E,and E_{k-1} corresponds to the residual energy E'). This procedure is illustrated graphically in Figure C-8. The result is a range correction at discrete energy points, as indicated by the open circles. Starting with a new energy E_1', the range correction ΔR_1' is normalized such that it is consistent with a smooth curve drawn through the circles. The range correction can then be calculated for the set of points symbolized by the squares. Continuing this procedure, a smooth range correction curve can be obtained at all energies.

As noted previously, our technique of measuring mass is insensitive to a constant offset in the range since equation C-4 depends only on the difference between ranges. Therefore, an arbitrary normalization to the range must be imposed at some energy. A reasonable normalization is that the range of a particle with zero energy is zero.

The resulting range corrections as a function of energy for ^{4}He, ^{14}N, and ^{16}O are illustrated in Figures C-9, C-10, and C-11. The dotted sections of the curves are linear extrapolations to zero energy. The extrapolations were necessary because the calibration runs did not produce enough events at low energies to allow us to accurately measure the mass response. However, the response was measured at all energies for which we can observe nitrogen and oxygen isotopes with the flight data.

FIGURE C - 8

Graphical representation of the method used to calculate the range correction. The ranges of the circles at adjacent energies are separated by T. This is also true for the squares.

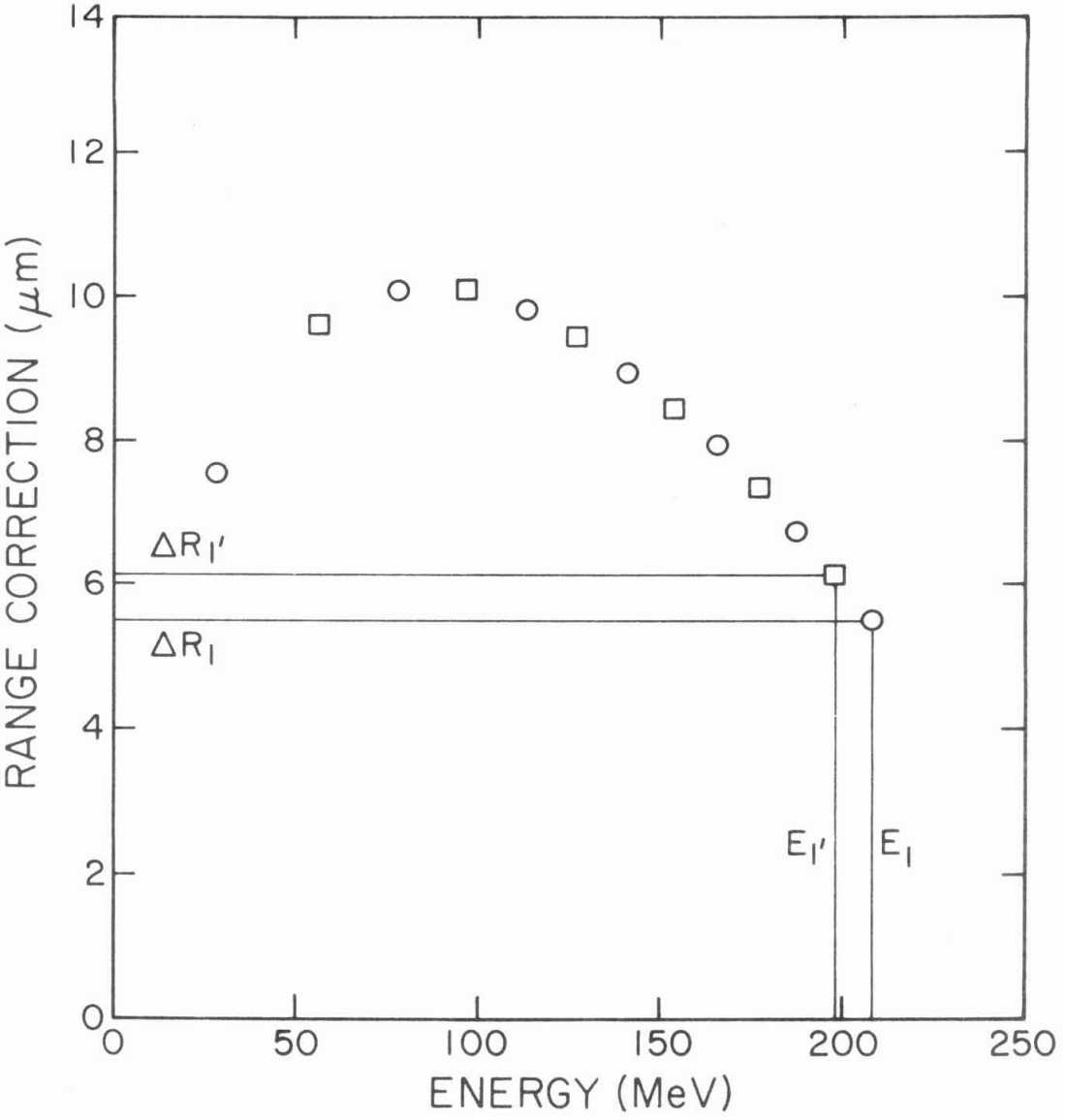
RANGE CORRECTION (μm)
ENERGY (MeV)
ΔR1'
ΔR1
E1'
E1
0
2
4
6
8
10
12
14
0
50
100
150
200
250

FIGURE C - 9

Range correction for ^{4}He in silicon. The dotted line represents a linear extrapolation.

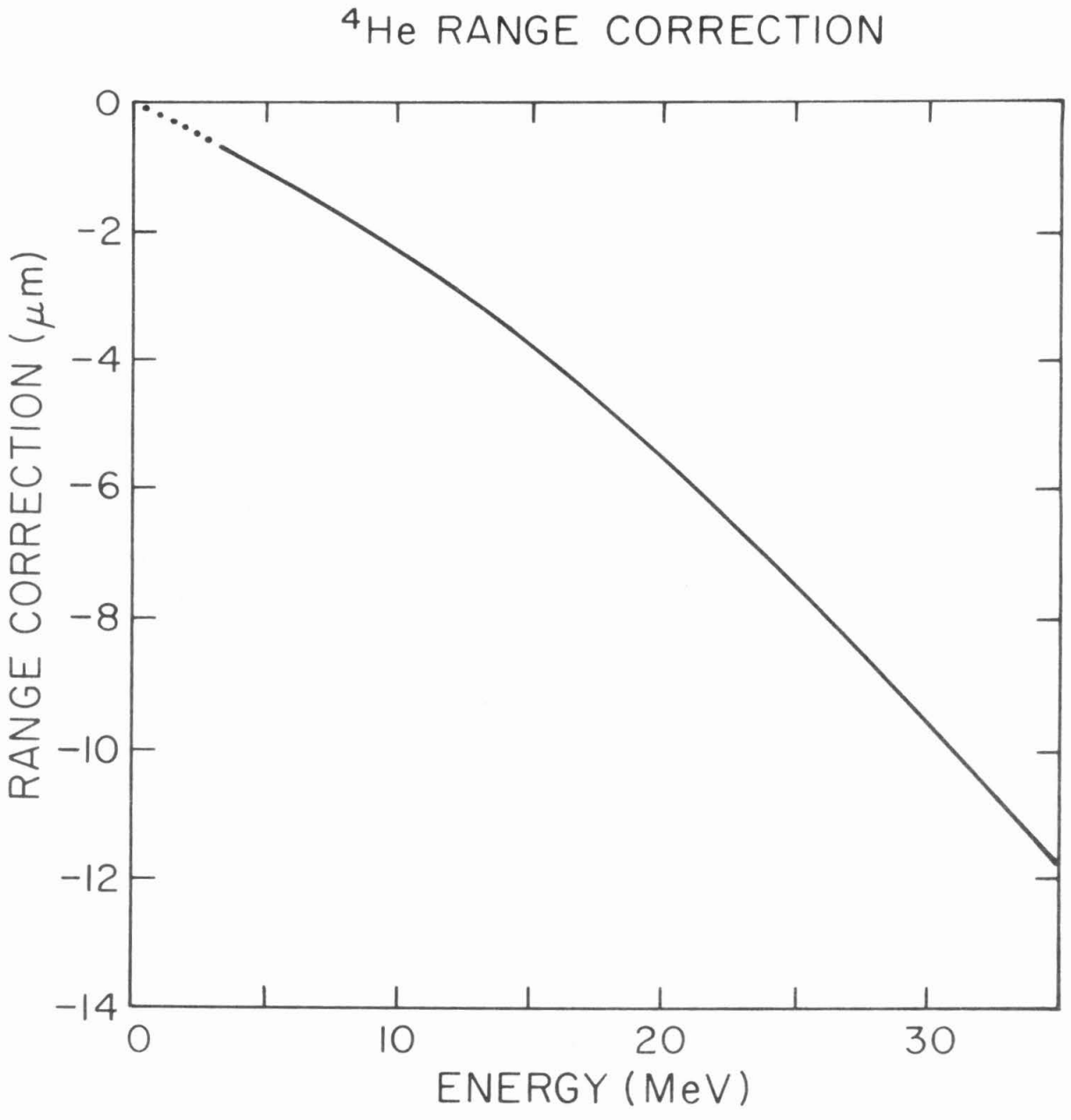
^{4}He RANGE CORRECTION
RANGE CORRECTION (μm)
0
-2
-4
-6
-8
-10
-12
-14
0
10
20
30
ENERGY (MeV)

FIGURE C - 10

Range correction for ^{14}N in silicon. The dotted line represents a linear extrapolation.

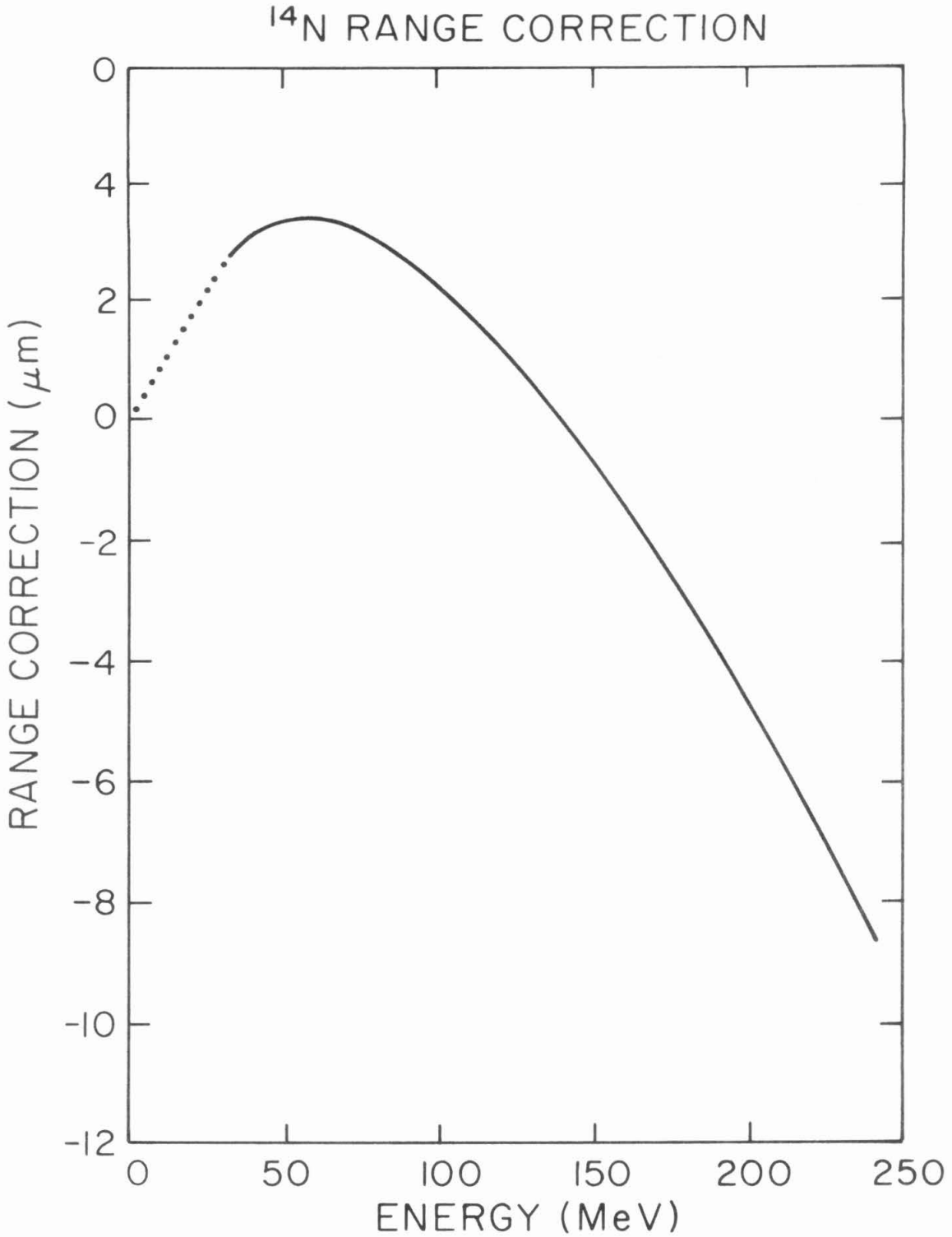
^{14}N RANGE CORRECTION
RANGE CORRECTION (μm)
0
4
2
0
-2
-4
-6
-8
-10
-12
0
50
100
150
200
250
ENERGY (MeV)

FIGURE C - 11

Range correction for ^{16}O in silicon. The dotted line represents a linear extrapolation.

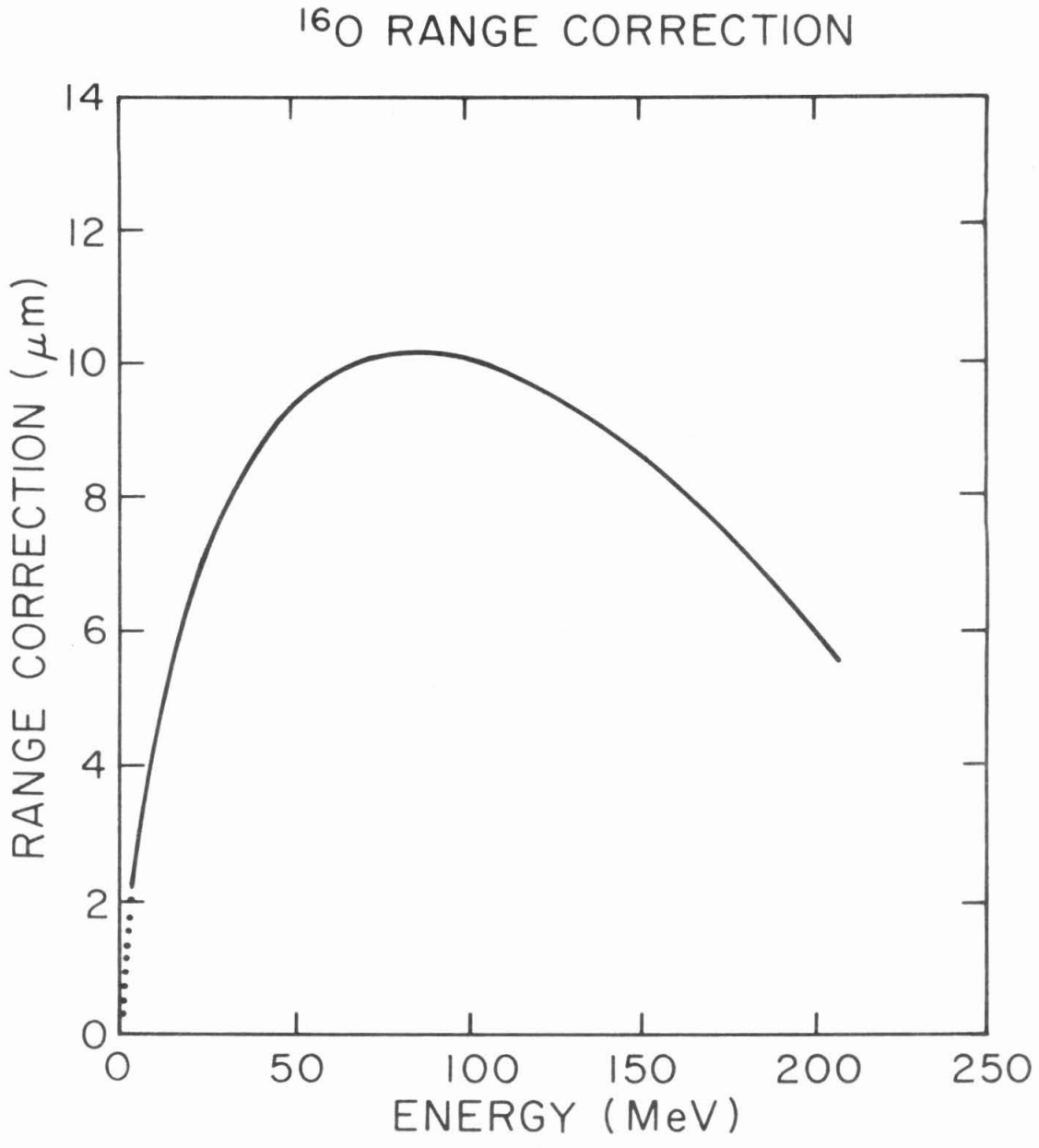
^{16}O RANGE CORRECTION
RANGE CORRECTION (μm)
0
2
4
6
8
10
12
14
0
50
100
150
200
250
ENERGY (MeV)

The range corrections obtained for ^{4}He, ^{14}N, and ^{16}O are listed in Tables C-2, C-3, and C-4 as a function of energy.

To estimate the uncertainty in the range correction, we must first estimate the uncertainty in the mass response. The mass response to ^{1}H, ^{4}He, ^{14}N, and ^{16}O is plotted in Figures C-3, C-4, C-5, and C-7. It is convenient to divide the uncertainties into two categories: those due to electronics (gain and offset shifts and non-linearities) and those due to all other effects. The effects of the electronics have been discussed in Section C-2. To estimate the importance of the second category, two contributions will be considered. Uncertainties in the data points due to statistics result in uncertainties in the mass response curve. In addition there are systematic uncertainties which can be estimated by the deviation of the smoothed mass response curve from the individual data points. These systematic uncertainties result either from fluctuations of the data points about the response curve or from an imperfect fit of the response curve to the data points.

The rms contributions to the mass uncertainties are estimated in Table C-5. For the flight data, it is necessary to know the nitrogen and oxygen mass response relative to the helium response. (See Section III-D.) Therefore, the contribution of the uncertainty in the helium response to the uncertainties in the relative nitrogen and oxygen responses is indicated in Table C-5. The total rms mass uncertainty is obtained by combining the individual contributions in quadrature.

TABLE C - 2

Range Correction for ^4He in Silicon

MeV	μm	MeV	μm	MeV	μm	MeV	μm	MeV	μm
(0.0	0.0)	(0.2	-0.05)	(0.4	-0.09)	(0.6	-0.14)	(0.8	-0.18)
(1.0	-0.23)	(1.2	-0.27)	(1.4	-0.32)	(1.6	-0.36)	(1.8	-0.41)
(2.0	-0.45)	(2.2	-0.50)	(2.4	-0.54)	(2.6	-0.59)	(2.8	-0.63)
(3.0	-0.68)	3.2	-0.72	3.4	-0.76	3.6	-0.80	3.8	-0.85
4.2	-0.94	4.4	-0.98	4.6	-1.02	4.8	-1.07	5.0	-1.11
5.2	-1.16	5.4	-1.20	5.6	-1.25	5.8	-1.29	6.0	-1.34
6.2	-1.38	6.4	-1.43	6.6	-1.47	6.8	-1.52	7.0	-1.56
7.2	-1.61	7.4	-1.65	7.6	-1.70	7.8	-1.75	8.0	-1.79
8.2	-1.84	8.4	-1.89	8.6	-1.94	8.8	-1.99	9.0	-2.04
9.2	-2.09	9.4	-2.14	9.6	-2.18	9.8	-2.24	10.0	-2.29
11.0	-2.56	12.0	-2.85	13.0	-3.15	14.0	-3.47	15.0	-3.79
16.0	-4.13	17.0	-4.48	18.0	-4.83	19.0	-5.19	20.0	-5.57
21.0	-5.95	22.0	-6.34	23.0	-6.73	24.0	-7.14	25.0	-7.54
26.0	-7.96	27.0	-8.36	28.0	-8.79	29.0	-9.22	30.0	-9.64
31.0	-10.07	32.0	-10.51	33.0	-10.94	34.0	-11.39	35.0	-11.84

Values in parentheses are based on linear extrapolation from higher energies.

TABLE C - 3

Range Correction for ^{14}N in Silicon

MeV	μm	MeV	μm	MeV	μm	MeV	μm	MeV	μm
(0.0	0.0)	(0.2	0.02)	(0.4	0.03)	(0.6	0.05)	(0.8	0.07)
(1.0	0.08)	(1.2	0.10)	(1.4	0.12)	(1.6	0.13)	(1.8	0.15)
(2.0	0.17)	(2.2	0.18)	(2.4	0.20)	(2.6	0.22)	(2.8	0.23)
(3.0	0.25)	(3.2	0.27)	(3.4	0.28)	(3.6	0.30)	(3.8	0.31)
(4.0	0.33)	(4.2	0.35)	(4.4	0.37)	(4.6	0.38)	(4.8	0.40)
(5.0	0.42)	(5.2	0.43)	(5.4	0.45)	(5.6	0.47)	(5.8	0.48)
(6.0	0.50)	(6.2	0.52)	(6.4	0.53)	(6.6	0.55)	(6.8	0.56)
(7.0	0.58)	(7.2	0.60)	(7.4	0.62)	(7.6	0.63)	(7.8	0.65)
(8.0	0.67)	(8.2	0.68)	(8.4	0.70)	(8.6	0.71)	(8.8	0.73)
(9.0	0.75)	(9.2	0.77)	(9.4	0.78)	(9.6	0.80)	(9.8	0.81)
(10.0	0.83)	(11.0	0.92)	(12.0	1.00)	(13.0	1.08)	(14.0	1.16)
(15.0	1.25)	(16.0	1.33)	(17.0	1.41)	(18.0	1.50)	(19.0	1.58)
(20.0	1.66)	(21.0	1.75)	(22.0	1.83)	(23.0	1.91)	(24.0	2.00)
(25.0	2.08)	(26.0	2.16)	(27.0	2.25)	(28.0	2.33)	(29.0	2.41)
(30.0	2.50)	(31.0	2.58)	(32.0	2.65)	33.0	2.73	34.0	2.79
33.0	2.73	34.0	2.79	35.0	2.86	36.0	2.92	37.0	2.98
38.0	3.03	39.0	3.07	40.0	3.12	41.0	3.17	42.0	3.21
43.0	3.25	44.0	3.29	45.0	3.32	46.0	3.34	47.0	3.37
48.0	3.39	49.0	3.40	50.0	3.42	51.0	3.43	52.0	3.44
53.0	3.45	54.0	3.45	55.0	3.45	56.0	3.45	57.0	3.45
58.0	3.45	59.0	3.45	60.0	3.44	61.0	3.43	62.0	3.43
63.0	3.41	64.0	3.40	65.0	3.39	66.0	3.38	67.0	3.36
68.0	3.34	69.0	3.32	70.0	3.30	71.0	3.28	72.0	3.26
73.0	3.23	74.0	3.21	75.0	3.18	76.0	3.16	77.0	3.13
78.0	3.10	79.0	3.07	80.0	3.04	81.0	3.01	82.0	2.98
83.0	2.94	84.0	2.91	85.0	2.87	86.0	2.84	87.0	2.80
88.0	2.77	89.0	2.73	90.0	2.69	91.0	2.65	92.0	2.61
93.0	2.57	94.0	2.53	95.0	2.48	96.0	2.44	97.0	2.40
98.0	2.35	99.0	2.31	100.0	2.26	101.0	2.22	102.0	2.17
103.0	2.12	104.0	2.07	105.0	2.02	106.0	1.97	107.0	1.92
108.0	1.87	109.0	1.82	110.0	1.76	111.0	1.71	112.0	1.66
113.0	1.61	114.0	1.55	115.0	1.50	116.0	1.44	117.0	1.39
118.0	1.33	119.0	1.27	120.0	1.22	121.0	1.16	122.0	1.10
123.0	1.05	124.0	0.99	125.0	0.93	126.0	0.87	127.0	0.81
128.0	0.75	129.0	0.69	130.0	0.62	131.0	0.56	132.0	0.50
133.0	0.44	134.0	0.38	135.0	0.31	136.0	0.25	137.0	0.18
138.0	0.12	139.0	0.06	140.0	-0.01	141.0	-0.07	142.0	-0.14
143.0	-0.20	144.0	-0.27	145.0	-0.34	146.0	-0.41	147.0	-0.48
148.0	-0.55	149.0	-0.62	150.0	-0.69	151.0	-0.75	152.0	-0.83
153.0	-0.90	154.0	-0.97	155.0	-1.04	156.0	-1.11	157.0	-1.19
158.0	-1.26	159.0	-1.33	160.0	-1.40	161.0	-1.48	162.0	-1.55
163.0	-1.63	164.0	-1.70	165.0	-1.78	166.0	-1.85	167.0	-1.93
168.0	-2.01	169.0	-2.08	170.0	-2.16	171.0	-2.24	172.0	-2.32
173.0	-2.40	174.0	-2.48	175.0	-2.56	176.0	-2.65	177.0	-2.72
178.0	-2.80	179.0	-2.88	180.0	-2.96	181.0	-3.05	182.0	-3.13
183.0	-3.21	184.0	-3.29	185.0	-3.38	186.0	-3.46	187.0	-3.55
188.0	-3.63	189.0	-3.72	190.0	-3.80	191.0	-3.89	192.0	-3.98
193.0	-4.06	194.0	-4.15	195.0	-4.24	196.0	-4.33	197.0	-4.42
198.0	-4.50	199.0	-4.59	200.0	-4.69	201.0	-4.78	202.0	-4.87
203.0	-4.96	204.0	-5.05	205.0	-5.14	206.0	-5.23	207.0	-5.32
208.0	-5.41	209.0	-5.51	210.0	-5.60	211.0	-5.70	212.0	-5.79
213.0	-5.88	214.0	-5.98	215.0	-6.08	216.0	-6.17	217.0	-6.27
218.0	-6.36	219.0	-6.46	220.0	-6.55	221.0	-6.65	222.0	-6.75
223.0	-6.85	224.0	-6.95	225.0	-7.05	226.0	-7.15	227.0	-7.25
228.0	-7.35	229.0	-7.45	230.0	-7.55	231.0	-7.65	232.0	-7.75
233.0	-7.85	234.0	-7.95	235.0	-8.06	236.0	-8.16	237.0	-8.26
238.0	-8.36	239.0	-8.47	240.0	-8.57	241.0	-8.68		

Values in parentheses are based on linear extrapolation from higher energies.

TABLE C - 4

Range Correction for ^{16}O in Silicon

MeV	μm	MeV	μm	MeV	μm	MeV	μm	MeV	μm
(0.0	0.0)	(0.2	0.12)	(0.4	0.24)	(0.6	0.37)	(0.8	0.49)
(1.0	0.61)	(1.2	0.73)	(1.4	0.86)	(1.6	0.98)	(1.8	1.10)
(2.0	1.23)	(2.2	1.35)	(2.4	1.47)	(2.6	1.59)	(2.8	1.72)
(3.0	1.84)	(3.2	1.96)	(3.4	2.08)	3.6	2.21	3.8	2.33
3.6	2.21	3.8	2.33	4.0	2.45	4.2	2.57	4.4	2.70
4.6	2.82	4.8	2.89	5.0	2.97	5.2	3.04	5.4	3.11
5.6	3.17	5.8	3.22	6.0	3.28	6.2	3.34	6.4	3.39
6.6	3.45	6.8	3.51	7.0	3.56	7.2	3.62	7.4	3.68
7.6	3.73	7.8	3.78	8.0	3.83	8.2	3.88	8.4	3.93
8.6	3.98	8.8	4.02	9.0	4.07	9.2	4.12	9.4	4.17
9.6	4.22	9.8	4.27	10.0	4.31	11.0	4.54	12.0	4.76
13.0	5.00	14.0	5.22	15.0	5.42	16.0	5.61	17.0	5.79
18.0	5.97	19.0	6.13	20.0	6.30	21.0	6.45	22.0	6.61
23.0	6.76	24.0	6.90	25.0	7.04	26.0	7.17	27.0	7.31
28.0	7.43	29.0	7.55	30.0	7.66	31.0	7.80	32.0	7.93
33.0	8.04	34.0	8.14	35.0	8.23	36.0	8.32	37.0	8.41
38.0	8.50	39.0	8.59	40.0	8.67	41.0	8.76	42.0	8.83
43.0	8.90	44.0	8.97	45.0	9.03	46.0	9.09	47.0	9.15
48.0	9.20	49.0	9.25	50.0	9.31	51.0	9.36	52.0	9.40
53.0	9.45	54.0	9.50	55.0	9.54	56.0	9.58	57.0	9.62
58.0	9.66	59.0	9.69	60.0	9.73	61.0	9.76	62.0	9.79
63.0	9.82	64.0	9.85	65.0	9.87	66.0	9.89	67.0	9.91
68.0	9.93	69.0	9.95	70.0	9.97	71.0	9.99	72.0	10.00
73.0	10.02	74.0	10.04	75.0	10.05	76.0	10.06	77.0	10.07
78.0	10.08	79.0	10.09	80.0	10.10	81.0	10.11	82.0	10.11
83.0	10.12	84.0	10.12	85.0	10.13	86.0	10.13	87.0	10.13
88.0	10.13	89.0	10.13	90.0	10.13	91.0	10.12	92.0	10.12
93.0	10.11	94.0	10.10	95.0	10.10	96.0	10.09	97.0	10.08
98.0	10.07	99.0	10.06	100.0	10.05	101.0	10.04	102.0	10.02
103.0	10.01	104.0	9.99	105.0	9.97	106.0	9.96	107.0	9.94
108.0	9.92	109.0	9.90	110.0	9.88	111.0	9.86	112.0	9.84
113.0	9.81	114.0	9.79	115.0	9.77	116.0	9.74	117.0	9.72
118.0	9.69	119.0	9.66	120.0	9.64	121.0	9.61	122.0	9.58
123.0	9.55	124.0	9.53	125.0	9.50	126.0	9.47	127.0	9.43
128.0	9.40	129.0	9.37	130.0	9.34	131.0	9.31	132.0	9.27
133.0	9.24	134.0	9.21	135.0	9.17	136.0	9.14	137.0	9.10
138.0	9.07	139.0	9.03	140.0	8.99	141.0	8.95	142.0	8.92
143.0	8.88	144.0	8.85	145.0	8.81	146.0	8.77	147.0	8.73
148.0	8.69	149.0	8.65	150.0	8.61	151.0	8.57	152.0	8.53
153.0	8.48	154.0	8.44	155.0	8.40	156.0	8.36	157.0	8.31
158.0	8.27	159.0	8.23	160.0	8.18	161.0	8.14	162.0	8.09
163.0	8.04	164.0	8.00	165.0	7.95	166.0	7.90	167.0	7.85
168.0	7.81	169.0	7.76	170.0	7.71	171.0	7.66	172.0	7.61
173.0	7.56	174.0	7.51	175.0	7.45	176.0	7.40	177.0	7.35
178.0	7.30	179.0	7.25	180.0	7.19	181.0	7.14	182.0	7.08
183.0	7.03	184.0	6.97	185.0	6.92	186.0	6.86	187.0	6.80
188.0	6.75	189.0	6.69	190.0	6.63	191.0	6.57	192.0	6.51
193.0	6.45	194.0	6.39	195.0	6.34	196.0	6.27	197.0	6.21
198.0	6.15	199.0	6.09	200.0	6.03	201.0	5.96	202.0	5.90
203.0	5.83	204.0	5.77	205.0	5.70	206.0	5.64	207.0	5.57
208.0	5.50								

Values in parentheses are based on linear extrapolation from higher energies.

TABLE C - 5

Rms Uncertainties in Mass

	^{4}He (amu)	^{14}N (amu)	^{16}O (amu)
Electronics	0.007	0.011	0.010
Uncertainties in Data Points	0.008	0.030	0.011
Systematic Errors	0.004	0.028	0.023
Sub Total	0.011	0.042	0.027
Error Relative to Helium		0.038	0.044
TOTAL		0.06	0.05

For the mass uncertainties listed in Table C-5, the typical accuracy for the difference between the range corrections for any 50 μm range interval is ~ 0.1 μm. The absolute magnitude of the range correction is more uncertain. To determine the absolute magnitude a linear extrapolation of the range correction to zero energy was performed although the true second derivative $\frac{d^2}{dE^2}(\Delta R)$ probably is not zero. However, as noted previously, a shift in the absolute magnitude of the range does not affect the mass response of the instrument.

When the range corrections of Tables C-2, C-3, and C-4 are substituted into equation C-4, one should obtain the correct mass for ^4He, ^{14}N, and ^{16}O since the range corrections were actually obtained from these isotopes. According to our assumptions, we should also be able to calculate the proper masses for all other isotopes of helium, nitrogen, and oxygen. Using the new range corrections along with Janni's proton range - energy table, mass histograms were obtained for a portion of the hydrogen, helium, nitrogen, and oxygen calibration data. The results are shown in Figure C-12. The isotopes have the proper masses within the predicted accuracy, thus supporting the validity of the new range corrections.

FIGURE C - 12

Mass histograms for hydrogen, helium, nitrogen, and oxygen calibration data using range corrections in Tables C-2, C-3, and C-4. The hydrogen, nitrogen, and oxygen isotopes resulted from inelastic scattering of an ^{16}O beam. The data from a ^{14}N and an ^{16}O beam were combined to obtain the mass histogram for helium.

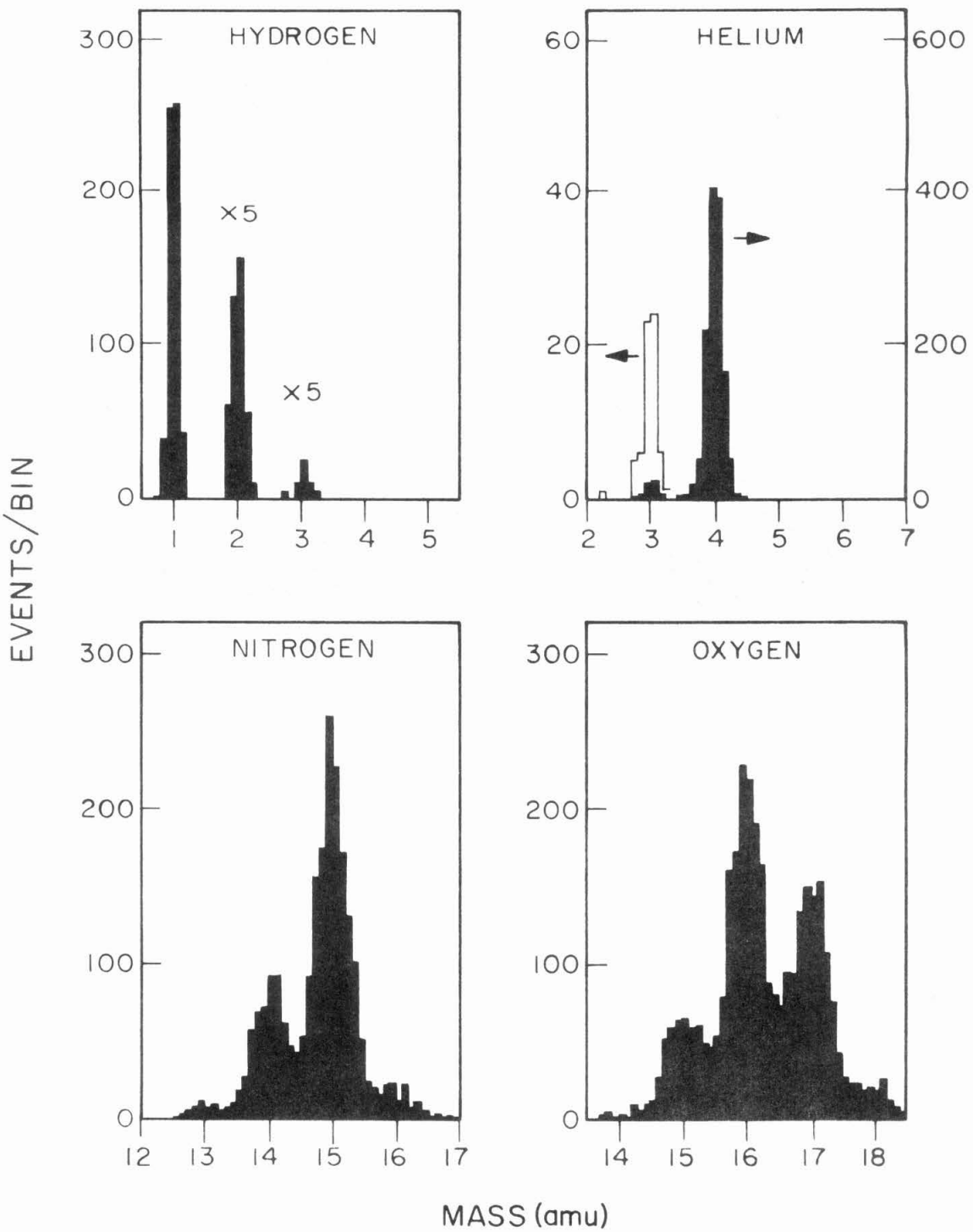
HYDROGEN
HELIUM
NITROGEN
OXYGEN
×5
×5
EVENTS/BIN
MASS (amu)
300
200
100
0
60
40
20
600
400
200
1
2
3
4
5
6
7
12
13
14
15
16
17
18

REFERENCES

Anderson, H. H., Simonsen, H., Sorenson, H., "An Experimental Investigation of Charge-Dependent Deviations from the Bethe Stopping Power Formula", Nucl. Phys., A125, 171 (1969).

Ashley, J. C., Ritchie, R. H., Brandt, W., "Z_1^3 Effect in the Stopping Power of Matter for Charged Particles", Phys. Rev. B, 5, 2393 (1972).

Axford, W. I., "The Interaction of the Solar Wind with the Interstellar Medium", Solar Wind, edited by C. P. Sonett, J. P. Coleman, J. M. Wilcox, NASA SP-308 (Washington, D.C.: National Aeronautics and Space Administration), 609 (1972).

Barkas, W. H., Dyer, J. N., Heckman, H. H., "Resolution of the Σ^- Anomaly", Phys. Rev. Lett., 11, 26 (1963).

Bertsch, D. L., Biswas, S., Fichtel, C. E., Pellerin, C. J., Reames, D. V., "Variations of the Relative Abundances of He, (CNO) and Fe- Group Nucleii in Solar Cosmic Rays and Their Relationship to Solar Particle Acceleration", Solar Physics, 31, 247 (1973).

Bevington, Phillip. R., "Data Reduction and Error Analysis for the Physical Sciences", McGraw-Hill, New York (1969).

Bichsel, H., Tschalaer, C., "A Range - Energy Table for Heavy Particles in Silicon", Nuclear Data, A3, 343 (1967).

Brown, J. W., "A Satellite Measurement of Cosmic-Ray Abundances and Spectra in the Charge Range $2 \leq Z \leq 10$", Ph.D. Thesis, Calif. Inst. of Technology (1973).

Cameron, A. G. W., "A Critical Discussion of the Abundances of Nuclei", Explosive Nucleosynthesis, edited by D. Schramm, and W. Arnett, University of Texas Press, Austin (1973).

Chan, J. H., Price, P. B., "Anomalies in the Composition of Interplanetary Heavy Ions with $0.01 < E < 40$ MeV per amu", Astrophys. J., 190, L39 (1974).

Comstock, G. M., Fan, C. Y., Simpson, J. A., "Energy Spectra and Abundances of the Cosmic-Ray Nuclei Helium to Iron from the OGO-I Satellite Experiment", Astrophys. J., 155, 609 (1969).

Evans, Robley J., "The Atomic Nucleus", McGraw-Hill, New York (1955).

Fisk, L., "Solar Modulation of Cosmic-Ray Oxygen and Nitrogen at Low Energies", Bull. Am. Phys. Soc., 19, 434 (1974).

Fisk, L., Kozlovsky, B., Ramaty, R., "An Interpretation of the Observed Oxygen and Nitrogen Enhancements in Low-Energy Cosmic Rays", Astrophys. J., 190, L35 (1974).

Garcia-Munoz, M., Mason, G. M., Simpson, J. A., "A New Test for Solar Modulation Theory: The 1972 May-July Low-Energy Galactic Cosmic-Ray Proton and Helium Spectra", Astrophys. J., 182, L81 (1973).

Garcia-Munoz, M., Mason, G. M., Simpson, J. A., "The Isotopic Composition of Low Energy Nitrogen Galactic Cosmic Rays", Symposium on Measurements and Interpretation of the Isotopic Composition of Solar and Galactic Cosmic Rays, Durham, New Hampshire (1974).

Garcia-Munoz, M., Mason, G. M., Simpson, J. A., "The Anomalous He^4 Component in the Cosmic Ray Spectrum at $\leqslant$ 50 MeV per Nucleon during 1972-1974", to be published (1975).

Garrard, T., "A Quantitative Investigation of the Solar Modulation of Cosmic Ray Protons and Helium Nuclei", Ph.D. Thesis, Calif. Inst. of Technology (1973).

Garrard, T., "The Caltech Electron and Isotope Spectrometer Experiments on IMP's H and J", Space Radiation Laboratory Internal Report, No. 50 Calif. Inst. of Technology (1974a).

Garrard, T., "Abstraction of IMP Tapes", Space Radiation Laboratory Internal Report No. 52, Calif. Inst. of Technology (1974b).

Garrard, T., "General Overview of IMP Data Processing", Space Radiation Laboratory Internal Report No. 59, Calif. Inst. of Technology (1974c).

Garrard, T., and Hurford, G., "IMP-H Experiment Tape Data Format", Space Radiation Laboratory Internal Report No. 43, Calif. Inst. of Technology (1973).

Garrard, T., Petruncola, A., "STRIP Program User's Guide", Space Radiation Laboratory Internal Report No. 49, Calif. Inst. of Technology (1974).

Goldberg, L., Muller, E. A., Aller, L. H., "The Abundances of Elements in the Solar Atmosphere", Astrophys. J., 5, 1 (1960).

Hartman, S., "Geometrical Factors for IMP-H", Space Radiation Laboratory Internal Report No. 45, Calif. Inst. of Technology (1973).

Heckman, H. H., and Lindstrom, P. J., "Stopping-Power Differences between Positive and Negative Pions at Low Velocities", Phys. Rev. Lett., 22, 871 (1969).

Hovestadt, D., Vollmer, O., Gloeckler, G., Fan, C. Y. "Differential Energy Spectra of Low-Energy (< 8.5 MeV per Nucleon) Heavy Cosmic Rays during Solar Quiet Times", Phys. Rev. Lett., 31, 650 (1973).

Hoyle, F., Clayton, D. D., "Nucleosynthesis in White-Dwarf Atmospheres", Astrophys. J., 191, 705 (1974).

Hughes, M. P., Thompson, A. R., Colvin, R. S., "An Absorption Study of the Galactic Neutral Hydrogen at 21 Centimeters Wavelength", Astrophys. J. Suppl., 23, 323 (1971).

Hurford, G. J., "Observations of Hydrogen and Helium Isotopes in Solar Cosmic Rays", Ph.D. Thesis, Calif. Inst. of Technology (1974).

Hurford, G. J., "D25 → D6 Crosstalk on IMP-7 EIS", Addendum to Space Radiation Laboratory Internal Report No. 50 by T. Garrard, Calif. Inst. of Technology (1974b).

Hurford, G. J., Mewaldt, R. A., Stone, E. C., Vidor, S. B., Vogt, R. E., "The Isotopic Composition of 5 to 12 MeV/Nucleon Cosmic Ray Nitrogen and Oxygen Nuclei", Bull. Am. Phys. Soc., 19, 433 (1974).

Janni, J. F., "Calculations of Energy Loss, Range, Pathlength, Straggling, Multiple Scattering, and the Probability of Inelastic Nuclear Collisions for 0.1- to 1000- MeV Protons", Technical Report No. AFWL-2R-65-150 (1966).

Jokipii, J. R., "Propagation of Cosmic Rays in the Solar Wind", Reviews of Geophysics and Space Physics, 9, 27 (1971).

Kelley, J. G., Sellers, B., Hanser, F. A., "Energy-Loss and Stopping-Power Measurements between 2 and 10 MeV/amu for ^{12}C, ^{14}N, and ^{16}O in Silicon", Phys. Rev. B, 8, 103 (1973).

Lederer, C. M., Hollander, J. M., Perlman, J., Table of Isotopes , John Wiley and Sons, New York (1967).

Livingston, M. S. and Bethe, H. A., "Nuclear Dynamics, Experimental", Rev. Mod. Phys., 9, 245 (1937).

Lund, N., Peters, B., Cowsik, R., Pal, Y., "On the Isotopic Composition of Primary Cosmic Ray Nucleii", Phys. Lett., 31B, 553 (1970).

Marshall, F., "Varian Software for PACE System" Space Radiation Laboratory Internal Report No. 57, Calif. Inst. of Technology (1974).

Mathews, Jon and Walker, Robert L., Mathematical Methods of Physics , Benjamin, New York (1965).

McDonald, F. B., Teegarden, B. J., Trainor, J. H., Webber, W. R., "The Anomalous Abundance of Cosmic Ray Nitrogen and Oxygen Nucleii at Low Energies", Astrophys. J., 187, L105 (1974).

McKibben, R. B., "Azimuthal Propagation of Low-Energy Solar-Flare Protons as Observed from Spacecraft Very Widely Separated in Solar Azimuth", J. Geophys. Res., 22, 3957 (1972).

Mewaldt, R. A., Stone, E. C., Vogt, R. E., "The Time Variation of 5-11 MeV/Nucleon Cosmic Ray Nitrogen and Oxygen Nuclei ", Bull. Am. Phys. Soc., L9, 433 (1974a).

Mewaldt, R. A., Stone, E. C., Vidor, S. B., Vogt, R. E., "Isotopic Composition of 6 to 12 MeV/nuc Cosmic Ray Nitrogen and Oxygen", Symposium on Measurements and Interpretation of the Isotopic Composition of Solar and Galactic Cosmic Rays, Durham, New Hampshire (1974b).

Mewaldt, R. A., Stone, E. C. Vidor, S. B., Vogt, R. E., "Isotope Calibration of a dE/dX-E Telescope", Symposium on Measurements and Interpretation of the Isotopic Composition of Solar and Galactic Cosmic Rays, Durham, New Hampshire (1974c).

Mewaldt, R. A., Vidor, S. B., "IMP's-H and -J Electronic Calibration", Space Radiation Laboratory Internal Report No. 60, Calif. Inst. of Technology (1975).

Meyer, P., "Cosmic Rays in the Galaxy", Annual Review of Astronomy and Astrophysics, 7, 1 (1969).

Mogro-Campero, A., Schofield, N., Simpson, J. A., "On the Origin of Low Energy Heavy Nucleii below ~ 30 MeV per Nucleon Observed in Interplanetary Space During Solar Quiet Times 1968-72", Thirteenth International Cosmic Ray Conference, Conference Papers, Denver, 140 (1973).

Northcliffe, L. C., "Passage of Heavy Ions through Matter", Ann. Rev. Nucl. Sci., 13, 67 (1963).

Northcliffe, L. C. and Schilling, R. F., "Range and Stopping Power Tables for Heavy Ions", Nuclear Data Tables, A7, 233 (1970).

Pottasch, S., "On the Interpretation of the Solar Ultraviolet Emission Spectrum", Space Sci. Rev., 3, 816 (1964).

Rogerson, J. B., York, D. G., Drake, J. F., Jenkins, E. B., Morton, D. C., Spitzer, L., "Spectrophotometric Results from the Copernicus Satellite. III. Ionization and Composition of the Intercloud Medium", Astrophys. J., 181, L110 (1973).

Rossi, Bruno, High Energy Particles , Prentice-Hall, Englewood Cliffs (1952).

Rygg, I., Earl, J. A., "Balloon Measurements of Cosmic Ray Protons and Helium over Half a Solar Cycle 1965-1969", J. Geophys. Res., 76, 7445 (1971).

Sellers, L., Hanser, F. A., Kelley, J. G., "Energy Loss and Stopping-Power Power Measurements Between 2 and 10 MeV/amu for ^{3}He and ^{4}He in Silicon", Phys. Rev. B, 8, 98 (1973).

Seltzer, S. M., and Berger, M. J., "Energy Loss Straggling of Protons and Mesons:Tabulation of the Vavilov Distribution", Studies in Penetration of Charged Particles in Matter, NAS-NRC-Publication 1133, 187 (1964).

Shapiro, M. M. and Silberberg, R., "Heavy Cosmic-Ray Nucleii", Ann. Rev. Nucl. Sci., 20, 323 (1970).

Starrfield, S. D., Sparks, W. M., Truran, J. W., "An Extremely Carbon Enhanced Nova Model", to be published (1975).

Teegarden, B. J., McDonald, F. B., Balasubrahmanyan, V. K., "Spectra and Charge Composition of the Low Energy Galactic Cosmic Radiation from Z = 2 to 14", Proceedings of the 11th International Cosmic Ray Conference, 1, Budapest, 345 (1969).

Teegarden, B. J., von Rosenvinge, T. T., McDonald, F. B., "Satellite Measurements of the Charge Composition of Solar Cosmic Rays in the $6 \leq Z \leq 26$ Interval", Astrophys. J., 180, 571 (1973).

Tsao, C. H., Shapiro, M. M., Silberberg, R., "Cosmic Ray Isotopes at Energies > 2 GeV/amu", 13th International Cosmic Ray Conference, Conference Papers, Denver, 107, (1973).

Van Hollebeke, M. A. I., Ma Sung, L. S., McDonald, F. B., "The Variation Of Solar Proton Energy Spectra and Size Distribution with Heliolongitude", Goddard Space Flight Center preprint X-660-74-298(1974).

Vidor, S. B., "Calibration of Pulser with α-Particles", Space Radiation Laboratory Internal Report No. 31, Calif. Inst. of Technology (1972).

Vidor, S. B., "Geometrical Factor for IMP-J", Addendum to Space Radiation Laboratory Internal Report No. 45 by S. Hartman, Calif. Inst. of Technology (1974).

Vidor, S. B., "IMP-J Tandem Calibrations", Space Radiation Laboratory Internal Report No. 64, Calif. Inst. of Technology (1975).

Vidor, S. B., "Cyclotron Calibration of the Spare IMP Telescope", Space Radiation Laboratory Internal Report No. 63, Calif. Inst. of Technology (1975b).

Vidor, S. B., "D5 → D4 Cross-Talk on IMP-7 EIS", Addendum to Space Radiation Laboratory Internal Report No. 50 by T. Garrard, Calif. Inst. of Technology (1975c).

Webber, W. R., "Cosmic Ray Charge Measurements - a 1972 Summary", Inter-American Seminar on Cosmic Rays, Sao Paulo, Brazil, October(1972).

Webber, W. R., and Lezniak, J. A., "The Comparative Spectra of Cosmic Ray Protons and Helium Nuclei", Astrophysics and Space Science, 30, 361 (1974).

Webber, W. R., Damle, S. V., Kish, J., "Studies of the Chemical Composition of Cosmic Rays with Z = 3-30 at High and Low Energies", Astrophysics and Space Science, 15, 245 (1972).

Webber, W. R., Lezniak, J. A., Kish, J., Damle, S. V., "The Relative Abundance of the Isotopes of Li, Be and B and the Age of Cosmic Rays", Astrophysics and Space Science, 24, 17 (1973).

Weisheit, J. C., "Ionization Equilibrium in HI Regions", Astrophys. J., 185, 877 (1973).